

Report of the Working Group on Photon and Weak Boson Production

Conveners: U. Baur (Buffalo), E.L. Berger (ANL), H.T. Diehl (FNAL), and D. Errede (UIUC)

Subgroup Conveners: *Photon Production:* J. Huston (MSU), J. Owens (FSU), and J. Womersley (FNAL)

Weak Boson Production: D. Casey (MSU) and T. Dorigo (Harvard), *Diboson Production:* U. Baur (Buffalo) and H.T. Diehl (FNAL)

Contributing authors: L. Apanasevich (Rochester), M. Begel (Rochester), Y. Gershtein (Brown), M. Kelly (Michigan), S. E. Kuhlmann (ANL), S. Leone (Pisa), D. Partos (Brandeis), D. Rainwater (FNAL), W.K. Sakumoto (Rochester), G. Steinbrück (Columbia), M. Zieliński (Rochester), and V. Zutshi (Rochester)

This report discusses physics issues which can be addressed in photon and weak boson production in Run II at the Tevatron. The current understanding and the potential of Run II to expand our knowledge of direct photon production in hadronic collisions is discussed. We explore the prospects for using the W -boson cross section to measure the integrated luminosity, improving the measurement of the W and Z boson transverse momentum distributions, the $Z \rightarrow b\bar{b}$ signal, and the lepton angular distribution in W decays. Finally, we consider the prospects for measuring the trilinear gauge boson couplings in Run II.

1. Introduction

For the next few years, the Fermilab Tevatron Collider will be the high energy frontier of particle physics. The luminosity enhancement provided by the Main Injector will significantly increase the discovery reach of the Tevatron experiments over what has been achieved with Run I data. It will also move the experimental program into a regime of precision hadron collider physics. This will make it possible to address open questions of high energy physics from several complementary directions.

Understanding the mechanism of production for photons, W , and Z -bosons is important for several reasons. First of all, it provides an opportunity to directly test the Standard Model (SM). Second, photon and weak boson production often constitute an irreducible background in searches for new physics. Finally, a detailed understanding of the production mechanism for these particles is necessary to control the systematic errors in precision measurements, such as the determination of the W mass (see Ref. [1]).

In this report, we consider several aspects of the production of photons, W , and Z bosons which are of interest for Run II of the Tevatron Collider. In Sec. 2, direct photon production is discussed. A detailed overview of our current experimental and theoretical understanding of direct photon production in hadronic collisions is presented. Direct photon production has long been considered a probe of QCD and a source for extracting the gluon distribution of the proton. Unfortunately, not all existing (fixed target and Tevatron collider) datasets are consistent, and our current theoretical understanding of direct photon production, especially at small photon transverse

momenta, is incomplete. Recent theoretical developments, however, offer optimism that the long-standing difficulties in direct photon production can finally be resolved. The enormous number of photon-jet events expected in Run II may help to shed light on these issues. In particular, photon – jet correlations should be helpful in sorting out the source of disagreement between theory and experiment. In addition, the kinematic reach in transverse momentum will be greatly extended in Run II.

In Sec. 3 several important topics associated with W and Z -boson production are discussed. For many measurements in Run II, knowledge of the integrated luminosity is essential. The integrated luminosity can be extracted either from the total inelastic cross section or from the cross section of a theoretically well understood process with high statistics, such as inclusive W production. Using the total inelastic cross section to determine the integrated luminosity for Run I has led to inconsistencies which may well persist in Run II. It may thus be advantageous to use the W production cross section as an alternative. In Sec. 3.1 we present a brief overview of the magnitude of the experimental uncertainties in such a measurement. The total uncertainty in the W cross section is found to be dominated by the uncertainty from the parton distribution functions, which is considered in more detail in the Report of the Working Group on Parton Distribution Functions [2].

In Sec. 3, we also consider the transverse momentum distribution of the Z boson, $Z \rightarrow b\bar{b}$ decays, and the prospects to measure the lepton angular distribution in W decays. The $Z p_T$ distribution is of interest as a test of QCD, and as a tool for reducing uncertainties in the transverse momentum distribution of the W . This

is important for a precise determination of the mass of the W boson (see Ref. [1]). Searching for a light Higgs boson in the range between 110 GeV and 180 GeV is one of the prime objectives for Run II. $H \rightarrow b\bar{b}$ decays dominate for Higgs boson masses $M_H < 135$ GeV. The ability to separate the Higgs boson signal in the $Wb\bar{b}$ and $t\bar{t}b\bar{b}$ channels from the large QCD background depends critically on the $b\bar{b}$ invariant mass resolution, and thus on the measured b -quark jet energies. $Z \rightarrow b\bar{b}$ decays offer a testing ground for algorithms designed to improve the jet energy measurement for b jets and are also useful as a calibration tool. The measurement of the lepton angular distributions in W decays serves as a probe of NLO QCD. The measurement carried out by DØ in Run I is statistics limited. While a QCD calculation is preferred, large deviations from QCD are not excluded. In Run II, this measurement will allow for a much improved test of the QCD prediction.

In Sec. 4 of this report, we discuss di-boson production. Vector boson pair production provides a sensitive ground for direct tests of the trilinear gauge boson couplings. A brief overview of the WWV ($V = \gamma, Z$), $Z\gamma V$ and ZZV couplings is presented and recent advances in our theoretical understanding of the NLO QCD corrections to di-boson production are described. After a brief review of the limits on trilinear couplings obtained in Run I, the prospects for strengthening existing bounds in Run II are discussed. In addition to improving the measurements of WWV and $Z\gamma V$ couplings, it will be possible to determine the ZZV couplings via ZZ production with an accuracy of about 15% in Run II, and to observe the so-called “radiation zero” in $W\gamma$ production.

2. Direct Photon Production

The use of direct photon production as an electromagnetic probe of hard scattering dynamics has a history which covers more than twenty years. As in other electromagnetic processes such as lepton pair production or deep inelastic scattering, the point-like coupling of the photon to charged particles offers some simplifications over purely hadronic probes. Compared to hadronic jet production, direct photon production offers the apparent advantages of having fewer subprocesses at lowest order and of avoiding the complications of jet definitions when measuring or calculating a cross section. This latter point means that one can extend the range of transverse momenta to smaller values for direct photons than for jets. However, in actual practice, these apparent simplifications must be tempered by having to deal with backgrounds from neutral meson decays, a lower event rate compared to jet production, and complications from photons produced

during jet fragmentation, to name just a few. Nevertheless, direct photon data provide information which complements that obtained from other hard scattering processes. Furthermore, photons may be important signatures of physics beyond the SM. Therefore, it is necessary to understand the “conventional” sources of photons before one can fully exploit them in signatures designed to look for new physics.

In this Section, recent work concerning the phenomenology of initial-state gluon emission in direct-photon production in hadron collisions is reported. In Sec. 2.1, high-mass direct-photon pairs are used to explore the impact of such radiation in terms of effective parton transverse momenta, k_T . At fixed-target energies, data on high- p_T inclusive π^0 and $\pi^0\pi^0$ production are used to further clarify the arguments presented. We then review progress towards fully resummed QCD descriptions and present comparisons of a phenomenological k_T model to recent fixed-target and collider data. Possibilities for more extensive studies with data from Run II, and the additional information they can provide for these considerations, are explored in Sec. 2.1.5. A consistent picture of the observed deviations of NLO perturbative QCD (pQCD) calculations from inclusive direct-photon and π^0 data is now emerging, and we comment on the implications of these results for the extraction of the gluon distribution, $G(x)$, in Sec. 2.1.6.

Run II has the potential to significantly expand our knowledge of direct photon production. Issues related to our understanding of the relevant production mechanisms in the kinematic range accessible during Run II are reviewed in Sec. 2.2. In this Section, we also discuss observables which may help improve our understanding of direct photon production as well as experimental issues which can affect the quality of the data. In Sec. 2.2.4 some predictions for photon-jet correlations are presented. The potential of observables other than the usual single photon p_T distribution to help elucidate the underlying dynamics is discussed.

Run I data are available on the associated production of a γ carrying large transverse momentum along with a charm quark c whose transverse momentum balances a substantial portion of that of the photon [3]. An intriguing possibility is that the data may be used to measure the charm quark density in the nucleon as well as to probe dynamical correlations predicted by QCD. These possibilities are discussed in Ref. [4] where predictions are obtained from a full next-to-leading order perturbative QCD calculation of $p + \bar{p} \rightarrow \gamma + c + X$ at high energy. The associated production of a photon and a heavy quark is not discussed further in this report.

2.1. Present Status of Direct Photon Production in Hadronic Collisions¹

2.1.1. Introduction

Single and double direct-photon production at high p_T have long been viewed as ideal processes for testing the formalisms of pQCD. NLO calculations are available for both processes [5, 6, 7, 8, 9]. While the importance of including gluon emission through the resummation formalism was recognized and available for some time for the di-photon process [10, 11], it is only recently that this approach has been developed for inclusive direct-photon production [12, 13, 14, 15, 16, 17]. A complete theoretical description of the direct-photon process is of special importance as it has long been expected to provide one of the best measurements of the gluon distribution in the proton. The quark-gluon Compton scattering subprocess ($gq \rightarrow \gamma q$) shown in Fig. 1 provides a major contribution to inclusive direct-photon production. The gluon distribution ($G(x)$) is relatively well constrained for $x < 0.1$ by deep-inelastic scattering (DIS) and Drell-Yan (DY) data, but less so at larger x [18]. Fixed-target direct-photon data can constrain $G(x)$ at large x , and consequently has been incorporated in several modern global parton distribution analyses [19, 20, 21]. More recently, however, both the completeness of the theoretical NLO description of the direct-photon process, and the consistency of the available data sets have been the subject of intense debate [21, 22, 23, 24, 25, 26, 27]. Direct-photon measurements

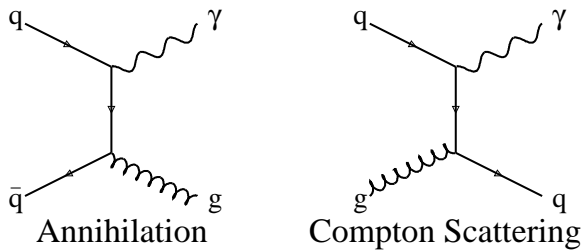


Figure 1. Leading order diagrams for direct-photon production.

in collider data, and especially the data expected from the forthcoming Run II at the Tevatron, provide an important testing ground for novel approaches and improvements in the understanding of the direct-photon process, and therefore can help resolve the present arguments.

¹ Contributed by: L. Apanasevich, M. Begel, Y. Gershtein, J. Huston, S. E. Kuhlmann, D. Partos, J. Womersley, M. Zieliński, and V. Zutshi.

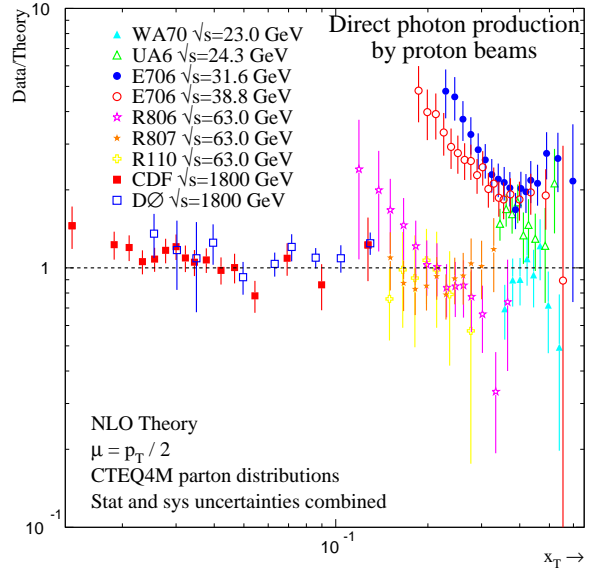


Figure 2. Comparison between proton-induced direct-photon data and NLO pQCD calculations for several experiments as a function of photon x_T ($= 2p_T/\sqrt{s}$). (The CDF and D0 data are from Run Ia, see Figs. 23 and 24 for the Run Ib update.)

The understanding of single and double direct photon yields, and of the more copious high- p_T π^0 production, is of importance for searches for the Higgs in the $\gamma\gamma$ decay mode at the LHC. In addition, Higgs production, both at the Tevatron and the LHC, can be affected by soft-gluon emission from the initial-state partons, and separation of signal and background can benefit from a reliable resummation formalism or equivalent parton-shower Monte Carlo descriptions [28, 29, 30].

2.1.2. Parton Transverse Momentum

A pattern of deviation has been observed between measured direct-photon cross sections and NLO calculations (Fig. 2). The origin of the disagreement has been ascribed to the effect of initial-state soft-gluon radiation [23, 24]. Correlations between any produced high- p_T particles probe aspects of the hard scatter not easily accessible via studies of single inclusive particle production. In particular, studies of high-mass pairs of particles such as direct photons and π^0 's can be used to extract information about the transverse momentum of partons, k_T , prior to the hard scatter. Whatever the source, any transverse momentum between the partons will appear as a net p_T imbalance among the outgoing particles produced in the hard scatter, and is therefore reflected in the vector sum of the individual p_T

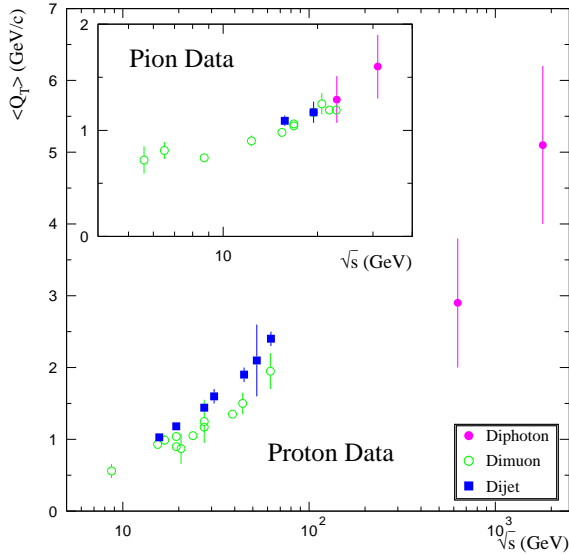


Figure 3. $\langle Q_T \rangle$ of pairs of muons, photons, and jets produced in hadronic collisions versus \sqrt{s} .

values of the outgoing particles (Q_T). If the outgoing particles are pairs of photons or leptons, then this variable should provide a good measure of $\langle k_T \rangle$, with $\langle k_T \rangle / \text{parton} \approx \langle Q_T \rangle / \sqrt{2}$. When the outgoing particles are partons, they will hadronize, but the reconstructed jets can also yield a measure of $\langle k_T \rangle$.

Evidence of significant k_T has been found in several measurements of dimuon, diphoton, and dijet production; a collection of $\langle Q_T \rangle$ measurements is displayed in Fig. 3 for a wide range of \sqrt{s} [31, 32, 33, 34, 35]. The values of $\langle Q_T \rangle$ are large, and increase with increasing \sqrt{s} . The dijet k_T measurements (Fig. 3) agree qualitatively with the dimuon and diphoton results, though they have somewhat higher mean values. Such a shift is expected since there is also potential for final-state soft-gluon emission in dijet events. The values of $\langle k_T \rangle$ per parton indicated by these data are too large to be interpreted as due only to the size of the proton. From these observations, one can infer that the $\langle k_T \rangle$ per parton is of order 1 GeV/c at fixed-target energies, increasing to 3 GeV/c to 4 GeV/c at the Tevatron collider, whereas $\langle k_T \rangle$ would be expected to be of the order of 0.3 GeV/c to 0.5 GeV/c based solely on proton size.

The p_T imbalance between the outgoing particles can also be examined using kinematic variables other than Q_T . Given some finite k_T , the two outgoing particles no longer emerge back-to-back; the azimuthal angle between the particles, $\Delta\phi$, will differ from 180° . The transverse momentum normal to the scattering plane,

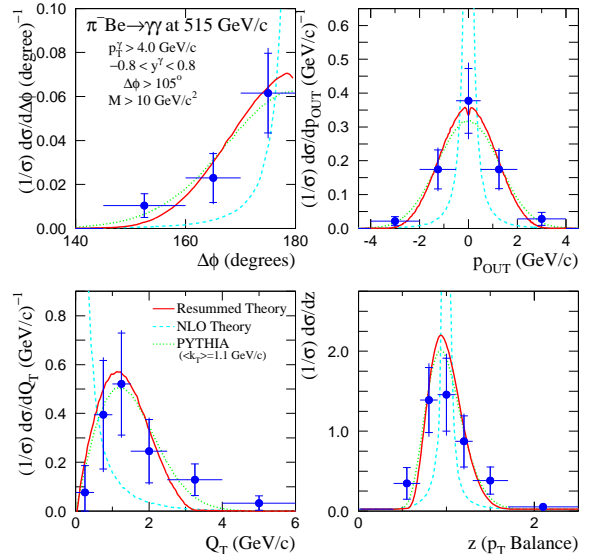


Figure 4. Diphoton $\Delta\phi$, p_{OUT} , Q_T , and z distributions for E706 π^- Be data at $\sqrt{s} = 31.1$ GeV [31]. Overlaid on the data are the results from NLO [8] (dashed) and resummed [10] (solid) calculations. PYTHIA [37] results (dotted) with $\langle k_T \rangle = 1.1$ GeV/c are also shown.

p_{OUT} , and the p_T -balance quantity,

$$z = -(\vec{p}_{T1} \cdot \vec{p}_{T2} / p_{T2}^2) = (p_{T2} / p_{T1}) \cos \Delta\phi, \quad (1)$$

are two useful variables, each with two possible values per pair of objects.

High-mass direct-photon pairs have been measured at the Tevatron [33, 31, 36]. Distributions as a function of $\Delta\phi$, p_{OUT} , Q_T , and z for such events from E706 [31] are shown in Fig. 4. Overlaid on the data are the results from both NLO [8] and resummed [10] pQCD calculations. There are large differences in the predicted shapes. At leading order, each of these distributions would consist of a δ function. While the NLO prediction has finite width due to the radiation of a single hard gluon, the resummed theory, which also includes the effects of multiple soft-gluon emission, is in better agreement with the data. This is particularly true for Q_T , where the NLO calculation tends towards infinity as $Q_T \rightarrow 0$, while the resummed (RESBOS [10]) calculation follows the shape of the data and goes to zero. Also shown in Fig. 4 are the distributions from PYTHIA [37], where k_T effects are approximated by a Gaussian smearing technique. PYTHIA provides a reasonable description of the di-photon data using a value for $\langle k_T \rangle$ consistent with the measurements displayed in Fig. 4. Comparisons between CDF and DØ data lead to similar conclusions [29]. There is also good agreement between the WA70 di-photon data [

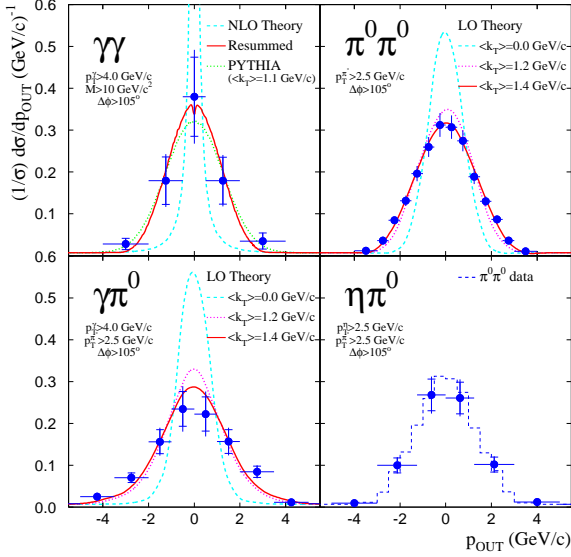


Figure 5. p_{OUT} distributions for $\gamma\gamma$, $\pi^0\pi^0$, $\gamma\pi^0$, and $\eta\pi^0$ for E706 π^- Be data at $\sqrt{s} = 31.1$ GeV [31]. Overlaid on the diphoton data are the results from NLO [8] and resummed [10] pQCD calculations. PYTHIA [37] results with $\langle k_T \rangle = 1.1$ GeV/c are also shown. Overlaid on the $\pi^0\pi^0$ and $\gamma\pi^0$ are the results from LO pQCD calculations [38] for various values of $\langle k_T \rangle$ and fixed $\langle q_T \rangle = 0.6$ GeV/c. The $\pi^0\pi^0$ data have been overlaid on the $\eta\pi^0$ data for comparison.

32] and resummed pQCD [11]. The increased statistics expected for Run II should allow for more detailed comparisons between di-photon data and theory.

Similar evidence for k_T effects is seen in analyses of high-mass $\pi^0\pi^0$, $\eta\pi^0$, and $\gamma\pi^0$ pairs by E706 [31]. This is illustrated by Fig. 5 which shows a comparison of the p_{OUT} distribution from each of these samples. The LO pQCD calculation [38], which incorporates k_T effects using a Gaussian smearing technique similar to that used in PYTHIA [37], provides a reasonable characterization of k_T -sensitive variables such as $\Delta\phi$ and p_{OUT} for $\langle k_T \rangle$ similar to that measured for di-photons. The $\langle k_T \rangle$ values needed to provide good matches to the data for $\pi^0\pi^0$ and $\gamma\pi^0$ are slightly larger than for $\gamma\gamma$, but that is expected since π^0 's emanate from final-state quarks and gluons that can produce additional gluon radiation. (We use $\langle q_T \rangle = 0.6$ GeV/c [35] for the p_T due to fragmentation.)

2.1.3. k_T Phenomenology

Similar soft-gluon contributions are expected to be present in other hard-scattering processes, such as inclusive production of jets or direct photons [39, 40, 41, 42]. Resummed pQCD calculations for single direct-photon production are currently under

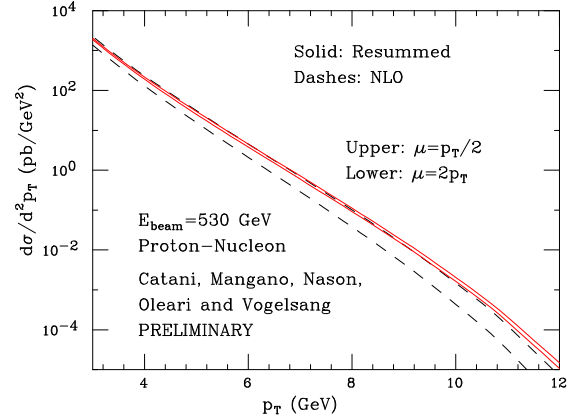


Figure 6. Comparison between a threshold resummed and a NLO theory calculation for direct-photon production for two scale choices: $p_T/2$ and $2p_T$ [12].

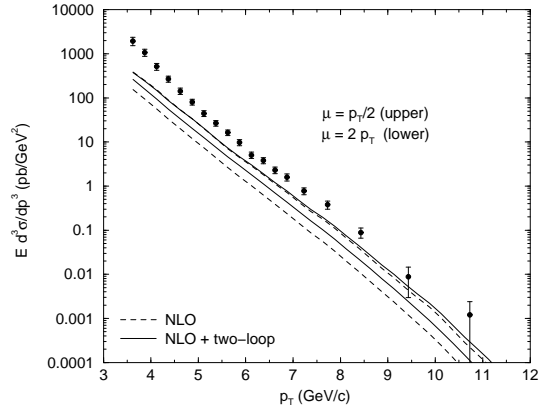


Figure 7. NLO and NNLO results for direct-photon production in hadronic collisions compared to E706 [45] p Be data at $\sqrt{s} = 31.6$ GeV [13].

development [12, 13, 14, 15, 16, 17]. Two recent independent threshold-resummed pQCD calculations for direct photons [12, 13] do not include k_T effects, but exhibit less dependence on QCD scales than the NLO theory (see Figs. 6 and 7). These threshold-resummed calculations agree with the NLO prediction for the scale $\mu \approx p_T/2$ at low p_T , and show an enhancement in cross section at high p_T .

A method for simultaneous treatment of recoil and threshold corrections in inclusive single-photon cross sections has been developed [17] within the formalism of collinear factorization. This approach accounts explicitly for the recoil from soft radiation in the hard-scattering subprocess, and conserves both energy

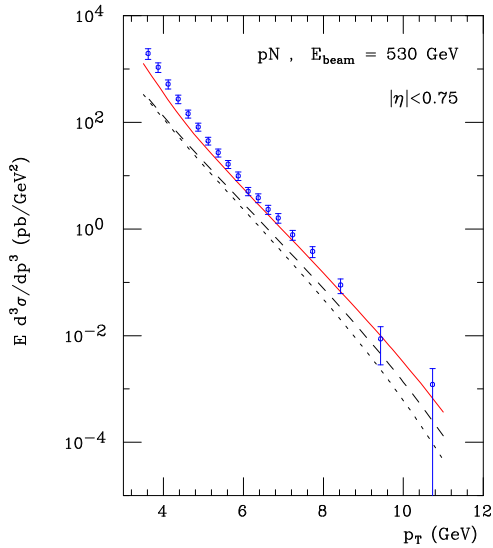


Figure 8. Direct-photon cross section for the E706 data [45]. The dotted line represents the full NLO calculation, while the dashed and solid lines respectively incorporate pure threshold resummation [12] and joint threshold and recoil resummation [17].

and transverse momentum for the resummed radiation. At moderate p_T , substantial enhancements from higher-order perturbative and power-law non-perturbative corrections have been found at fixed-target energies, as illustrated in Fig. 8 in a comparison with the E706 direct-photon measurement at $\sqrt{s} = 31.6$ GeV. Although the present numerical results are only exploratory estimates of the size of expected effects, it is already clear that the phenomenological consequences are significant.

Approximate phenomenological approaches to k_T -smearing have been used in the past to investigate deviations between data and NLO pQCD. The underlying hypothesis is that the leading gluon in NLO pQCD calculations is inadequate for describing the full initial-state parton shower. Full parton shower Monte Carlos such as PYTHIA or HERWIG have been used to test this idea at collider energies [28]. We used PYTHIA v5.71 [37] and the direct photon process to extract the number of initial-state gluons as well as amount of net k_T present in initial-state gluons, after subtracting the gluon with the highest initial state p_T . The number of initial-state gluons is shown in Fig. 9, illustrating that the number is significantly larger than the NLO pQCD approximation of either 0 or 1. The net k_T present, after subtracting the highest p_T gluon, is shown in Fig. 10 for 10 GeV/c and 50 GeV/c direct

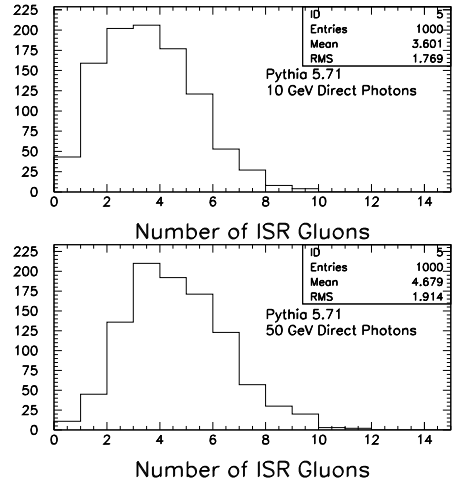


Figure 9. Number of initial-state gluons in PYTHIA from the direct-photon process at $\sqrt{s} = 1.8$ TeV.

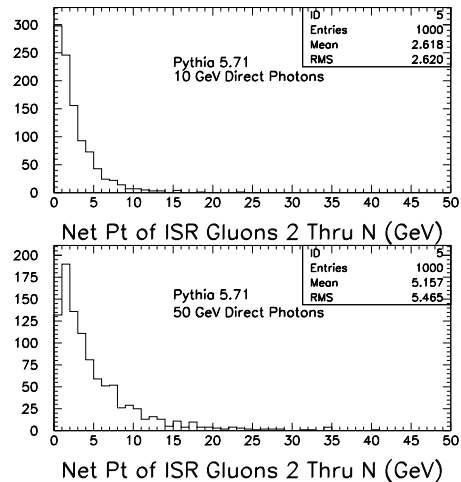


Figure 10. Net p_T due to all but the leading gluon in PYTHIA for direct-photon events.

photons in $p\bar{p}$ collisions at $\sqrt{s} = 1.8$ TeV. The net p_T of such remnant gluons is 2.6 GeV/c for direct photons with $p_T = 10$ GeV/c, and 5.2 GeV/c for $p_T = 50$ GeV/c.

At fixed-target energies, parton-showering models do not provide sufficient smearing because shower development is constrained by cut-off parameters that ensure the perturbative nature of the process. Since traditional NLO calculations do not account for the effects of multiple soft-gluon emission, a kinematical model was employed to incorporate k_T effects in available pQCD calculations of direct-photon (and π^0) production [24]. The relationship between this phenomenological k_T -smearing and the Collins–Soper–Sterman (CSS) resummation formalism [43, 44] was considered in some detail in Ref. [29].

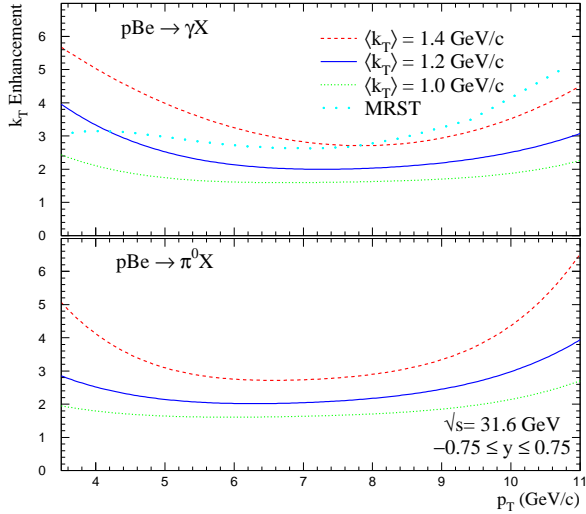


Figure 11. The variation of k_T enhancements, $K(p_T)$, for the E706 pBe data at $\sqrt{s} = 31.6$ GeV.

The same LO pQCD [38] program that successfully characterized high-mass pair production was used to generate K-factors (ratios of LO calculations for any given $\langle k_T \rangle$ to the result for $k_T=0$) for inclusive cross sections (Fig. 11). These K-factors were then applied to the NLO calculations. This procedure involves a risk of double-counting since some of the k_T -enhancements may already be contained in the NLO calculation. However, the effects of such double-counting are expected to be small [24].

As illustrated in the upper part of Fig. 11, the K-factors for direct-photon production at E706 are large over the full range of p_T , and have p_T -dependent shapes—a behavior reminiscent of that obtained from the full resummation formalism [17]. The lower part of Fig. 11 displays K-factors for π^0 production, based on the same model. The data appear to require somewhat larger values of $\langle k_T \rangle$ in the case of π^0 s. At the same values of $\langle k_T \rangle$ the K-factors in π^0 production are somewhat smaller than for γ production. This is expected because π^0 's originate from the fragmentation of the partons.

Figure 11 also displays the K-factor for photons used by the MRST group [21] in recent fits to parton distributions. Their result was obtained through a different technique involving analytical smearing of the parameterized photon cross section, rather than an explicit parton-level calculation. Although the correction is of similar size, it has a different p_T -dependence. It should be noted, however, that despite the similarity in the values of the K-factors used by the MRST group and the ones presented here, the $\langle k_T \rangle$ values cited by MRST

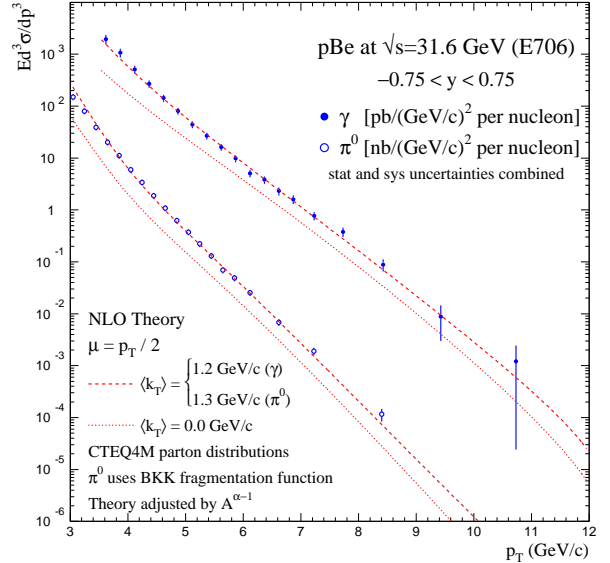


Figure 12. The photon and π^0 cross sections for E706 pBe data at $\sqrt{s} = 31.6$ GeV [45] compared to the k_T -enhanced NLO calculations.

are lower by a factor of 2. This difference can be traced to an erroneous relation between parameters of their analytical smearing function and the transverse momenta of partons in the hard scatter [21]. This has already been pointed out in Refs. [24, 27]. The approach used here [24] is based on explicit parton kinematics and therefore does not suffer from this problem.

The treatment of k_T -enhancements proposed in Ref. [27], based on parton distributions unintegrated over the parton transverse momenta, suggests possible modifications of the above simple picture. Reference [27] imposes strong ordering of momentum transfers of emitted gluons, which prevents transverse momenta of the incoming partonic system from approaching p_T ; k_T values are correlated with the scale at which the parton distributions are sampled. In their approach, the K-factors are expected to be smaller than those shown in Fig. 11, and have less p_T -dependence. Additional scrutiny of the theoretical ideas should help resolve these differences.

2.1.4. High- p_T Production Fixed Target

Invariant cross sections for inclusive direct-photon and π^0 production are displayed for the E706 pBe data at $\sqrt{s} = 31.6$ GeV in Fig. 12, with overlays from theory [45]. Discrepancies between NLO pQCD theory (dotted curves) and the data are striking. The enhancements, generated using $\langle k_T \rangle$ values consistent

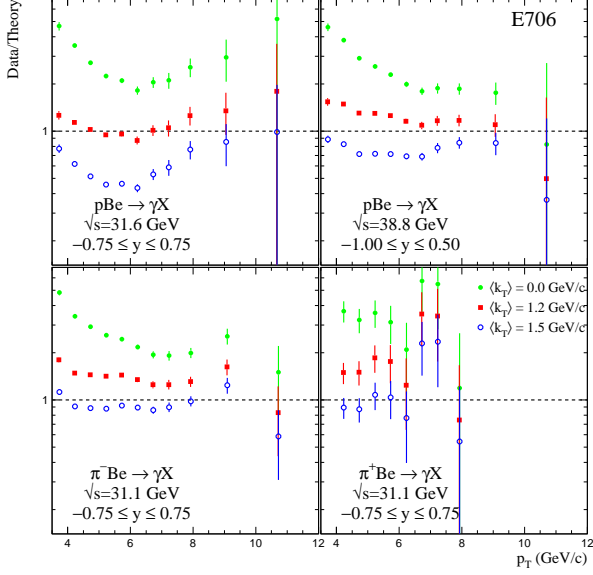


Figure 13. Comparison between the E706 direct-photon data and NLO pQCD calculations with and without k_T enhancements, for several values of $\langle k_T \rangle$.

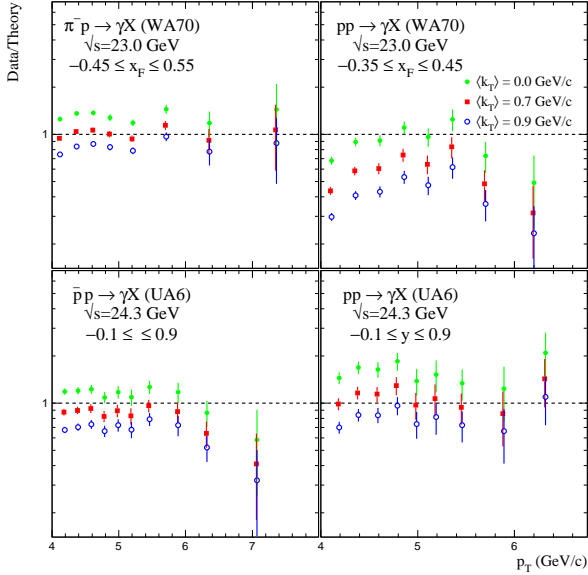


Figure 14. Comparison between the WA70 and UA6 direct-photon data and NLO pQCD calculations with and without k_T enhancements, for several values of $\langle k_T \rangle$.

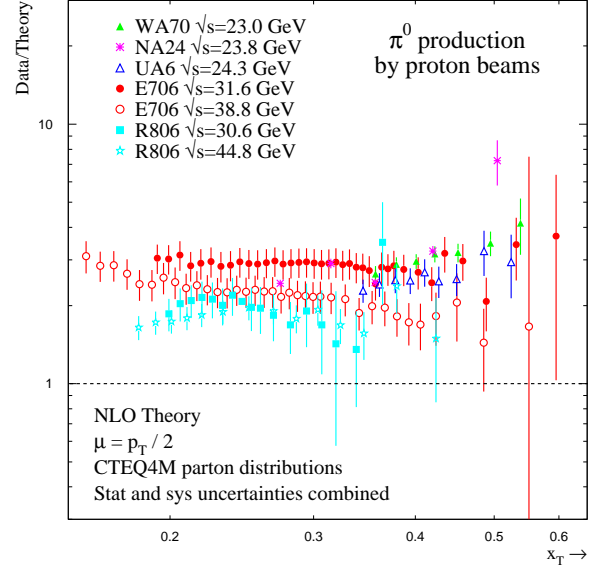


Figure 15. Comparison between proton-induced π^0 data and NLO pQCD calculations for several experiments as a function of x_T .

with the data on high-mass pairs (Fig. 5), can accommodate both the shapes and normalizations of direct-photon and π^0 inclusive cross sections.

Comparisons between direct-photon data from E706 [45], WA70 [46, 47], and UA6 [48] and k_T -enhanced NLO pQCD [24] are shown in Figs. 13 and 14. The values of $\langle k_T \rangle$ were based on the data for high-mass pairs from E706 (Fig. 5), and the di-photon data from WA70 [49, 32] ($\langle k_T \rangle = 0.9 \pm 0.1 \pm 0.2$ GeV/c). The center-of-mass energies for WA70 and UA6 ($\sqrt{s} \approx 24$ GeV) are smaller than those for E706. Correspondingly, $\langle k_T \rangle$ values for these experiments are expected to be slightly smaller than the values required for E706 (Fig. 3).

A recent survey of π^0 production found that current NLO pQCD calculations significantly undershoot the data [26]. A comparison between π^0 data and NLO pQCD is shown in Fig. 15 for several experiments [50]. The data are consistently a factor of 2 to 3 above theory. The above phenomenological model should also be valid for pion production. Using $\langle k_T \rangle$ similar to, but slightly higher than that for direct photons, good agreement is obtained for π^0 's measured by E706 [45], WA70 [51], and UA6 [52] (Figs. 16 and 17). The k_T -enhanced predictions compare well with the π^0 cross sections, with all the E706 and UA6 direct-photon data, and with the π^- beam direct-photon cross sections of WA70.

Since k_T -smearing affects similarly direct-photon

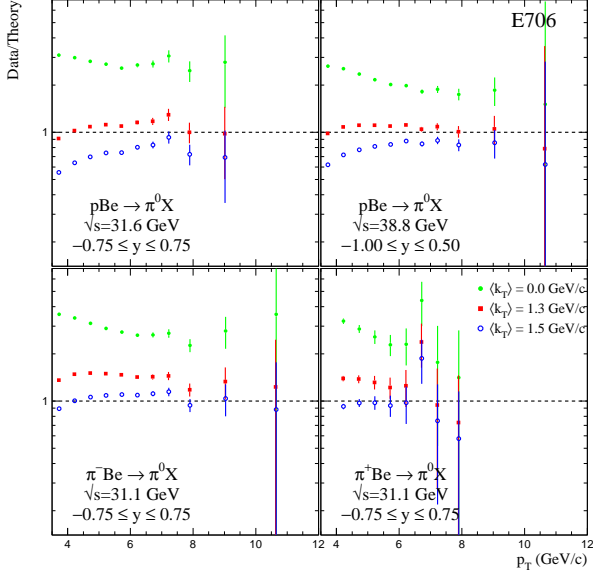


Figure 16. Comparison between the E706 π^0 data and NLO pQCD calculations with and without k_T enhancements, for several values of $\langle k_T \rangle$.

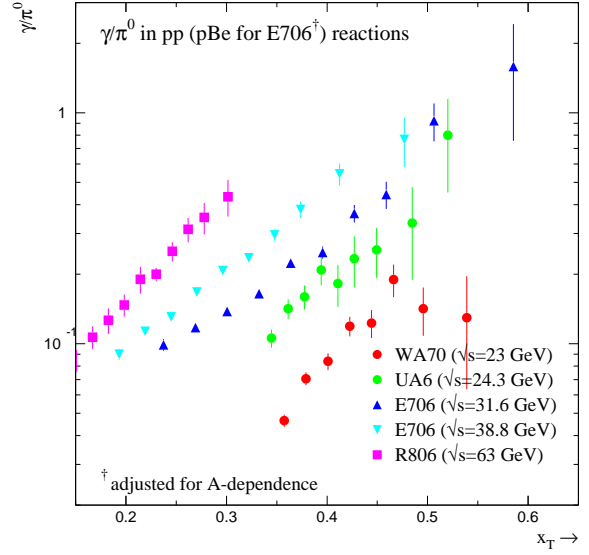


Figure 18. Ratios of direct-photon cross sections to the π^0 cross sections as a function of p_T for various experiments at several values of \sqrt{s} .

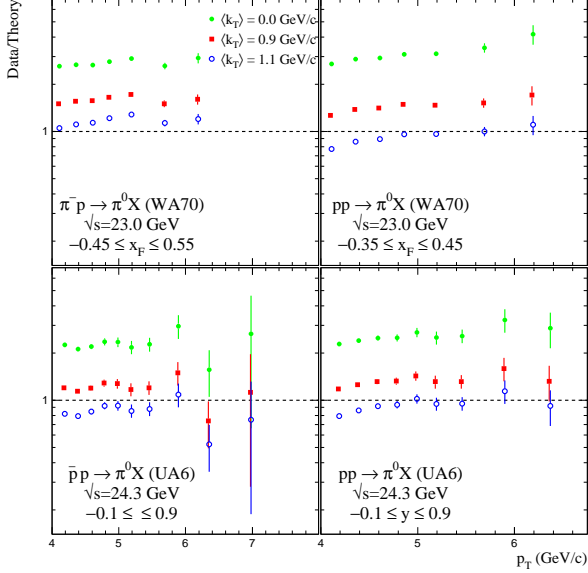


Figure 17. Comparison between the WA70 and UA6 π^0 data and an NLO pQCD calculation with and without k_T enhancements, for several values of $\langle k_T \rangle$.

and π^0 data, the ratio of direct-photon to π^0 production should be relatively insensitive to k_T . Experimental and theoretical uncertainties also tend to cancel in such ratios. Figure 18 shows the ratios of cross-sections [50] for direct-photon to π^0 production for WA70, UA6, E706, and R806 [53, 54, 55]. The results from WA70 (Fig. 19) and UA6 (Fig. 20), at approximately the same \sqrt{s} , appear to differ significantly. The ratio for NLO theory differs from that of WA70 by a factor of three, but only by $\approx 30\%$ from the UA6 data. The WA70 and UA6 π^0 results agree (Fig. 15) and most of the difference is therefore in the direct-photon cross section. Similar γ/π^0 comparisons are shown for E706 at $\sqrt{s} = 38.8$ GeV (Fig. 21) and R806 at $\sqrt{s} = 63$ GeV (Fig. 22). The same 30% level of agreement can also be found for the E706 data at $\sqrt{s} = 31.6$ GeV and the R806 data at $\sqrt{s} = 31$ GeV and 45 GeV.

The discussion of direct-photon data from fixed-target and ISR experiments [25], while rejecting the k_T interpretation for the observed deviations, pointed to limitations for the applicability of NLO calculations at lower- p_T values and to inconsistencies among experiments used in comparisons to NLO theory. Given the shortcomings of a purely NLO description, a global comparison of the available data to fully resummed theory may provide useful insights into these issues.

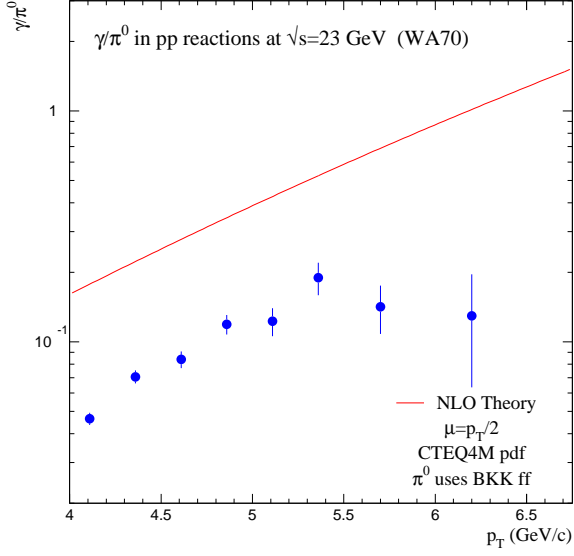


Figure 19. γ/π^0 comparison for the WA70 pp data at $\sqrt{s} = 23$ GeV. Overlaid are the results from the NLO pQCD calculations.

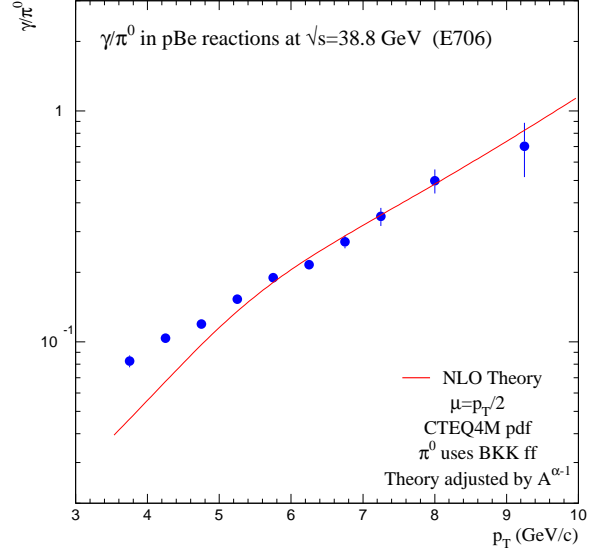


Figure 21. γ/π^0 comparison for the E706 pBe data at $\sqrt{s} = 38.8$ GeV. Overlaid are the results from the NLO pQCD calculations.

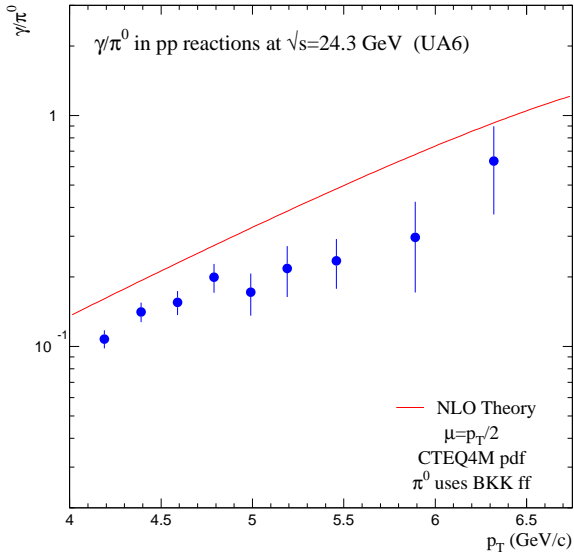


Figure 20. γ/π^0 comparison for the UA6 pp data at $\sqrt{s} = 24.3$ GeV. Overlaid are the results from the NLO pQCD calculations.

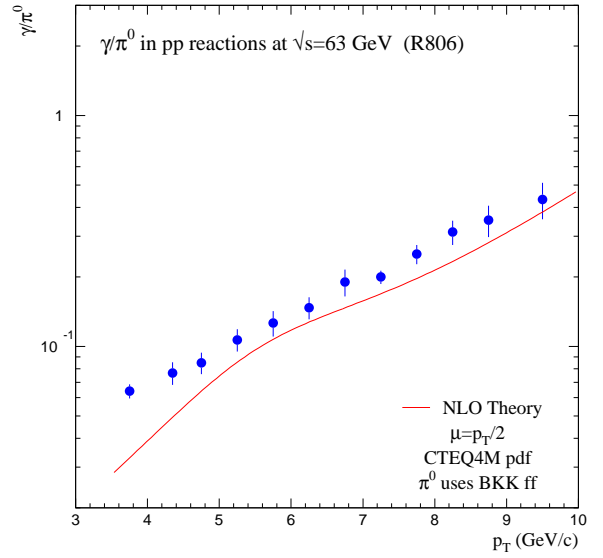


Figure 22. γ/π^0 comparison for the R806 pp data at $\sqrt{s} = 63$ GeV. Overlaid are the results from the NLO pQCD calculations.

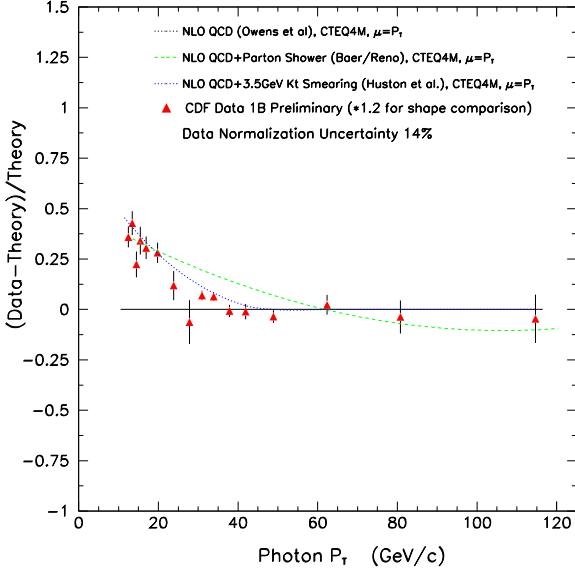


Figure 23. A comparison of the CDF isolated direct-photon data at $\sqrt{s} = 1.8$ TeV from Run Ib with a NLO pQCD prediction and two implementations of soft gluon corrections to the NLO prediction [56].

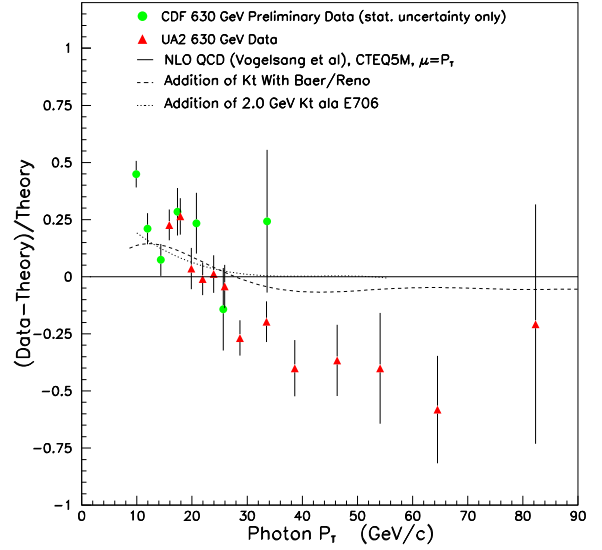


Figure 25. A comparison between CDF and UA2 data at $\sqrt{s} = 630$ GeV.

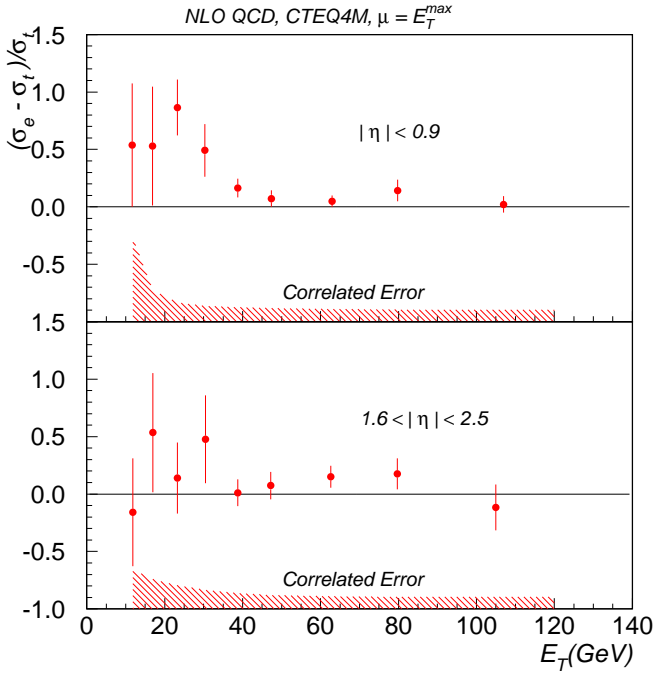


Figure 24. A comparison of the $D\phi$ isolated direct-photon data at $\sqrt{s} = 1.8$ TeV from Run Ib with a NLO pQCD calculation in both the central and forward rapidity regions [57].

Run I Results

The consequences of k_T smearing are expected to depend on \sqrt{s} (Fig. 3). At the Tevatron collider, where p_T is large compared to k_T , the above model of soft-gluon radiation leads to a relatively small modification of the NLO cross section. Only the lowest end of the p_T spectrum is modified significantly, and the K-factor exhibits the expected $\sim 1/p_T^2$ behavior for a power correction.

A comparison of the results from Run Ib, shown in Figs. 23 and 24 [56, 57], confirms the expected deviation in shape at low p_T . Using di-photons, CDF has measured $\langle k_T \rangle = 3.6 \pm 0.8$ GeV/c at $\sqrt{s} = 1.8$ TeV [33]. Employing this value, the phenomenological model adequately describes the shape of the data in Fig. 23. Also shown in this figure is an implementation of soft-gluon corrections using an enhanced parton shower [22]. The phenomenological- k_T model provides a better agreement with data than is available in the enhanced parton shower model. The agreement between the phenomenological model implementation of k_T smearing and the direct-photon data can also be seen in preliminary results from CDF at $\sqrt{s} = 630$ GeV (Fig. 25).

The CDF data in Fig. 23 have been normalized upwards by a factor of 1.2 for the benefit of a shape comparison. Without this normalization, then the CDF data lie below the NLO pQCD calculation at high p_T . Figure 25 also contains a comparison between CDF

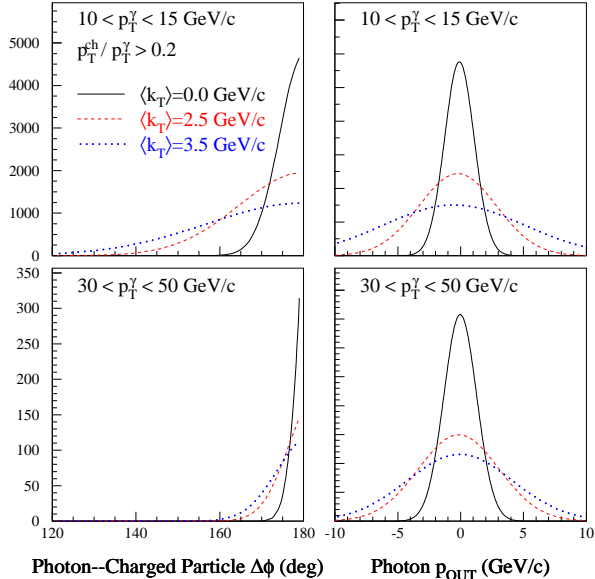


Figure 26. Left: Distributions of azimuthal angle difference $\Delta\phi$ between the direct photon and a recoil charged track for several values of k_T and for two photon p_T ranges. Right: Similar dependences for the photon p_{OUT} .

and UA2 [58, 59] data at $\sqrt{s} = 630$ GeV, where a similar deficit is observed at high p_T for the UA2 data. There is currently no explanation for this effect.

2.1.5. Expectations for Run II

k_T Studies at Low- p_T

To study the level of k_T induced by multiple gluon emissions at the collider, the experiments have employed the relatively low-statistics di-photon data. In Run II, both CDF and DØ will have precision magnetic tracking, which will permit studies of k_T effects using “two-arm” data on pairs consisting of a direct photon and a recoil charged track, in a spirit similar to that of the fixed-target investigations of $\gamma\pi^0$ and $\pi^0\pi^0$ pairs discussed before. The advantage of this approach is that it will obviate the need for jet reconstruction (difficult at low p_T), and minimize complications from jet energy scale calibration. Of course, photon+jet systems are also of interest, but may be harder to study in the range of interest for checking the effects of k_T smearing.

We simulated the expected behavior of photon-track systems using the same LO Monte Carlo [38] employed in previous fixed-target studies. The results are illustrated in Fig. 26 for $\Delta\phi$ and p_{OUT} of the photon, for two representative ranges of photon p_T that span the region where the k_T effects appear to be important in

the inclusive photon cross sections from Run I. (For the measurement of p_{OUT} for photon, the scattering plane is defined by the colliding beams and the recoil track.) The sensitivity to the value of $\langle k_T \rangle$ in the range of 0 to 3.5 GeV/c is clearly seen for both variables. The $\Delta\phi$ distributions become narrower with increasing photon p_T , as expected from simple kinematic arguments. For a fixed $\langle k_T \rangle$, the width of the p_{OUT} distributions is relatively insensitive to p_T , and can therefore be particularly useful for mapping out the dependence of k_T on event kinematics (especially on the p_T of the photon). To properly interpret the widths of such distributions in terms of k_T induced by gluon-radiation, it is important to subtract the amount generated in the fragmentation of partons into the charged particles (as was done in the fixed-target analyses).

Additional handles on interpreting the data can be obtained through studies of p_T distributions of charged particles from fragmentation of partons recoiling against direct-photon triggers. In the presence of significant initial-state k_T , such distributions are expected to become softer than expected from standard fragmentation functions (determined *e.g.* from e^+e^- data), since the k_T -kick tends to increase the photon p_T while taking it away from the recoil side. This should be observed most clearly at low photon p_T 's, where the effect from k_T is greatest.

Photon Purity

The particularly interesting connection between two-arm studies and measurements of the inclusive photon cross section is mainly at relatively low p_T (10 GeV/c to 35 GeV/c), where Run I results indicate significant deviation of the cross section from expectations from NLO pQCD (Figs. 23 and 24). This is also the region of high statistics, and, consequently, where detailed studies will be possible. It is therefore important to achieve a high photon-signal purity in this region, which has proved to be difficult in Run I.

In the case of DØ, calorimeter response will be modified in Run II by the presence of a central solenoid magnet and preshower detectors [60]. The separation of photon signal and background in Run I was based on the fraction of electromagnetic energy detected in the first longitudinal layer of the calorimeter (E_{EM1}/E_{TOT}). This quantity is particularly sensitive to differences in the early stages of shower development initiated by single photons, and by photons from decays of π^0 's of the same p_T . In the Run II configuration, the signal-background discrimination based on this variable is expected to deteriorate, but simulations indicate [61] that Run I performance can be recovered by using instead the fraction of energy deposited in

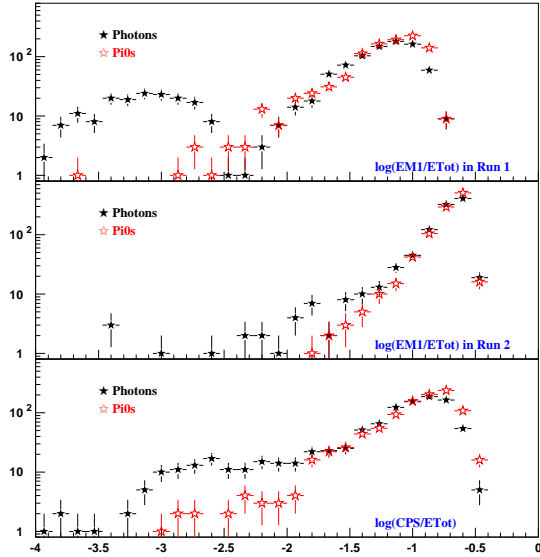


Figure 27. Comparisons of simulated discriminations between photons (solid) and π^0 's (open) for the $D\emptyset$ detector in the Run I configuration (top, discriminant variable is $\log(E_{EM1}/E_{TOT})$); for the same discriminant in the Run II configuration (middle); and for the Run II configuration and $\log(E_{CPS}/E_{TOT})$ discriminant (bottom).

the preshower detectors (E_{CPS}/E_{TOT}), as illustrated in Fig. 27 for photons at central rapidities. Using the fine-grained shower-profile information from the preshower strips (ca. 7 mm triangles), an additional factor of two rejection of background (while maintaining high signal-efficiencies) has been achieved in our Monte Carlo simulations [61]. As illustrated in Fig. 28, multiple preshower clusters for sufficiently large separation between photons from meson decays can be resolved, or inferred from the widths of clusters when the showers are not fully separated. Results are shown for $p_T \approx 15$ GeV/c and $\eta \approx 0.95$, where the separation of photon signal from background is particularly difficult. Another variable useful for the discrimination is the distance in the $R-\phi$ plane between the detected CPS cluster and the photon position (the latter calculated from the primary vertex and the position of the calorimeter cluster) [62]. Figure 29 shows this distribution for $p_T \approx 15$ GeV/c and $\eta \approx 0.1$.

Even higher background rejection can be achieved by exploiting correlations between the calorimeter and preshower shower profiles in a covariance-matrix approach. A study was undertaken using a simplified version of the Run I covariance matrix, with added preshower variables [62]. Figure 30 shows the E_T

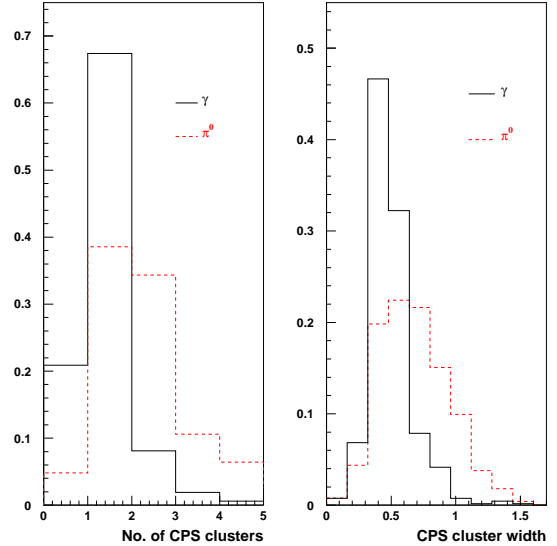


Figure 28. Additional γ vs π^0 discrimination with the $D\emptyset$ detector in Run II is possible using differences in the respective distributions for the number of reconstructed preshower clusters matched with the calorimeter shower (left) or for the width of the preshower cluster (right). Solid lines are for γ 's, dashed for π^0 's.

dependence of the π^0 efficiency for χ^2 cutoffs corresponding to 90% and 60% photon efficiency.

In the central region, CDF tools for γ -background separation in Run I (shower width in the electromagnetic shower-maximum detector, and conversion in the central-preradiator detector) will remain the same. These tools provide a clear separation of the photon signal and the π^0 -dominated background. The addition of a new scintillator-based endplug calorimeter with a preshower and shower-max detector will offer an extension of these tools to the forward region in Run II.

Thus, we expect a better signal purity at low p_T in Run II than was achieved in Run I, which will facilitate more precise measurements of low- p_T direct photons and di-photons.

Photons at High- p_T

At high values of p_T , separating the direct-photon signal from background and the expected reach in p_T are determined by the collected luminosity. As shown in Sec. 2.2, for the initial luminosity of 2 fb^{-1} , the inclusive direct-photon cross section measurement can be extended beyond 300 GeV/c. While the high- p_T data will permit detailed tests of perturbative QCD, it is not expected to be sensitive to differences in recent

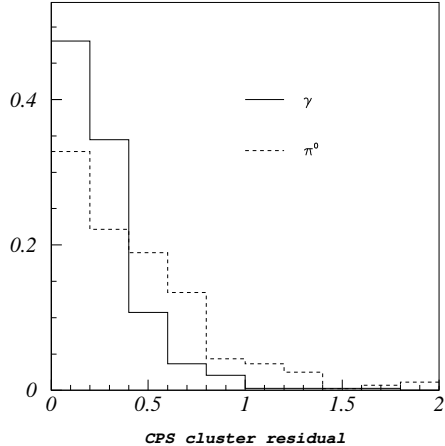


Figure 29. The residual of CPS cluster position relative to the photon or π^0 in the R- ϕ plane in the DØ detector. Clusters from π^0 's have larger residuals, especially when one of the decay photons does not convert in the solenoid.

parameterizations of gluon distributions at large x (eg., CTEQHJ and CTEQM). Thus, the determination of the large- x gluon distribution will have to continue to rely on direct-photon data from fixed target experiments and on jet data at the Tevatron.

2.1.6. Impact on the Gluon Distribution

The largest uncertainty in any parton distribution function (PDF) is that for the gluon distribution. At low x , the gluon can be determined indirectly from scaling violations in quark distributions, but a direct measurement is required at moderate to large x . Direct-photon production has long been regarded as potentially the most useful source of information on the large- x part of the gluon distribution. And direct-photon data, especially from CERN fixed target experiment WA70, have been used in several global analyses [21, 63]. Another process sensitive to the gluon distribution, through the gluon-gluon and gluon-quark scattering subprocesses, is jet production in hadron-hadron collisions. Precise data from Run I are available over a wide range of transverse energy and, indeed, provide a constraint on the gluon distribution in an x range from about 0.05 to 0.25. However, the low statistical power of the jet cross section at high E_T , and the dominance of the $q\bar{q}$ scattering subprocess in that kinematic region, do not provide for a similar constraint at large x .

Figure 31 shows several gluon parton distribution functions [18] that provide a reasonable fit to the DIS and DY data used in the CTEQ4 fits [19]. The excursions shown (normalized to the CTEQ4M

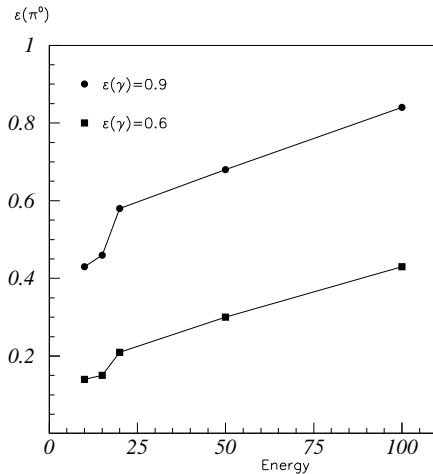


Figure 30. Efficiency for a π^0 to pass covariance matrix χ^2 cuts corresponding to photon efficiencies of 90% and 60%. (Preliminary study for the DØ detector in Run II.)

gluon) provide an estimate of the uncertainty in the gluon distribution. The gluon distribution seems reasonably well-constrained by these data, except at large x . Also shown in Fig. 31 are the gluon distributions from CTEQ5HJ [64] (which best fits the Tevatron high- E_T jet data) and three recent MRST PDF's [21]. The MRST PDF's incorporate the WA70 direct-photon data using the k_T -enhancements described above. Nevertheless, the theoretical problems associated with direct-photon production have discouraged the CTEQ collaboration from using the direct-photon data in their recent fits [64]. The recent work on resummation offers hope that this situation will change.

The CTEQ4HJ PDF's were determined by increasing the weight for the CDF jet cross section at high E_T [19]. In the resultant fit, the increase was achieved through a significant increase in the gluon contribution at large x , without inducing serious conflicts with any of the other experiments used in the CTEQ4 data sets. This increase was allowed by the uncertainty in the gluon distribution in this x range, a flexibility not present for any of the quark distributions. Another demonstration of the uncertainty in the gluon distribution at large x can be seen in Fig. 32, where the CTEQ4HJ gluon distribution is plotted along with that of CTEQ4M and three recent MRST PDF's. At $x \approx 0.6$, there is over an order of magnitude spread between the CTEQ4HJ and the MRST $g \downarrow$ gluon distributions.

The CTEQ4HJ gluon distribution (and its successor, CTEQ5HJ) provides the best description of not only the CDF jet cross section, but that of DØ as well. At

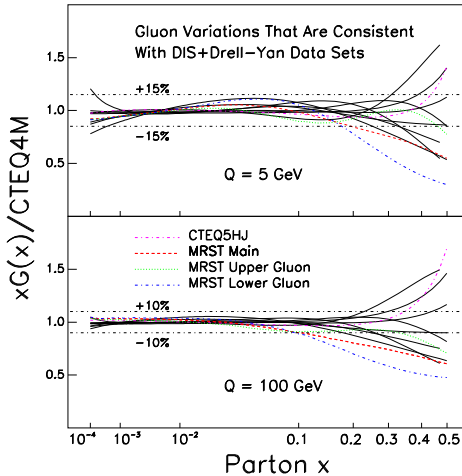


Figure 31. The ratio of gluon distributions obtained in the study in Ref. [18] to the CTEQ4M gluon at two different Q scales. All of these gluon distributions correspond to PDF's which provide a reasonably good fit to the CTEQ4 DIS/DY data set.

$x \approx 0.5$, corresponding roughly to $E_T \approx 450$ GeV for central η , a doubling of the gluon distribution (compared to CTEQ4M) results in only a 20% increase in the inclusive jet cross section. On the other hand, the fixed-target direct-photon yield of E706, produced mainly through gq scattering, is proportional to the gluon distribution. A fit using the E706 direct-photon data and the k_T K-factors is also shown in Fig. 32; this result is very similar to the CTEQ4M gluon. At the highest reach of the E706 data, the CTEQ4HJ gluon distribution is a factor of 4 to 5 larger than the CTEQ4M gluon. With the advent of more complete theoretical treatments [17] of direct-photon production, the E706 data should have great impact on the determination of the behavior of the gluon at large x . This would have implications not only for fixed-target direct-photon data, but also for collider physics at highest Q^2 scales.

2.1.7. Conclusions

Direct-photon physics remains a viable and interesting program for Run II of the Tevatron. The Run II measurements of single and double direct photons, and of photon and jet or single track correlations, will reach larger p_T and have improved detection efficiency at low p_T , compared to Run I. Although the data are not expected to improve directly our knowledge of the gluon distribution at intermediate and large x , it can do so by providing a testing ground for newly developed theoretical models and formalisms, and by helping

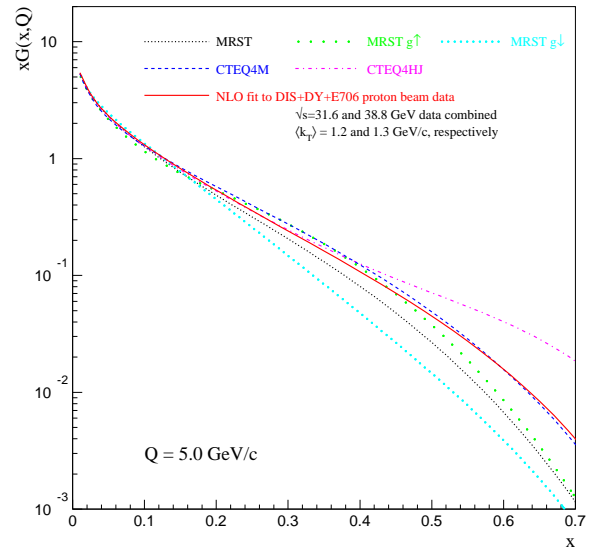


Figure 32. A comparison of the CTEQ4M, MRST, and CTEQ4HJ gluons, and the gluon distribution derived from fits that use E706 data [24]. The $g \uparrow$ and $g \downarrow$ gluon densities correspond to the maximum variation in $\langle k_T \rangle$ that MRST allowed in their fits.

clarify the currently confused role that multiple gluon emission play in direct-photon production (and other high- p_T processes). Once this physics is properly understood, the existing fixed-target data should provide one of the best constraints on the gluon distribution, as has been envisioned for a long time.

We have examined the best available experimental information on production of single and double direct photons (and mesons) at large p_T in both fixed-target and collider energy regimes. Recent theoretical developments offer optimism that the long-standing difficulties in the proper description of these processes can finally be resolved. While there is still no final consensus, the trend of recent developments has led to an increased appreciation of the importance of the effect of multiple gluon emission, and to the emergence of tools for clarifying this issue.

To summarize, measurements of the production of high-mass pairs of high- p_T particles at WA70, E706, CDF, and DØ provide consistent evidence for the presence of large k_T . NLO pQCD calculations [8], which include effects due to the radiation of a single hard gluon, compare poorly to k_T -sensitive distributions in di-photon data. RESBOS [10], a NLO pQCD calculation, which also includes the effects of multiple soft-gluon emission through the CSS resummation technique, compares well with the shape of the di-photon data. LO pQCD calculations [37, 38]

that incorporate k_T effects through Gaussian smearing techniques, provide reasonable characterizations of distributions for pairs of direct photons and mesons.

While the apparent inconsistencies between different direct-photon and π^0 data sets are not understood [24, 25, 26], we found it instructive to consider results on the γ/π^0 ratio from WA70, UA6, E706, and R806. Various experimental and theoretical uncertainties tend to cancel in such a ratio, which is also relatively insensitive to k_T -effects. We find that the ratio from theory agrees to $\approx 30\%$ with data from UA6, E706, and R806 over the range $24 \text{ GeV} < \sqrt{s} < 63 \text{ GeV}$.

LO pQCD has been used to estimate the impact of k_T on the inclusive production of high- p_T direct photons and π^0 's. This simple phenomenological model is able to account for differences between NLO pQCD calculations and inclusive data over a wide range in \sqrt{s} . While the approximate nature of such models is clear, and has been discussed in several recent papers, the emerging formalism for the full (threshold and recoil) resummation of inclusive direct-photon cross sections appears to vindicate much of the understanding of effects from multiple gluon emission that has been achieved using approximate tools. The resummation formalism can be expected to provide a solid foundation for the treatment of k_T , at which time a global reexamination of parton distributions, with an emphasis on the determination of the gluon distribution from the direct-photon data, should become possible [65].

2.2. Direct Photon Production at the Tevatron¹

2.2.1. Introduction

In this section we summarize features of direct photon production which are relevant in the kinematic range to be covered in Run II. In Sec. 2.2.2, a comparison between Run I data and the corresponding theoretical description is presented. Several potential problem areas are noted. Sec. 2.2.3 contains a brief description of the kinematic reach expected for Run II, based on an integrated luminosity of 2 fb^{-1} . Included here is a discussion of the sensitivity to parton distribution functions and to what extent direct photons at Run II can help constrain the gluon distribution. In Sec. 2.2.4 some predictions for photon-jet correlations are presented. The potential of observables other than the usual single photon p_T distribution to help elucidate the underlying dynamics is also discussed.

2.2.2. Comparison to Run I Data

Data for the inclusive cross section for direct photon are available over a wide range in energies from fixed

target and collider experiments. By now it is well known that it has not yet been possible to simultaneously describe all of the experimental results with a next-to-leading-order (NLO) QCD calculation. A pattern of discrepancies between theory and experiment exists in both the fixed target and the collider data sets. This situation has been reviewed in [23, 24, 25]. An analysis similar to that for direct photon production in Ref. [25] has been performed for the case of π^0 production [26]. The two processes are closely related since π^0 's decaying to two photons provide much of the background which must be dealt with when extracting the signal for direct photon production. Some of these issues are also dealt with in Sec. 2.1 where a detailed comparison to fixed target data is also presented. While it is clearly of interest to understand direct photon production over the entire range of available energies, this section will focus on those aspects of the data which can most directly be addressed during Run II. The first step is to examine the theoretical description of the data from Run I.

A comparison of NLO QCD predictions to the direct photon data from CDF and DØ has indicated the presence of a deviation of the data from theory at low values of transverse momentum [23, 24]. This deviation decreases if the effects of soft gluon radiation are taken into account by applying a Gaussian k_T smearing model using a value of $\langle k_T \rangle$ measured in di-photon production in the two experiments.* Such a k_T treatment is phenomenologically motivated.

Recently, there has been progress in more sophisticated treatments of soft gluon radiation near threshold in the parton-parton scattering process [14, 66, 13]. At large values of transverse momentum for the photon, the phase space for the emission of additional gluons in the hard scattering is limited. This limitation on the emission of real gluons upsets the balance in the theoretical expressions between virtual and real emission contributions. The result is large logarithmic corrections near the threshold for the parton-parton scattering subprocesses. These large corrections can be resummed in a relatively compact formalism. The results [12, 66, 13] indicate that the corrections to existing next-to-leading-order calculations are large as $x_T = 2p_T/\sqrt{s}$ approaches 1. Away from the region at the edge of phase space it is observed that the corrections to the NLO results coming from the threshold resummation are relatively small over much of the x_T range covered in the fixed target experiments when the renormalization and factorization scales are chosen to be $p_T/2$ and the resummed results show an overall reduction in the sensitivity to the choices

*The value of k_T can be directly measured in di-photon events since the photon 4-vectors can be measured precisely.

¹ Contributed by: J. Huston and J.F. Owens

of these scales. However, the threshold resummation corrections alone are not sufficient to explain the discrepancies observed between the theoretical predictions and some of the fixed target experimental results. In addition, threshold resummation cannot explain the deviations observed by $D\bar{O}$ and CDF at the low p_T end of the measured distributions.

Another approach to resumming soft gluon effects is that of Ref. [27] which uses the DDT [67] or q_T -space method. This technique has recently been applied to vector boson production [68] and compared with the impact parameter method of Ref. [44]. In Ref. [27] a parton-parton luminosity function is defined which depends on the net transverse momentum of the pair of colliding partons. The parton distributions are probed not at the scale of the hard scattering process, but instead at a scale given by q_T . This means that the scale of the parton distributions is typically somewhat smaller than, for example, the transverse momentum of the produced photon. This results in an enhancement of the cross section. In addition, the parton transverse momentum is taken into account when the final photon p_T is calculated. Some enhancement of the fixed target predictions is noted using this technique, but it is insufficient to fully describe all of the fixed target data. For the collider energy range, Ref. [27] quotes only a small effect, which does not appear to be sufficient to explain all the observed deviations. At present, the resummation is done only with the leading-log terms included. More results from this technique are anticipated as next-to-leading-log terms are included as well.

Quite recently a new formalism for simultaneously incorporating both the threshold resummation *and* the resummation of k_T (or recoil) effects has been developed [17]. This formalism possesses the desirable property of simultaneously conserving both energy and momentum in the resummation process. The initial results presented in [17] indicate that the threshold enhancement referred to above is correctly reproduced while, in addition, there is a large enhancement due to the newly included recoil effects. Detailed applications and studies of the scale dependence and the dependence on non-perturbative input parameters are expected soon.

The initial indications of discrepancies between theory and experiment in the collider data came from results taken in Run Ia. A comparison of the higher statistics results from CDF in Run Ib, shown in Fig. 23, confirms the shape deviation at low p_T and the agreement with the k_T smearing correction obtained using the Gaussian smearing model. (Also shown is an attempt to implement the soft gluon corrections using an enhanced parton shower [22]. In this case, the effect seems to drop off more slowly than the deviation ob-

served in the data.) Note that the k_T smearing correction falls off roughly as $1/p_T^2$, as expected from a power correction type of effect. This is not true in the case of fixed target experiments, as discussed in Sec. 2.1, where the steeply falling parton distribution functions enhance the effects of the soft gluon radiation.

The $D\bar{O}$ direct photon cross section for the central region is also consistent with such a deviation at low p_T [57], as shown in Fig. 24 while no conclusion can be reached for the $D\bar{O}$ cross section in the forward region (see the lower half of Fig. 24 and Ref. [57]). The possibility that the discrepancy between theory and experiment may be dependent on rapidity is interesting and is one that can be investigated in more detail with the higher statistics expected from Run II.

In an attempt to achieve a better theoretical description of the data it is important to investigate what flexibility exists within the conventional QCD hard scattering NLO formalism. In order to perform perturbative QCD calculations, one must specify the renormalization and factorization scales. For the latter, there are two scales, corresponding to the factorization of collinear singularities for the initial state parton distributions and the final state fragmentation functions. For most hard scattering calculations these three scales are chosen to be proportional to the characteristic large transverse momentum - that of the photon in this case. Often, all three scales are set equal to each other. However, this latter step is not necessary and it is reasonable to ask whether or not one can describe the shapes of the CDF and $D\bar{O}$ data in the region below $p_T = 30$ GeV by a suitable variation of all three of the scales [69]. In Fig. 33 the Run Ib CDF data are compared to several curves corresponding to different choices of the renormalization and factorization scales. One can see that it is possible to get a steepening of the slope at the low- p_T end, but only at the price of an increase in the overall normalization. Apparently, it is not possible to get both the shape and the normalization correct by such a strategy.

In Fig. 23, the CDF data has been normalized upwards by a factor of 1.2 for an easier shape comparison. If this normalization is taken out, as shown in Fig. 34, it is evident that the data fall below the NLO QCD prediction at high p_T . Also shown is a comparison to the CDF photon data taken at $\sqrt{s} = 630$ GeV and the photon data from UA2 [59] where a similar deficit is observed at high p_T . For most observables, typically, the data lie above the NLO QCD predictions so this is somewhat of an unusual situation. It is interesting to note that a measurement of the photon fraction (of the photon candidate sample) indicates that the photon fraction seems to be leveling off at approximately 80%, rather than saturating the sample at near 100% at high

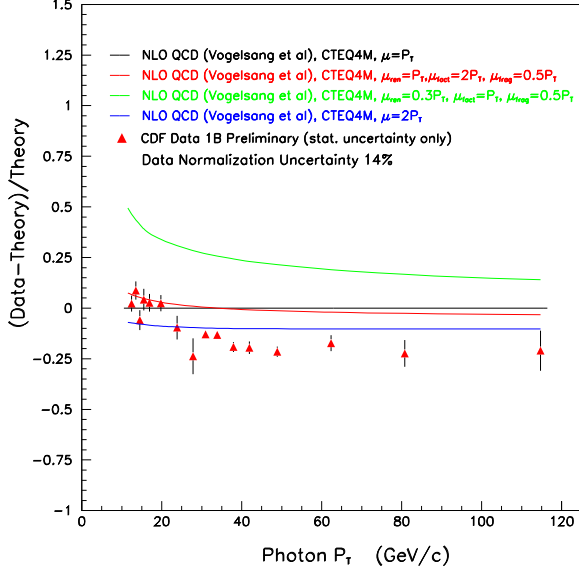


Figure 33. Comparison of the CDF Run Ib data with several NLO curves corresponding to different choices of the renormalization and factorization scales.

p_T . The latter outcome would be predicted from very basic considerations: with a fixed E_T isolation cut, jets are required to fragment into a π^0 with a higher z value as the p_T of the photon candidate increases. Such a fragmentation is suppressed by the sharp falloff of the fragmentation function at high z . It will be interesting and important to understand this behavior. The increased statistics of Run II will allow both the low p_T and high p_T regions to be investigated more thoroughly.

2.2.3. Expectations for Run II

For the purposes of this section we shall assume an integrated luminosity for Run II of 2 fb^{-1} . As noted in Sec. 2.2.2, the data on direct photon production from Run I extend to a transverse momentum of approximately 120 GeV. The increased statistics expected from Run II greatly extend this range as shown in Figs. 35 and 36. These figures have been generated using the next-to-leading-logarithm program of [70] with the CTEQ5M [64] parton distributions and with the renormalization and factorization scales set equal to $p_T/2$. The errors shown are statistical only and the results are presented for the transverse momentum range where more than 10 events are expected in a 10 GeV bin of p_T with a total integrated luminosity of 2 fb^{-1} and 4 fb^{-1} , respectively. No efficiency/acceptance corrections, however, have been applied to these estimates. Typically, these corrections

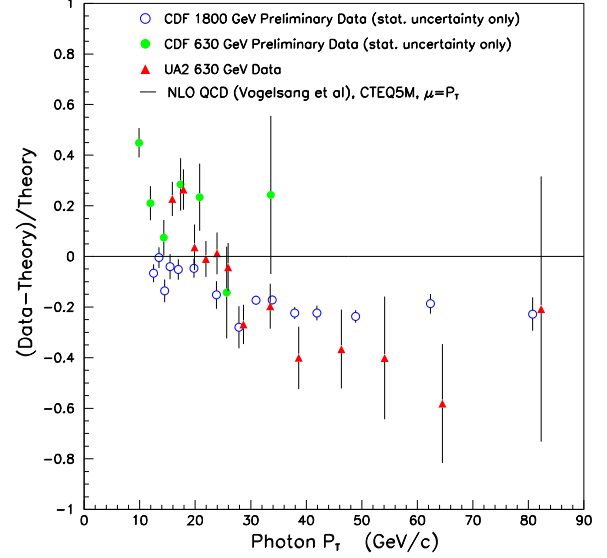


Figure 34. A comparison of the CDF photon data from Run Ib (at both $\sqrt{s} = 630 \text{ GeV}$ and $\sqrt{s} = 1800 \text{ GeV}$) with a NLO QCD prediction and the direct photon data from UA2.

are on the order of 50%.

One can see that the range of useful statistics extends past 300 GeV in the first case and past 350 GeV in the second. This extended coverage in p_T corresponds to an increased range of sensitivity for the values of the parton momentum fractions of the colliding hadrons. Recall that the inclusive cross section for single photon production in the central region is sensitive to average values of the parton momentum fraction x approximately equal to $x_T = 2p_T/\sqrt{s}$. A range of x_T out to about 0.3 will be covered, corresponding to a similar range of $\langle x \rangle$ for the parton distributions. This extended range suggests that the relative ratios of the underlying subprocesses should change significantly over the p_T range to be covered. To investigate this, the inclusive cross section is displayed in Fig. 37 along with the contributions from the various parton scattering subprocesses. For ease of comparison, the same results are shown in Fig. 38 on a linear scale relative to the total rate. The results in both of these figures were generated using the leading-logarithm approximation with the CTEQ5L parton distributions. The leading-log approximation was chosen so that the separation between the point-like and fragmentation contributions would be unambiguous. Processes with two or more partons in the final state in addition to the photon can populate regions of phase space where the photon is collinear with one of the par-

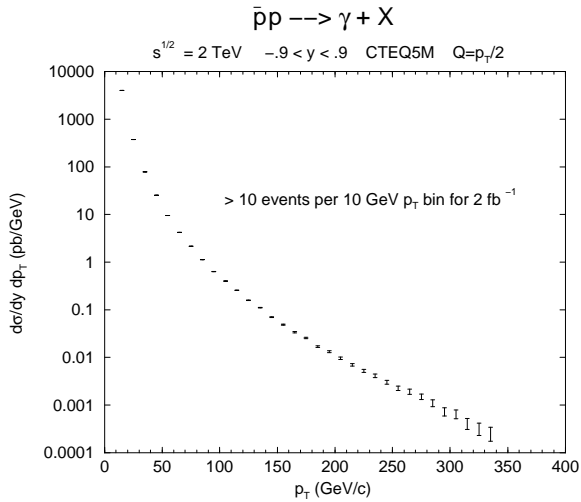


Figure 35. Direct photon p_T distribution for Run II with errors based on an integrated luminosity of 2 fb^{-1} .

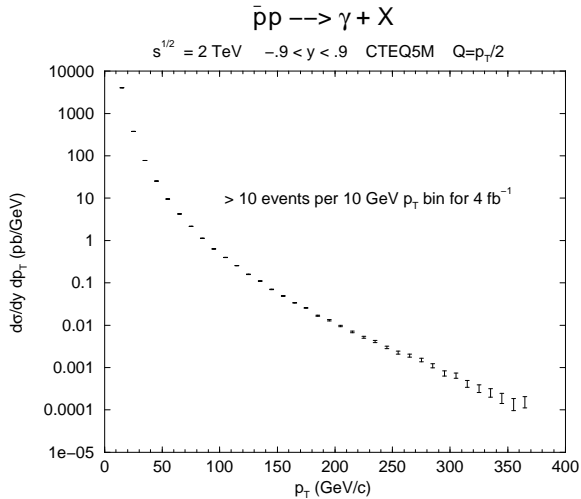


Figure 36. Direct photon p_T distribution for Run II with errors based on an integrated luminosity of 4 fb^{-1} .

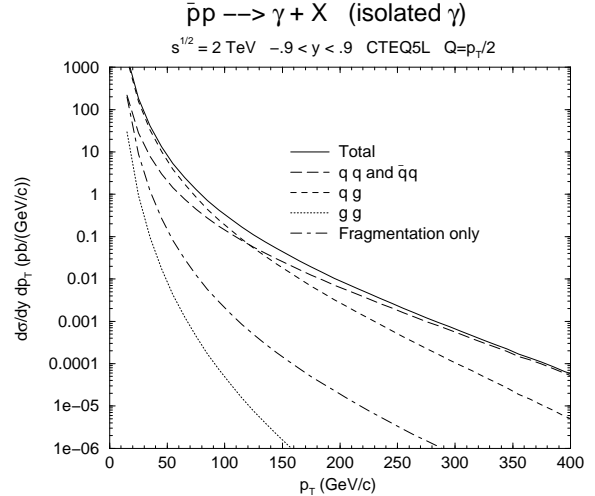


Figure 37. Contributions of the various subprocesses for direct photon production calculated in the leading-log approximation using the CTEQ5L parton distributions.

tions. These topologies correspond to the fragmentation process. Thus, the higher order terms mix the contributions from the point-like and fragmentation (or bremsstrahlung) components. One must define, through the use of appropriate experimental cuts, precisely what is meant by the bremsstrahlung component. For the purposes of the discussion being presented here the leading-log predictions are sufficient. Note that the magnitude of the next-to-leading-order corrections relative to the leading-log predictions for the choice of scale used here ($p_T/2$) is slowly varying over the kinematic region being studied, as shown in Fig. 39.

The results shown in Figs. 37 and 38 illustrate several points worth noting. First, the fragmentation component is expected to be a negligible fraction of the total rate. This is due primarily to the imposition of an isolation cut which rejects events with more than 1 GeV of hadronic energy accompanying the photon in a cone of radius 0.4 about the photon direction.[†] Such a cut is necessary experimentally in order to control the copious background to the photon signal from jets fragmenting into π^0 's. This cone isolation energy is almost completely saturated by the underlying event energy accompanying the hard scatter, leaving little room for

[†]This cut was used for the CDF Run Ib direct photon measurements. The value of the isolation energy cut in Run II will have to be increased somewhat due to the contributions to the isolation energy from the larger number of minimum bias events expected in the same crossing.

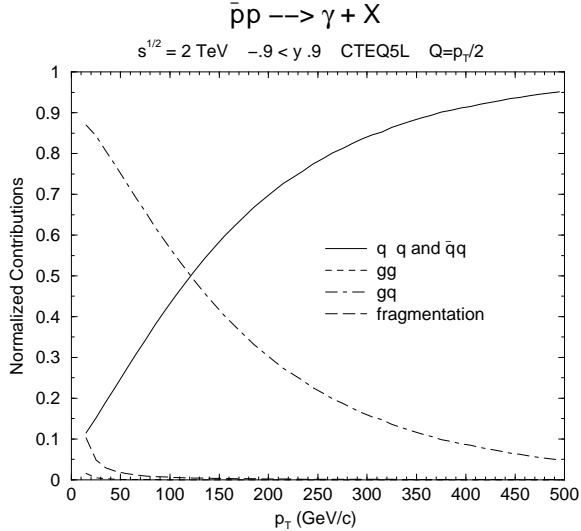


Figure 38. The same results as shown in Fig. 37 except on a linear scale and normalized to the total rate at each value of p_T .

energy from the fragmentation of the jet. Note that the precise value of the fragmentation contribution relative to the total rate will vary as one includes higher order effects, but the overall contribution is still expected to be small. Next, one sees the dominance of the $q\bar{q} \rightarrow \gamma q$ subprocess in the region out to about 100 GeV in p_T , *i.e.*, the range covered by the Run I data. Beyond this range the $q\bar{q} \rightarrow \gamma g$ subprocess becomes dominant. Gluon-gluon initiated processes are not expected to play a significant role over the p_T range shown.

One of the classic applications of direct photon production is to provide constraints on the gluon distribution in global fits of parton distributions. The gluon distribution is especially uncertain in the region beyond $x \approx 0.15$ [18]. Run I results on high- p_T jet production from the CDF [71] and DØ [72] collaborations favor a gluon distribution which is larger at high- x than was anticipated from global fits which did not emphasize the high- p_T jet data. One such example is the CTEQ5HJ [64] set of distributions which are favored by both sets of jet data. One might hope that the direct photon data could shed some light on this issue, but such is not expected to be the case. As shown in Fig. 40, the ratio of the CTEQ5HJ and CTEQ5M predictions is consistent with unity within about 5% over the p_T range under consideration. This can be understood by referring back to Fig. 38 where it is shown that the gq subprocess decreases in importance precisely where one would like to gain a constraint on

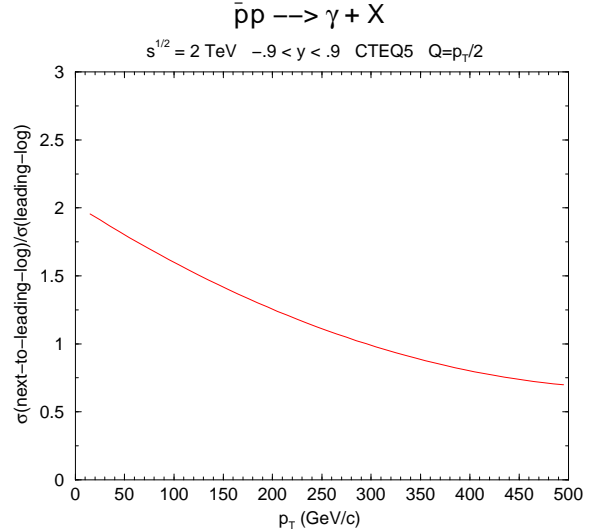


Figure 39. NLO/LO ratio for direct photon production.

the gluon distribution.

2.2.4. New Measurements

As noted in the introduction, the process of direct photon production is of interest for a variety of reasons. In particular, it offers a probe of hard scattering dynamics which complements that of jet production. At this point, the comparison between theory and experiment has not reached the quantitative level that one would like, so there is clearly more to be done. Furthermore, direct photon production has the potential to provide constraints on the parton distribution functions, particularly that of the gluon. Nevertheless, the less than satisfactory description of the current data has meant that this role is, as yet, unfulfilled. Finally, one must understand conventional sources of energetic photons before being able to confidently use photons as part of the signal for new physics. With these points in mind, it is natural to ask whether there are additional observables which could help shed light on some of the theoretical problems.

To date, almost all of the experimental results for direct photon production have been for the transverse momentum distribution of the photon, *i.e.*, the single photon inclusive cross section. Clearly, there is additional information to be gained by studying the joint rapidity distributions of the photon and a jet, *e.g.*, $d\sigma/dp_T dy_\gamma dy_{jet}$ where p_T represents the transverse momentum of the photon. This observable has been measured by the CDF Collaboration [73] for photons in the central region with $16 \text{ GeV} < p_T < 40 \text{ GeV}$.

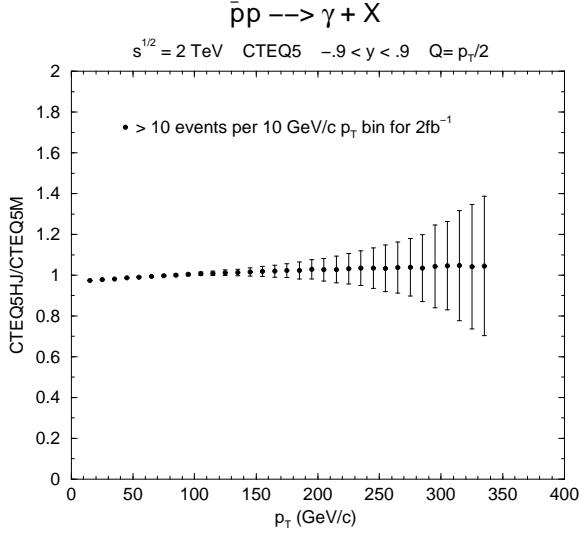


Figure 40. Ratio of the direct photon cross sections calculated with CTEQ5HJ and CTEQ5M with errors based on an integrated luminosity of 2 fb^{-1} .

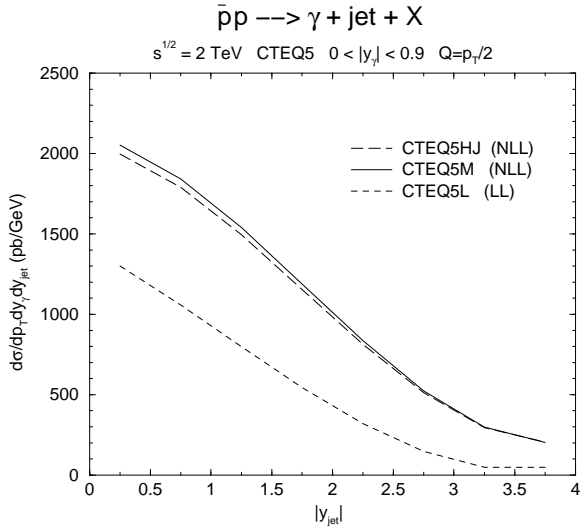


Figure 41. Jet rapidity distribution for photons in the central rapidity region calculated with the CTEQ5L, CTEQ5M, and CTEQ5HJ parton distributions with the program of Ref. [70].

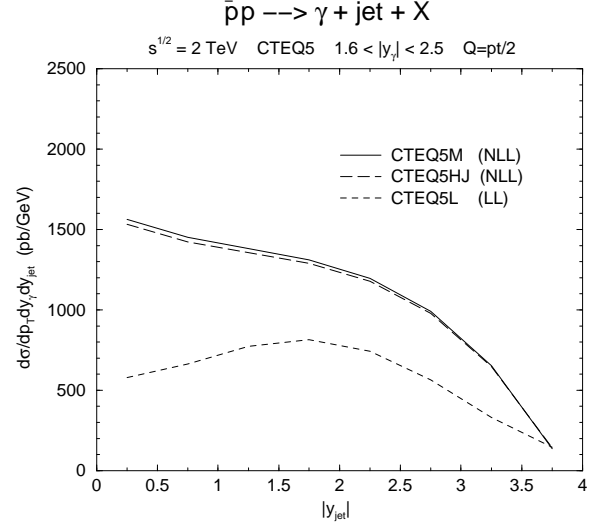


Figure 42. Jet rapidity distribution for photon in a forward rapidity region calculated with the CTEQ5L, CTEQ5M, and CTEQ5HJ parton distributions with the program of Ref. [70].

In this case the theoretical description of the jet rapidity distribution is good. However, no information is yet available for other values of photon rapidity. Some leading-log and next-to-leading-log predictions for this distribution are shown in Fig. 41 for central photons and Fig. 42 for forward photons. Notice the characteristic broadening of the jet rapidity distribution as the photon is moved forward. Note, too, the change in the ratio between the leading-log and next-to-leading-log predictions as the photon rapidity is varied. Predictions are shown for both the CTEQ5M and CTEQ5HJ parton distributions. There is only a slight difference between the two sets, due primarily to the fact that the curves were generated for $p_T > 10 \text{ GeV}$. The resulting low values of x_T result in the parton distributions being probed in a region where there is little difference between the CTEQ5M and CTEQ5HJ sets. On the other hand, that means that for these distributions there will be relatively less uncertainty due to the parton distributions and that, therefore, such measurements may be useful in helping to understand the p_T region where there is a discrepancy between the existing collider data and the theoretical results. In this regard the $D\bar{O}$ results for the inclusive photon yield shown in Fig. 24 are interesting as they may indicate that the theory/data discrepancy has some rapidity dependence. The lesson here is that photon-jet joint observables would be helpful in sorting out the source

of the disagreement between theory and experiment. Note that if one wanted to increase the sensitivity to differences between parton distributions, then a larger minimum p_T cut could be employed.

As discussed in Sec. 2.2.2, there is some indication that the photon yield above a transverse momentum of about 30 GeV may actually be less than the theoretical predictions, in contrast to the situation at lower values of p_T . It was mentioned that this may be related to the observed behavior of the γ/π^0 ratio. This issue is complicated by the necessity of placing isolation cuts on the electromagnetic triggers in order to reduce the π^0 background. NLO Monte Carlo programs can simulate the effect of these isolation cuts, but the experimental dependence on the parameters of the cuts has not yet been compared to that of the theory. If the theoretical treatment of the isolation cuts is wrong, then the comparison of the NLO results to collider data must be considered suspect. In recent years the question of the theoretical treatment of such isolation cuts has been studied by several authors [74, 75, 76]. What is needed is a data set showing how the cross section depends on the cone size and the energy threshold utilized in the isolation cuts. Similar comparisons for jet production have helped refine the various jet algorithms and have been very useful in understanding issues related to the theoretical description of jets.

2.2.5. Conclusions

Run II offers many opportunities to refine our understanding of the production of photons in hard scattering processes. The kinematic reach in transverse momentum should be greatly extended and the statistical precision of the data will also be increased. While there are still problems with the theoretical description of the existing data, the Run II data have the potential to shed some light on these issues. In particular, data for photon-jet correlations and for the dependence of the cross section on the parameters of the photon isolation cuts will be helpful. A better theoretical understanding of direct photon production will enable this process to be better used in the study of large transverse momentum processes and the search for new physics.

3. Topics in Weak Boson Production[†]

The very large number of W and Z boson events CDF and DØ will collect will yield precision measurements of the W mass and width [1], which are fundamental parameters of the Standard Model and thus need to be determined with the highest possible accuracy. The Run II vector boson datasets will of

[†]Contributed by: D. Casey, T. Dorigo, M. Kelly, S. Leone, W.K. Sakumoto, and G. Steinbrück

course provide other important advances in the field of electroweak physics, and will be the starting point of most new physics searches; but they will also become standard tools for the understanding of many sources of systematic uncertainty in otherwise unrelated physics studies. In this Section we will give an overview of some of the additional studies it will be possible to carry out with vector bosons in Run II; for rare decays of W bosons and other topics not covered here see Ref. [77].

3.1. The W Cross Section as a Luminosity Monitor

At both DØ and CDF, the uncertainty on the total integrated luminosity is approximately 4.5% [78, 79]. Though measuring the luminosity is difficult to do well, any measurement at the collider that has an absolute normalization depends on it. In several important cross section measurements made during Run I, this uncertainty contributed greatly to the overall measurement uncertainty. In particular, for both of the W and Z boson cases, the uncertainty in the luminosity measurement far outweighed the other systematic uncertainties in the measurement (see Table 1).

There is also a continuing controversy regarding the actual value of the luminosity at the two detectors at the Tevatron [78, 79]. At both DØ and CDF, the integrated luminosity is normalized by the total inelastic cross section in $\bar{p}p$ collisions. CDF has made this measurement [80] and uses it to normalize their luminosity. DØ did not measure the total inelastic cross section, and chooses to normalize to the world average, which is $\sim 6.2\%$ higher than the CDF measurement [78]. This is primarily due to a 2.8 standard deviation disagreement between the CDF measurement and the E811/E710 measurements [81, 82, 83, 84].

In the context of Run II, there are some general concerns regarding the measurement of the total integrated luminosity, particularly at high instantaneous luminosity. New luminosity monitors are being installed at each detectors as part of the modifications for Run II and CDF plans to repeat the measurement of the total inelastic cross section. However, it is not clear that this will result in a more precise determination of \mathcal{L} , and disagreement regarding the measured $\bar{p}p$ cross section is likely to persist. Given the high precision of the current W and Z cross section measurements, increasing precision in the matrix element calculations (now at NNLO [85]), and the expected abundance of W and Z bosons produced during Run II ($\sim 10^6$ W bosons and $\sim 10^5$ Z bosons within the fiducial volumes of each detector), we may consider using the rate of W boson production to normalize the integrated luminosity. In this subsection, we present a brief overview

Table 1

Measurements of $\sigma(W)$ at the Tevatron. The three quoted uncertainties are statistical, systematic, and luminosity.

Detector	Channel	$\sigma(W) \cdot B$ (nb)
DØ(1A)	$W \rightarrow e\nu$	$2.28 \pm 0.02 \pm 0.08 \pm 0.10$
DØ(1A)	$W \rightarrow \mu\nu$	$2.02 \pm 0.06 \pm 0.22 \pm 0.09$
DØ(1B)	$W \rightarrow e\nu$	$2.31 \pm 0.01 \pm 0.05 \pm 0.10$
DØ(1B)	$W \rightarrow \tau\nu$	$2.22 \pm 0.09 \pm 0.10 \pm 0.10$
CDF(1A)	$W \rightarrow e\nu$	$2.49 \pm 0.02 \pm 0.08 \pm 0.09$

of the magnitude of the experimental uncertainties in the integrated luminosity using W boson production, and discuss the requirements for such a measurement to be competitive with standard luminosity measurements and in what context it would surpass the current precision.

3.1.1. $\sigma(W)/\mathcal{L}$ in Run I/II at DØ

As an example, we describe some details of how the Run I measurement of the cross section for W boson production at DØ would translate into a determination of the total integrated luminosity.

Reversing the relationship between the integrated luminosity (\mathcal{L}) and the production cross section ($\sigma(W)$) in the calculation done by DØ [78], we have the following relation:

$$\mathcal{L} = \frac{N_{cand}(1 - f_{QCD}) - N_Z}{\epsilon A(1 + \frac{A_\tau}{A})\sigma(W)} \quad (2)$$

where N_{cand} is the number of W boson candidates observed, f_{QCD} is the fraction of candidates expected from QCD multi-jet production, N_Z is the number of candidates that are Z bosons in which one of the electrons was unobserved, ϵ is the event identification efficiency, A is the geometric and fiducial acceptance, A_τ is the acceptance times branching ratio for $W \rightarrow \tau\nu$, and $\sigma(W)$ is the predicted cross section times branching ratio for producing W bosons.

Table 2 show the values of each of the quantities as measured in Run I, and the fractional uncertainty each would contribute to a measurement of \mathcal{L} . The total uncertainty from measured quantities alone is 2.2%. Including a 4% uncertainty in the prediction of $\sigma(W)$ increases the total uncertainty to 4.6%.

We note two things: 1) even the Run I measurement results in an uncertainty on \mathcal{L} that is competitive with the directly measured result[‡] and 2) by far, the dominant uncertainty is in the prediction of $\sigma(W)$.

[‡]Of course, we cannot reliably use the theory prediction without the experimental confirmation from Run I!

Table 2

Uncertainties on the components of the measurement of \mathcal{L} if one used the components of the Run I measurement of the W production cross section by DØ.

Component	Value	Error on \mathcal{L}
f_{QCD}	0.064 ± 0.014	1.5%
ϵ	0.671 ± 0.009	1.3%
A	0.465 ± 0.004	0.9%
N_{cand}	67078	0.4%
N_Z	621 ± 155	0.3%
A_τ/A	0.0211 ± 0.0021	0.2%
$\sigma(W)$	22.2 ± 0.9 nb	4%

In preparation for Run II, both DØ and CDF are undergoing major upgrades to the detectors. For DØ, this includes the addition of a solenoid magnet and a complete replacement of the tracking system. The total luminosity is expected to increase by a factor of ~ 10 . We now consider how each of the factors in Eq. 2 will be affected in Run II.

The background fraction for events from QCD multi-jet production is dominated by systematics for the detection of electrons. We do not expect the uncertainty to decrease dramatically, nor do we expect the overall background level to change much. It may be possible to reduce the backgrounds and make them easier to understand if we use the muon channel; however, no serious study has been made on the subject.

The uncertainty on the lepton identification efficiency is equal parts Z boson statistics and background subtraction statistics and will scale by $\sim 1/\sqrt{10}$ (we assume an integrated cross section of 1 fb^{-1} in this section). We expect the tracking efficiency to increase, but the efficiency of the isolation and \cancel{E}_T requirements may decrease due to multiple interactions and decreased resolution due to the presence of the solenoid in the Run II detector. Speculating, these effect may balance each other, leaving an overall reduction in the uncertainty by 1/3 to 0.9%.

The geometrical and fiducial acceptance will stay approximately the same. The uncertainty is dominated by the electromagnetic energy scale (0.00319 of 0.004) whose uncertainty will be smaller in Run II due to an increased number of Z boson events and extra handles provided by a central magnetic field in the DØ detector. Scaling the rest of the uncertainties with the luminosity, we should be able to halve the uncertainty on the acceptance to 0.5%.

The uncertainties in the expected number of Z candidates and the acceptance of electrons and muons

Table 3

Estimated values for the uncertainties in a measurement of \mathcal{L} in Run II.

Component	Error on \mathcal{L}
f_{QCD}	1.5%
ϵ	0.9%
A	0.5%
N_{cand}	0.08%
N_Z	0.0%
A_τ/A	0.0%
$\sigma(W)$	4%

from $W \rightarrow \tau\nu$ are dominated by MC statistics and can be shrunk to a negligible value.

Finally, the number of candidates will increase by a factor of 10 just from the increased luminosity, by approximately a factor 1.12 from the increase of the center of mass energy from 1.8 TeV to 2.0 TeV, and by another factor of ~ 2 if one includes the muon channel, resulting in about 1.4×10^6 candidates, which translates into a statistical uncertainty of about 0.08%.

Table 3 summarizes the expected experimental uncertainties for measuring \mathcal{L} in Run II at $D\phi$. A measurement of the luminosity will be dominated by the background level and uncertainty and by the uncertainty in the prediction of the cross section. Figure 43 shows how changes in the QCD background level and uncertainty, and uncertainty in the cross section prediction, affect the overall uncertainty in the resulting luminosity. In each case, all quantities from experiment were fixed to their Run I values except the one being varied. The uncertainty on the cross section was made negligible when considering the sensitivity to the background level and uncertainty. We note that decreasing the fractional uncertainty on the QCD multi-jet background by a factor of 2 – 4 reduces the luminosity uncertainty from 2.2% to 1.7 – 1.8% – a factor of 0.3 – 0.2. The relatively large uncertainty in the background level (20%) translates into a significant sensitivity to the background level itself. Essentially, the trade-off for loosening the selection criteria and allowing more background into the data sample is that the background must be measured much more precisely in order to maintain a small uncertainty. In Run II (as in Run I), the best strategy to minimize the effect of the background uncertainty on the total cross section measurement will be to minimize the level of the background altogether – if the background can be made negligible, the effect of the uncertainty of the background on the cross section (no matter how large) will also be negligible. The cross section uncertainty

continues to dominate the situation. However, if the cross section uncertainty is kept to approximately the size of the experimental uncertainty, the resulting luminosity uncertainty is more than a factor of two better than the Run I value.

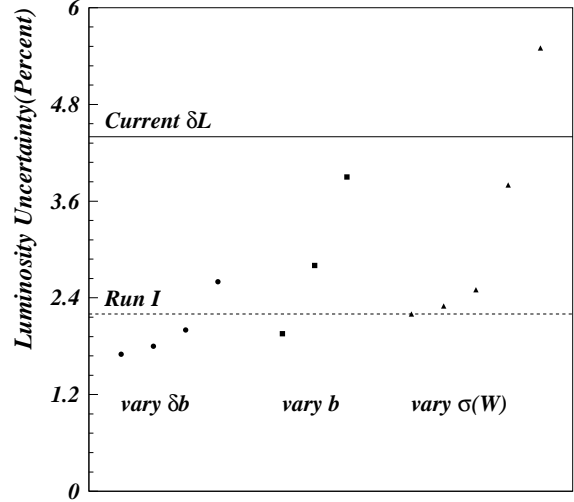


Figure 43. Impact of changing the overall background level (b), the uncertainty on the background level (δb), and the predicted $\sigma(W)$ in determining \mathcal{L} . Except when being varied, the experimental values are kept to the Run I determinations. Except when varying the uncertainty on the cross section, $\delta\sigma(W)$ is set to 0. The circles denote $\frac{\delta b}{b} = 0.05, 0.10, 0.15, 0.25$. The squares denote background fractions, $b = 5, 10, 15\%$. The triangles denote $\frac{\delta\sigma(W)}{\sigma(W)} = 0.001, 0.005, 0.01, 0.03, 0.05$. The solid line shows the current values of the luminosity uncertainty at $D\phi$ and the dashed line shows the uncertainty if the rate of W boson production was used and $\sigma(W)$ was known perfectly.

3.1.2. Counting on the Prediction for $\sigma(W)$

If one determines the integrated luminosity using the rate for W boson production, there are two fundamental issues that must be resolved. First, one must decide that the calculation for $\sigma(W)$ is reliable in itself; that it agrees with experiment. Second, one must determine the uncertainty in the calculation, since it will likely dominate the uncertainty in \mathcal{L} .

The first issue is likely not problematic. If all cross

section measurements were normalized to a specific $\sigma(W)$ calculation, then the worst impact of a change in that calculation would be to modify all measurements in the same manner. Additionally, the advantage would be that all measurements would be easy to compare, since the controversy over the measurement of the total inelastic cross section of $\bar{p}p$ collisions would be circumvented.

The problem of determining the uncertainty on the calculation is more difficult. Various *ad hoc* methods have estimated the uncertainty on $\sigma(W)$ to be 3–5% [78]. The uncertainty in the cross section is dominated (almost exclusively) by uncertainties in the PDF's which go into the calculation. (The uncertainties due to higher order QCD and electroweak corrections are likely much smaller than these.) Two efforts to understand the uncertainties in the PDF's quantitatively are described in the report of the Working Group on Parton Distribution Functions [2].

3.1.3. Conclusion

We have described the current expectations for measuring the integrated luminosity in Run II using the rate for W boson production. The experimental uncertainties, totaling $\sim 2.2\%$, are dominated by the uncertainty in the background from QCD multi-jet interactions. However, the total uncertainty is dominated by an ill-defined uncertainty on the prediction for the production cross section for W bosons. With sufficient progress in the continuing effort to quantify this uncertainty, we may be able to reliably determine the total integrated luminosity in Run II using the rate for W boson production to $\sim 3 - 4\%$.

3.2. Determination of the Weak Boson p_T Production Spectrum

During Run II at the Tevatron, CDF and $D\bar{O}$ will obtain the largest data set of e^+e^- pairs resulting from via $p\bar{p} \rightarrow \gamma^*/Z$ to date, pushing the analysis of vector boson production characteristics over the edge from being limited by statistical uncertainties, to being limited by systematic uncertainties. The di-electron final state provides two important experimental handles. Electrons themselves are among the best-measured objects at either detector, with far better resolution in energy and position than most final-state high- p_T objects (such as jets or muons). Additionally, the di-electron final state provides complete kinematic information about the hard collision; the four-momentum of the Z/γ^* state is known unambiguously. Since the electroweak character of the decay to di-electrons is generally uncorrelated with the QCD characteristics of the production of the vector boson state, di-electron production in $p\bar{p}$ collisions via the Drell-Yan production is a sensitive probe for investigating many aspects of

QCD. The rapidity (y) distribution is the Drell-Yan analog to deep inelastic scattering structure function, providing additional constraints on PDF's. The transverse momentum (p_T) distribution is sensitive to predictions from standard perturbative QCD at high- p_T ($\sim Q^2$) and to predictions from soft-gluon resummation calculations at low- p_T [86, 87]. Additionally, the low- p_T region is sensitive to non-perturbative effects not calculable in pQCD. These effects are included via a universal form factor, not unlike PDF's, whose parameters must be tuned to data.

In addition to the intrinsic benefits of precision measurements of QCD, there are practical benefits for other measurements at the Tevatron. In the low- p_T region, where the cross section is highest, uncertainties in the phenomenology of vector boson production have contributed to the uncertainty in the measurement of the mass of the W boson (M_W) [88, 89]. Diboson, top quark, and Higgs boson production all have single and di-electron backgrounds from W and Z boson production that will be more constrained through a precise measurement of Z/γ^* production properties. Also, the universality of the resummation approach requires further experimental testing, with implications ranging from the impact on the precise determination of M_W , to the production of Higgs bosons and di-photons [90, 10].

High mass Drell-Yan e^+e^- pairs are experimentally distinctive: the electrons typically have large E_T 's, are separated from each other in η and ϕ , and tend to be separated from jets and other activity in an event. In Run I, CDF and $D\bar{O}$ collected such events with electrons in the central ($|\eta_{\text{det}}| < 1.1$) and forward ($1.1 < |\eta_{\text{det}}| < 2.4/2.5$) regions, providing a coverage in the e^+e^- -pair rapidity of up to $|y| \sim 3$. Since the online and off-line electron identification efficiencies are comparable (for both experiments), additional off-line requirements primarily enhance the rejection of background from QCD multijet events that were mis-measured as electrons. At CDF, the most powerful discrimination is provided by tracking and precise electron shower centroid measurements. To cope with the large jet backgrounds in the forward detector region, CDF developed the SVX-Plug tracker [91] and improved the matching of tracks in the vertex tracker with calorimeter shower positions during Run I. Applying such forward tracking techniques to both e 's of a pair reduced the backgrounds from about 10% to a percent or less. At $D\bar{O}$, the most background rejection was obtained by additional isolation and shower-shape requirements, reducing the backgrounds from $\sim 10-15\%$ to 4–7%, depending upon fiducial region. With the addition of central magnetic field and enhanced tracking in the Run II detector, the background is expected

to be reduced even further.

To allow direct comparisons of experimental results with QCD predictions, the experimental results are fully corrected for detector acceptance, experimental efficiencies, and detector resolution effects. For the Run I data, CDF and DØ used Monte Carlo simulations to determine the corrections for the detector efficiency, acceptance, and resolution as a function of p_T and y . CDF generated the di-electron signal using PYTHIA [92], processing them with the CDF detector simulation and reconstruction programs. Additionally, they used PHOTOS [93] to simulate final state QED radiation from the $\gamma^*/Z \rightarrow e^+e^-$ vertex. PYTHIA and the detector simulation were tuned to obtain satisfactory agreement with data [94]. DØ generated γ^*/Z events using the resummed prediction from LEGACY [95], smearing the decay electrons with a parameterized detector simulation which included final-state QED radiation corrections. The parameters and resolutions in the detector simulation were tuned to obtain agreement with data [96].

In general, the predictions for vector boson production do not yet include QED effects, therefore the experimental corrections must attempt to account for them. At a minimum, final state QED radiation must be included because the effects are large [97], and CDF and DØ included such corrections in their Run I measurements. As there is yet no numerical implementation of the QED corrections analogous to the QCD soft gluon resummation formalism, initial state QED effects have not been considered. Initial state QED radiation effects in p_T are expected to be similar to those in QCD, but since the coupling is much smaller, the p_T distribution due to QED effects should be much softer. It is expected that resummation of the initial state soft-photon emission can be implemented similarly to the soft gluon case [97].

Using $110 \text{ pb}^{-1} e^+e^-$ data from Run I, both CDF and DØ have measured the Drell-Yan cross section $d\sigma/dp_T$ [94, 96] and CDF has measured $d\sigma/dy$ [98, 99]. For both CDF and DØ, the measurement error at the peak of the p_T distribution ($\sim 3 \text{ GeV}/c$) was $\sim 6\%$. The measurement error at $|y| = 0$ was $\sim 5\%$. The combined efficiency and acceptance for these measurements was $\sim 33\%$.

The dominant systematic uncertainties in these measurements are the efficiency and background corrections. Generally, the uncertainty in shape is more problematic than the uncertainty in overall normalization. As mentioned, the level of background is expected to be reduced in Run II with the enhanced tracking available in both detectors. This will also reduce the effect of the normalization-uncertainty on the final measurement. The uncertainty in the shape of

the background is dominated by statistics from events that satisfy multijet and direct- γ triggers, which also satisfy the kinematic and fiducial requirements necessary for the Z/γ^* analysis. Again, the enhanced statistics of Run II should allow this uncertainty to be reduced. The overall electron identification efficiency is well-known in both experiments— $\delta\epsilon \sim 0.5\%$. The shape as a function of p_T is dominated by the isolation requirement being spoiled by jet activity nearby the electron cluster. Understanding this effect requires either excellent GEANT-type Monte Carlo or a great number of di-electron events from single-electron triggers, so one can investigate the effects of hadronic activity on electron isolation in an unbiased manner. We expect to see improvements in both areas in Run II, hopefully reducing the uncertainty in the shape of the efficiency as a function of p_T from $\sim 3 - 5\%$ to $\sim 1\%$.

The expected Run II measurement errors for the $d\sigma/dy$ and $d\sigma/dp_T$ measurement can be estimated from the Run I measurement errors by assuming that the statistical (“Stat”) and systematic (“Syst”) errors scale as follows:

$$\begin{aligned} \text{Stat} &\rightarrow 1/\sqrt[2]{N_{\text{ev}}} \\ \text{Syst} &\rightarrow 1/\sqrt[4]{N_{\text{ev}}} \end{aligned}$$

where N_{ev} is the number of events in a bin. The scaling of the systematic uncertainties should be considered a rough parameterization. Scaling the Run I uncertainties from CDF to an integrated luminosity of 2 fb^{-1} , we obtain predictions for the total measurement uncertainty in $d\sigma/dy$ (Fig. 44) and $d\sigma/dp_T$ (Fig. 45).

With an expected precision of a few percent, the Run II data can provide even more stringent constraints on all aspects of our understanding of Z/γ^* productions, with important implications on our understanding of resummation in pQCD, and the precision determination of M_W . The precision of the Run II $d\sigma/dy$ and $d\sigma/dp_T$ measurements will most likely be limited by systematic uncertainties from corrections to the detector acceptance/efficiency and resolution. These uncertainties will be constrained through the improved accuracy of Monte Carlo detector simulations, and the additional data available in general during Run II.

3.3. Offstream Searches for Vector Bosons

3.3.1. Introduction

Since their discovery in 1983 [100, 101, 102, 103], W and Z bosons have been studied at hadronic colliders only via their leptonic decays. As a matter of fact the hadronic decays of these particles are generally so difficult to separate from the huge QCD backgrounds that, after the extraction of a nice mass bump in the jet-jet mass distribution by the UA2 collaboration in

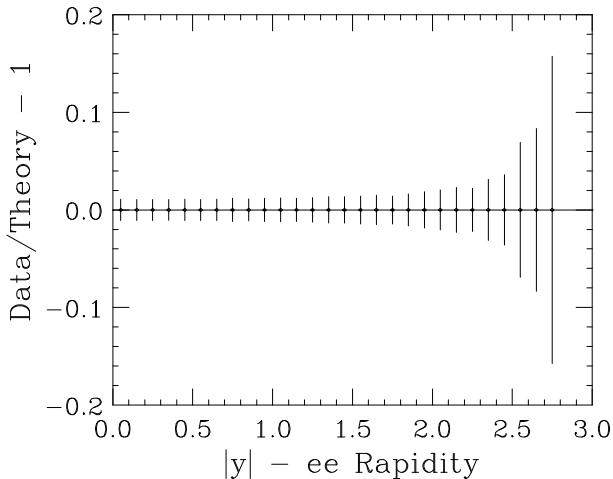


Figure 44. The expected CDF Run II measurement error on $d\sigma/dy$ of e^+e^- pairs in the mass range 66 – 116 GeV/c^2 . “Data/Theory” has been arbitrarily set to unity. The error is for 2 fb^{-1} .

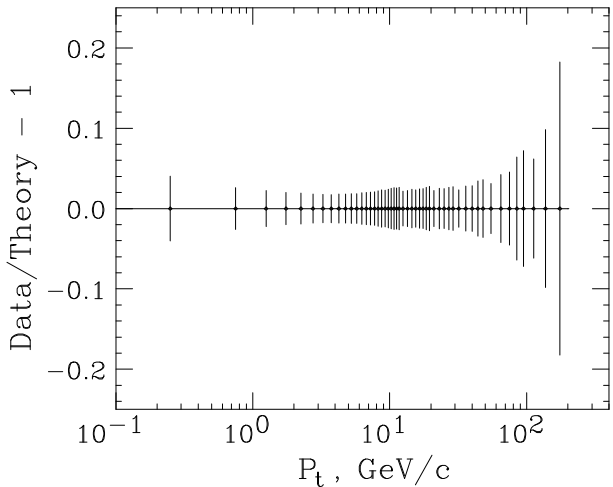


Figure 45. The expected CDF Run II measurement error on $d\sigma/dp_T$ of e^+e^- pairs in the mass range 66 – 116 GeV/c^2 . “Data/Theory” has been arbitrarily set to unity. The error is for 2 fb^{-1} .

1987 [104, 105], they have laid dormant for quite a while as an electroweak physics topic.

Things have started to change with the increase of collider luminosity and dataset size. During Tevatron’s Run I, hadronic W decays have been successfully used by CDF and D0 in the discovery and measurement of the top quark properties both in the single lepton and fully hadronic final states, and a handful of jet-jet masses peaking at 80 GeV have been extracted from a subset of high-purity $t\bar{t}$ events (see Fig. 46). More recently, a signal of Z decays to b -quark pairs has emerged in the CDF data (Sec. 3.3.3).

With Run II sample sizes it will be possible to search for more such hadronic signals, and some of them are expected to start becoming useful tools for other physics advances. In fact, their potential as calibration tools for the jet energy measurement is high, provided that they can be collected by unbiased triggers. This seems particularly likely in the case of $Z \rightarrow b\bar{b}$ decays, where the background has been shown to be reducible to a manageable size and the hardware tools for collecting them with good efficiency and small bandwidth concessions are now available; moreover, for b -quark jets the absolute energy scale cannot be fixed by photon-jet balancing techniques, due to the rarity of events with a photon recoiling against a single b -quark jet: a Z peak may then really be our best chance for that purpose. Hadronic W decays will also be an ideal calibration tool in $t\bar{t}$ events, but efforts need to be spent on finding their signal in independent data samples. These may be provided by diboson production processes, where triggering and background issues are less problematic.

3.3.2. Hadronic Decays of W Bosons

Searches for a W mass signal in inclusive jet triggers have been fruitless in Run I data. With respect to the lower energy $S\bar{p}pS$ collider, the Tevatron’s higher center-of-mass energy is a disadvantage for once, because in the face of a four-fold increase in signal cross section the background from QCD processes increases by an order of magnitude, due to its steep behavior with respect to parton x . Moreover, no dedicated low- E_T jet triggers were devised either at CDF or D0 during Run I, given the experiments’ focus on the high energy frontier; at the very end of the run, however, a sector of CDF’s central tracking chamber became in-operative due to a broken wire, which allowed 1.9 pb^{-1} of data to be collected by a high-bandwidth 12 GeV dijet trigger. The data thus gathered did not allow the extraction of a W peak either, but lends itself to fruitful extrapolations to Run II.

It seems reasonable to investigate the collection of events with very low jet E_T by special low-luminosity

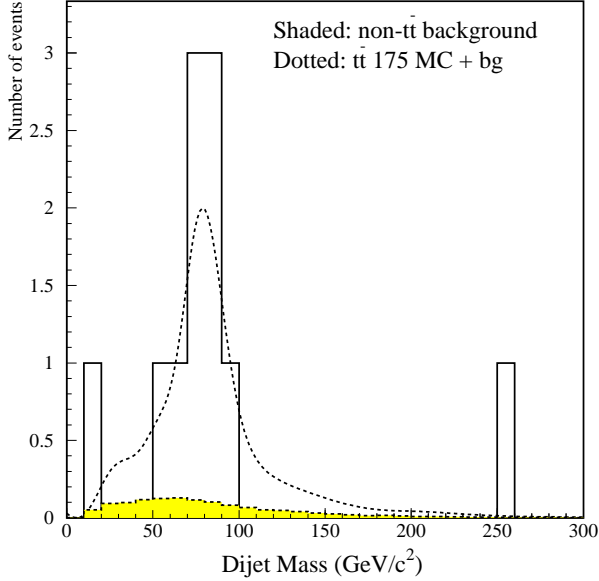


Figure 46. The jet-jet mass distribution of untagged jets in the very high purity single lepton $t\bar{t}$ candidates sample collected by CDF requiring two additional b -tagged jets.

runs, which might become an attractive option in the event of temporary inoperativeness of tracking detectors. Here we examine a scenario where CDF II or DØ gathers some 100 pb^{-1} of unprescaled data collected with a trigger requiring two calorimeter towers above 4 GeV at Level 1 and two jets with $E_T > 10 \text{ GeV}$ at Level 2, back-to-back in ϕ —about the smallest thresholds that do not saturate the bandwidth. About two million $W/Z \rightarrow jj$ decays could be then collected, which would be reduced to 200,000 after optimized kinematic cuts requiring two central back-to-back jets and little extra-jet activity. Toy Monte Carlo studies suggest that in such a scenario the W mass could be fit with a $\sim 0.5 \text{ GeV}$ uncertainty, provided the availability of a prescaled sample with looser requirements at Level 2: this would yield an understanding of the absolute jet energy scale of the detectors to better than 1%. Such a dataset could then clearly be used also for excellent tests of optimization of jet algorithms, and thus offer benefits to any search for hadronically decaying massive objects.

3.3.3. Z Decays to b -Quark Pairs in Run I

Thanks to the several million Z decays to b -quark pairs collected by the LEP I and SLD experiments since 1992, the physics of these decays is extremely

well studied and understood. At a proton-antiproton collider that particular process had not been identified before, though; therefore the extraction of a signal in Run I data was interesting in its own right. Moreover, the knowledge of how to extract a Z peak enables a careful design of a dedicated trigger for Run II, which may allow us to collect a large sample of these events, from which the mass distribution can be fit and thus insight can be obtained on the absolute energy scale for b -quark jets, substantially reducing one of the critical sources of systematic uncertainty in the top quark mass measurement.

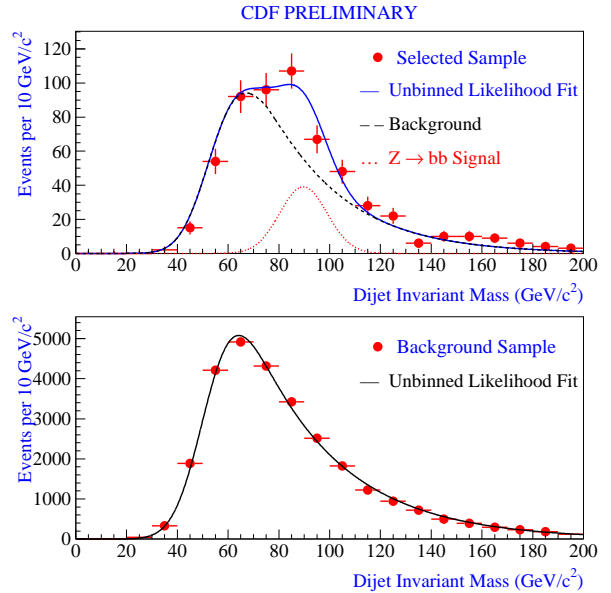


Figure 47. Top: the $Z \rightarrow b\bar{b}$ peak in the signal sample; bottom: a signal-depleted sample is used to extract the background shape.

A $Z \rightarrow b\bar{b}$ signal was extracted in Run I CDF data using kinematic tools and b -quark vertex tagging. Starting from a dataset of about five million events enriched of b -quark decays collected by a single muon trigger, a very tight kinematic selection was devised, which increased the signal to background ratio by three orders of magnitude.

The main background to the Z decay to b quarks is due to direct QCD production of a $b\bar{b}$ pair, while non- b backgrounds yielding muons can be completely eliminated by requiring the presence of a secondary vertex in each of the two jets; this cut also reduces the flavor excitation and gluon splitting contributions to b quarks

in the sample quite effectively. Most of the direct $b\bar{b}$ pairs are produced at the Tevatron by a gluon fusion process, whose high color charge in the initial state and color flow topology are distinctive characteristics. To exploit the smaller probability of QCD radiation in the signal, the two leading jets were required to be back-to-back in ϕ , and the sum of all other calorimeter clusters in the event was required to be smaller than 10 GeV. These cuts selected 588 events, whose jet-jet mass distribution was fit to the sum of QCD background and Z decay to yield a signal of 91 ± 30 events, with a S/N ratio at the Z peak equal to 1/3; the fit resulted in a Z mass of 90.0 ± 2.4 GeV (see Fig. 47). If the same analysis should be replicated with 20 times more statistics and no detector improvements, this would yield a relative error in the b -jet energy scale smaller than 1%. The picture could be even rosier as far as statistics goes, due to the extended lepton coverage and improved silicon tracking the Run II detectors will be endowed with, but the strong bias due to the triggering lepton will make these findings of difficult use for generic b -quark jets.

Besides its possible use as a calibration tool, however, a $Z \rightarrow b\bar{b}$ peak provides a fine testing ground for algorithms designed to improve the jet energy measurement for b jets, which is one of the critical points for the discovery of an intermediate mass Higgs boson in Run II. The $b\bar{b}$ final state is the dominant one in Higgs boson decay if $M_H < 135$ GeV/ c^2 [106]. Our ability to extract this particle from the large QCD background in Run II (for instance in the $Wb\bar{b}$ final state, when associated WH production is sought) will therefore depend critically on the resolution we can attain on the Higgs boson mass as reconstructed from the measured b -quark jet energies: both the possibility to see a bump in the mass spectrum of jet pairs associated to a leptonically decaying W bosons, and the alternative option of applying a mass window cut as a selection tool for these events, will strictly depend on the actual mass resolution.

The expected resolution for a generic jet-jet resonance at CDF and D0 was roughly $\sigma_{M_{jj}} = 0.1M_{jj}$ in Run I. A relative improvement of this number by 30% would significantly extend [106] our discovery reach for the Higgs boson in Run II. In order to achieve that improvement we must study in detail the characteristics of b -quark jets emitted in the Higgs decay, and use to their utmost the large amount of available information provided by the various detector components D0 and CDF II are made up of. For example, three-dimensional tracking in the new SVX II detector may allow CDF II to infer the momentum of the escaping neutrinos in semileptonic b -quark decays, greatly improving the energy measurement of the resulting

jets; this plan will work well in Run II, given the larger acceptance for charged leptons from semileptonic decays provided by the new detectors. Furthermore, the possibility of measuring track momenta to higher rapidity will allow a fruitful use of tracking information to improve the calorimetric measurement of jets.

A detailed study of the observable quantities of b -quark jets produced in $Z \rightarrow b\bar{b}$ decays followed by one semileptonic $b \rightarrow \mu X$ decay have been shown to allow a sizable reduction of the width of the reconstructed $b\bar{b}$ peak. The quantities found useful for this purpose in the CDF analysis were the muon momentum, the projection of missing transverse energy along the jet axes, and the charged fraction of the jets.

The muon momentum is needed in the correction of jets containing a semileptonic decay of b quarks, because the minimum ionizing muons do not contribute linearly to the energy measured in the calorimeter. The missing E_T , projected along the jet directions in the transverse plane, provides useful information on the amount of momentum taken away by the neutrino in the muon jet and on possible fluctuations of the energy measurement in both the muon and the away jet. The charged fraction of the jets, defined as the ratio between the total momentum of charged tracks belonging to a jet and the energy measured in the calorimeter, also helps reducing the uncertainty in the energy measurement.

By properly accounting for the value of these observables, it was possible to reduce the relative uncertainty in the dijet mass measurement, σ_M/M_{jj} , by nearly 50% (see Fig. 48).

If the alternative plan (described in the following section) based on collecting $Z \rightarrow b\bar{b}$ decays by triggering directly on secondary vertices in jets at Level 2 should fail, CDF II will anyways be able to observe a peak of several thousand events in the inclusive lepton datasets by simply replicating the Run I analysis. These peaks will not allow a precise calibration tool for inclusive b -quark jets, given the biasing semileptonic decay of one of the two jets, but they will anyways be extremely useful as a testing ground for the algorithms now under development which aim at reducing the jet energy resolution.

3.3.4. Z Decays to b -Quark Pairs in Run II

A strategy to collect $Z \rightarrow b\bar{b}$ events in Run II has been studied having in mind the CDF trigger configuration. We tried to keep the trigger requirements as simple as possible and optimize them in order to have acceptable trigger rates (less than 2% of the total bandwidth at each level) and maintain a good signal efficiency.

Most $Z \rightarrow b\bar{b}$ events should contain two recon-

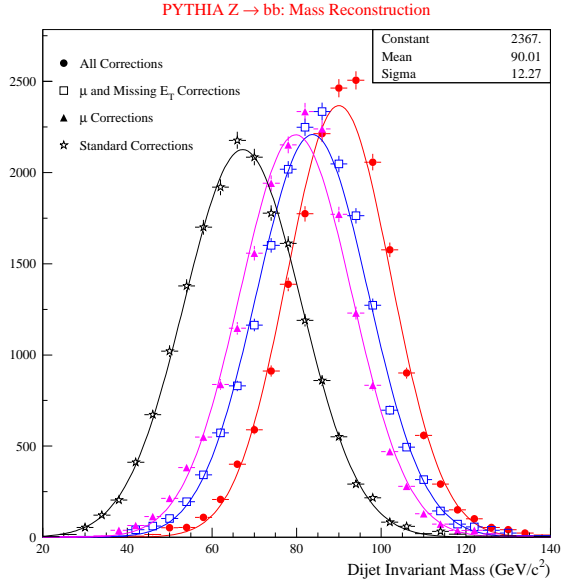


Figure 48. The four Gaussian fits show the improvement of the mass reconstruction for simulated $Z \rightarrow b\bar{b}$ events (Pythia V5.7, CDF detector simulation) when the observable characteristics of the b -quark decays are properly taken into account in the mass reconstruction.

structable secondary vertices in the final state. In Run II it will be possible to trigger on secondary vertex information. Exploiting this feature, it should be possible to collect a sample of $Z \rightarrow b\bar{b}$ events without particular requirements on the b decay. One purpose of this dataset is to provide a sample to calibrate the calorimeter energy scale for jets containing b quarks, which may limit our ability to measure the top mass. Therefore the trigger path should bias the energy scale measurement as little as possible.

At Level 1 the XFT (eXtremely Fast Tracker) information will be available: transverse momentum P_T , azimuthal angle ϕ and charge sign of particles crossing all of the Central Outer Tracker (COT) layers. We require the presence of two central high P_T tracks in opposite hemispheres. Cuts are chosen on the track P_T and $\Delta\phi$ to maximize the statistical significance (S/\sqrt{B}). The track P_T cuts are 6 GeV and 4 GeV, with $\Delta\phi > 150^\circ$.

At Level 2 the rate is reduced by requiring the tracks to have a finite impact parameter. The SVT (Silicon Vertex Tracker) processor will provide this information. The best significance is found by requiring two SVT tracks with $120 \mu m < |d| < 1000 \mu m$.

The computing power of the Level 3 processors should allow the reconstruction of secondary vertices online. We require two jets, each with uncorrected $E_T > 10$ GeV in a cone of radius $R = 0.7$, and check that the jets contain two displaced vertices.

A summary of signal efficiency, trigger cross section and trigger rate at the three trigger levels is reported in Table 4 for a typical instantaneous luminosity $\mathcal{L} = 1.4 \cdot 10^{32} \text{cm}^{-2}\text{s}^{-1}$.

Table 4
Summary of the $Z \rightarrow b\bar{b}$ trigger efficiency, cross section, and rate at each level.

Trigger	ϵ_S (%)	σ_T	R_T (Hz)
Level 1	17.0 ± 0.2	$(5.7 \pm 0.3) \mu b$	800 ± 42
Level 2	3.10 ± 0.03	$(32 \pm 3) nb$	4.4 ± 0.4
Level 3	2.4 ± 0.1	$(3.2 \pm 0.9) nb$	0.5 ± 0.1

Since $\sigma(p\bar{p} \rightarrow Z \rightarrow b\bar{b}X) \simeq 1$ nb, about $2 \cdot 10^6$ $Z \rightarrow b\bar{b}$ events will be produced in Run II, assuming 2fb^{-1} of data collected in two years. We expect to collect 48,000 signal events in a total of about $6.4 \cdot 10^6$ with this trigger, corresponding to a S/B of 0.0075 and a significance $S/\sqrt{B} \simeq 19$.

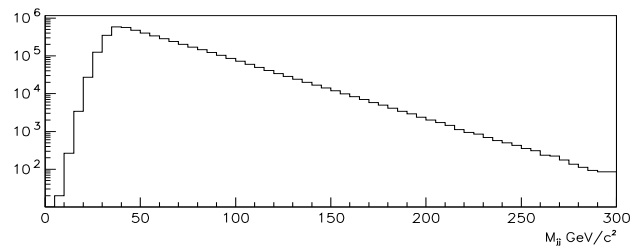


Figure 49. M_{jj} distribution expected from Run II: signal+background.

It is also advantageous to require the presence of no additional jets with $E_T > 10$ GeV in the event, either at trigger level or at a pre-analysis level. This would increase the signal fraction to 0.013 and the significance to $S/\sqrt{B} = 24$. We simulated the signal extraction procedure under these assumptions. We searched for

the $Z \rightarrow b\bar{b}$ signal in the jet-jet invariant mass distribution M_{jj} . We expect to see an enhancement corresponding to the Z mass, since the statistical significance of the signal is high. Outside of the signal region the M_{jj} spectrum should be approximately described by a decreasing exponential.

The PYTHIA Monte Carlo is used to model the $Z \rightarrow b\bar{b}$ invariant mass spectrum. The background M_{jj} distribution expected for the background is inferred from generic Run I dijet data by assuming that the request of secondary vertices does not modify its shape. The M_{jj} distributions for signal and background normalized to 2 fb^{-1} have been added (see Fig. 49).

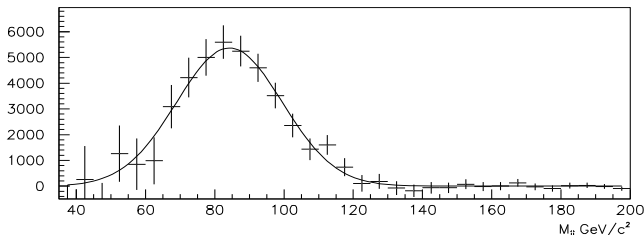


Figure 50. Background-subtracted M_{jj} distribution for Z events obtained from a pseudo-experiment.

Because of the very low S/B ratio, we cannot distinguish by eye the signal peak in Fig. 49. We conducted 1000 pseudo-experiments, varying every time the bin content according to a poissonian distribution with mean equal to the bin content itself. For each pseudo-experiment the region outside the Z peak was fitted with a decreasing exponential. The value of this function was subtracted, bin by bin, from the total spectrum. The results obtained in one of these pseudo-experiment subtractions is shown in Fig. 50, together with a gaussian fit to the excess found. With this method we typically obtain for the jet-jet invariant mass peak position $M_{meas} = 84.0 \text{ GeV}/c^2$, with a statistical uncertainty of $1.5 \text{ GeV}/c^2$ on M_{meas} .[§]

The interval of $\pm 2\sigma$ around the Z peak ($55 \text{ GeV}/c^2 < M_{jj} < 115 \text{ GeV}/c^2$) contains about 93% of the signal events and 25% of the background

[§]The jet energy corrections applied here are not optimized for b jets, whose higher mass and decay properties are sensibly different from those of generic light-quark and gluon jets: the invariant mass peak is thus about 7 GeV lower than the true Z mass.

events. Therefore in this region $S/B = 0.05$ and the statistical significance is $S/\sqrt{B} = 44$.

The error on the Z mass can be directly translated into an error on the b -jet energy scale. Measuring the Z mass with an error of the order of $1.5 \text{ GeV}/c^2$ will allow to determine the b -jet absolute energy scale with an uncertainty of 1.7%.

3.3.5. Other Hadronic Signals

Besides its interest for the study of trilinear gauge boson couplings, discussed in Sec. 4, associated production of two vector bosons yielding a leptonic and a hadronic decay may provide additional handles for the physics of hadronic resonances, both because of the ease of collecting these events with good efficiency in high- P_T lepton triggers and because of the larger signal to background ratio with respect to single boson production processes, due mainly to the reduction of background processes with gluons in the initial state.

WW production is the best example: in a sample of 5 fb^{-1} , for instance, about 3000 $p\bar{p} \rightarrow WW \rightarrow l\nu jj$ events can be collected by applying standard cuts on the leptonic decay products and requiring two jets with uncorrected $E_T > 15 \text{ GeV}$; the signal to noise ratio is then close to 1/40 before any optimized selection. Thence an observation of the W peak in the dijet mass distribution will be relatively easy to obtain. Systematic effects in the mass fits due to the low S/N ratio may make this sample of little impact as a source of knowledge of jet energy scale when compared to the high-purity $W \rightarrow jj$ samples that single lepton $t\bar{t}$ decays may provide; but the signal may still be extremely useful for the study of jet resolutions.

Another process that will be likely observed in Run II is associated WZ production with a subsequent leptonic decay of the W boson and a decay of the Z to b -quark jets. In 5 fb^{-1} about 500 such events can be collected by the lepton triggers, from where secondary vertex tagging can considerably increase the signal purity. Despite its small size, this signal may be of fundamental importance in checking systematic uncertainties in the standard model Higgs boson search, which will mainly focus on the very same dataset with very similar analysis cuts.

Finally, the possibility of collecting $Z \rightarrow b\bar{b}$ in photon triggers has been investigated. $Z\gamma$ production has a small cross section –about 2.5 pb for a photon with $E_T > 10 \text{ GeV}$ and two b -quark jets (see Fig. 51)– but the heavy flavor decay provides a quite distinctive signature, and the process could be easily put in evidence if a sufficiently low trigger threshold were set on the photon transverse energy, or alternatively if a γb trigger could be devised. The advantage of the process producing an additional photon over inclusive Z pro-

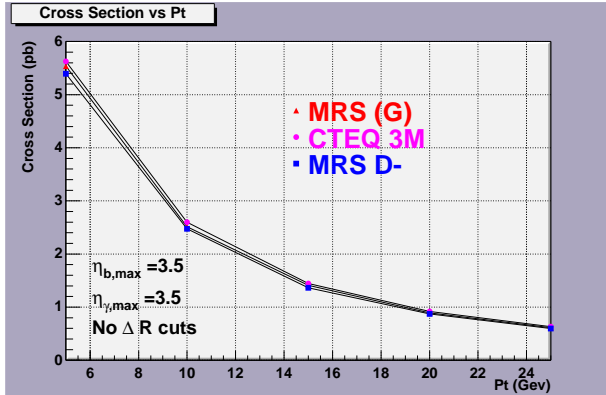


Figure 51. The cross section times branching ratio for $Z\gamma$ production with subsequent $Z \rightarrow b\bar{b}$ decay, for different choices of PDF sets, computed with the Baur-Berger-Zeppenfeld generator [107].

duction lays in the suppression of the irreducible background from direct QCD $b\bar{b}$ production: since initial state photons can only be present in quark-antiquark annihilation diagrams, at Tevatron energies the $b\bar{b}\gamma$ background is suppressed by roughly an order of magnitude more than the Z signal with respect to the searches in inclusive $b\bar{b}$ samples. It is however difficult to devise an unpre-scaled trigger capable of a sufficient efficiency for the signal while maintaining the total rate at an acceptable level. In particular, a γb trigger would have to require at Level 1 both a photon candidate and one or two charged tracks; the tracks and the photon would then need to be separated in azimuthal angle, to reduce the rate of fake photon signals from QCD events. There is currently no plan to devise such a trigger in CDF II or DØ, while the lowest unpre-scaled photon triggers will collect events with $E_T^\gamma > 25$ GeV, where the $\gamma b\bar{b}$ cross section is only 0.6 pb. With 5 fb^{-1} it will be relatively easy to isolate a signal of one or two hundred events over a similarly sized background, but, given the small size, its exploitation appears dubious.

3.4. Lepton Angular Distributions in W Boson Decay

Next-to-leading order perturbative QCD predicts that in $W \rightarrow l\nu$ decays an angular distribution of $(1 \pm \alpha_1 \cos\theta^* + \alpha_2 \cos^2\theta^*)$ [108] should be observed, where θ^* is the polar angle of the decay lepton in the Collins-Soper frame [109]. In the presence of QCD corrections, the parameters α_1 and α_2 are functions of p_T^W , the W boson transverse momentum.

The measurement of α_2 serves as a probe of NLO QCD, using the well understood W -fermion coupling.

By probing the spin structure of W production, this measurement provides another method that is independent of purely QCD analyses, while adding to the list of measurements using vector bosons to study NLO QCD. Moreover, the measurement of the angular distribution of the decay leptons is also of importance for the W mass measurements, because the next-to-leading order QCD corrections to the angular distribution are a non-negligible contribution to the W mass.

The measurement of the angular distribution of electrons from W bosons obtained with Run I data collected by DØ [110, 111] is statistically limited (see Fig. 52). While a calculation that includes QCD effects is preferred over one that does not, this preference is not strong enough to exclude a p_T independent angular parameter α_2 . With the next collider run starting in the near future, it is worthwhile looking at the sensitivity of this measurement in Run II. In the following discussion we will estimate the size of statistical and systematic errors to this measurement with 2 fb^{-1} in Run II.

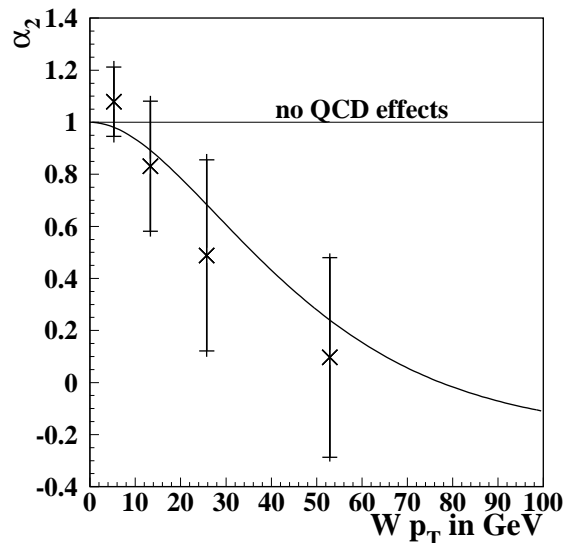


Figure 52. DØ Run I result: the measured α_2 as a function of p_T with combined statistical and systematic errors compared to the NLO QCD calculation by Mirkes (curve) and calculation in the absence of QCD effects (horizontal line). The statistical errors alone are shown as horizontal ticks.

The expected statistical errors in the determination

of α_2 should simply scale like the inverse of the square root of the number of events. We consequently need to calculate the expected number of W boson events under Run II conditions. We get a factor of 57 in W boson statistics which breaks down as follows (see [77]):

$$\frac{N_{W,RunII}}{N_{W,RunI}} = f_{lum} \times f_{2.0TeV} \times \frac{N_e + N_\mu}{N_e} \times \frac{\epsilon_{tracking}}{\epsilon_{no tracking}} \quad (3)$$

where $f_{lum} = 20$ indicates the increase in luminosity, $f_{2.0TeV} = 1.2$ indicates the increase in W cross section due to the increase of the center-of-mass energy from $\sqrt{s} = 1.8$ TeV to 2 TeV, $(N_e + N_\mu)/N_e = 2$ is the additional statistics gained by including the muon channel, and

$$\frac{\epsilon_{tracking}}{\epsilon_{no tracking}} = \frac{0.95}{0.8} \quad (4)$$

is the increase in efficiency due to tracking capabilities of the upgraded DØ detector.

The statistical errors of the Run I measurement are therefore scaled by $1/\sqrt{57}$, as shown in Fig. 53. The

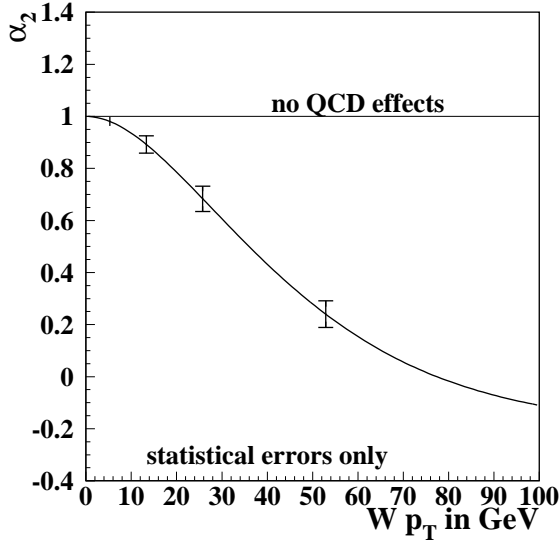


Figure 53. Estimated sensitivity of the α_2 measurement obtained by scaling statistical errors to Run II conditions.

statistical uncertainties to this measurement become quite small, and a further look at systematic errors

is therefore necessary. Table 5 shows a summary of statistical and systematic errors for Run I and Run II. Since the modeling of the hadronic recoil is done from Z data, the error due to the hadronic resolution will scale with Z statistics up to a point. The estimate of this error is done by scaling the number of Z events by a factor of $\sqrt{28.5}$ (the same as for W events but excluding muons). The error on the hadronic response will also improve with increased Z statistics. Consequently, the largest errors left are the ones due to the QCD multi-jet background and the electromagnetic scale. It will be of crucial importance for this and other electroweak measurements to better estimate the QCD background. This goal can partially be reached by taking more events with a QCD monitor trigger [111]. Of course, it would be best if the QCD background fraction could be reduced even further. At this point it is not obvious if this is feasible since the current set of electron identification cuts is already very efficient in reducing this background. A Monte Carlo program that correctly models QCD multi-jet events including a realistic detector model could also help in better estimating the shape of this background. For the low p_T region, the dominant error will be the electromagnetic scale. There is however currently no good estimate by how much this error will be reduced.

Table 5

Central values and statistical errors for α_2 and systematic errors due to backgrounds, the hadronic energy scale and resolution, and the choice of α_1 . All systematic errors are for Run I if not otherwise noted.

p_T [GeV]	0 – 10	10 – 20	20 – 35	35 – 200
mean p_T [GeV]	5.3	13.3	25.7	52.9
α_2 , Run I	1.07 ± 0.13	0.82 ± 0.25	0.49 ± 0.37	0.10 ± 0.37
α_2 , Run II	0.98	0.89	0.68	0.24
Stat. errors, e	± 0.024	± 0.047	± 0.069	± 0.069
e+ μ	± 0.017	± 0.033	± 0.049	± 0.049
total syst error	± 0.08	± 0.09	± 0.12	± 0.12
QCD	± 0.04	± 0.05	± 0.09	± 0.07
Z	± 0.01	± 0.02	± 0.02	± 0.04
top	± 0.00	± 0.00	± 0.00	± 0.02
EM scale	± 0.06	± 0.05	± 0.03	± 0.04
had scale	± 0.03	± 0.01	± 0.04	± 0.04
had. resolution	± 0.02	± 0.02	± 0.05	± 0.06
had. res. Run II	± 0.004	± 0.004	± 0.009	± 0.011
α_1	± 0.01	± 0.05	± 0.03	± 0.03

In the current measurement we had to fix α_1 to the value predicted by the QCD calculation since even after summing over both W signs we are slightly sensitive to α_1 due to acceptance effects. The error due to this

choice for α_1 was estimated by setting $\alpha_1 = 2.0$, the value predicted by the $V - A$ theory in the absence of QCD effects (see Table 5). This error is non-negligible. Since the central magnet in Run II will allow for sign identification of electrons, α_1 and α_2 could thus be measured simultaneously, eliminating the need for the above assumption for α_1 . This will reduce the error due to the choice of α_1 . While this is a nice extension of this measurement, it is not clear at this point by how much it will numerically improve the significance of the measurement of α_2 .

In the above estimate of the errors, the binning in p_T^W used for the Run I measurement was kept unchanged. With larger statistics, one would probably choose a finer binning in p_T^W , allowing for bins with larger mean p_T^W . This would increase the sensitivity in the area where the deviation of the angular distribution due to QCD effects is most pronounced.

The Monte Carlo used in the current analysis, which was originally developed for the measurement of the W mass [88] at $D\bar{O}$, treats hadronic jets as point particles and the hadronic recoil is treated as a single jet. This is clearly a simplification of the true processes involved and a real next-to-leading order event generator would be useful.

In addition to the experimental improvements discussed thus far, this measurement will be sensitive to W production models. These models have to be constrained by independent measurements.

To summarize, in Run II the measurement of the angular distribution of electrons from W boson decays will be systematically limited. While the recoil response and resolution will improve with increased Z statistics, the estimate of the QCD background fraction and shape becomes a limiting factor. It is difficult to estimate by how much the other dominant error, the error due to the uncertainty of the electromagnetic scale, will be reduced in Run II. Other improvements not quantified here are expected from a finer binning in p_T and sign identification of electrons.

4. Vector Boson Pair Production and Trilinear Gauge Boson Couplings – Prospects for Run II[§]

The Standard Model of electroweak interactions makes precise predictions for the couplings between gauge bosons due to the non-abelian gauge symmetry of $SU(2)_L \otimes U(1)_Y$. These self-interactions are described by the triple gauge boson (trilinear) $WW\gamma$, WWZ , $Z\gamma\gamma$, $ZZ\gamma$ and ZZZ couplings and the quartic couplings. Vector boson pair production provides a sensitive ground for *direct tests* of the trilinear cou-

plings. Deviations of the couplings from the SM values would indicate the presence of new physical phenomena.

The purpose of this section is to present a brief overview of recent theoretical advances in understanding di-boson production in hadronic collisions, and to highlight Run II opportunities for studying the physics of vector boson pair production. Because of the large anticipated size of the data sample, $\int \mathcal{L} dt = 2 \text{ fb}^{-1}$, interesting processes and final states that were not studied in Run I will become available. These are discussed, as well as prospects available in extensions of the Run I $W\gamma$, WW , and WZ analyses to Run II. This is meant to be an improvement over the forecasts of the TeV_2000 Report [77], which was written in 1995 before we had the benefit of having performed the Run Ib analyses. Indeed, some of the TeV_2000 Report's prognostications for Run II limits were achieved in Run I.

We begin with a brief summary of the trilinear gauge boson couplings and how they are parameterized. Next, we give a short description of new theoretical developments. Following that, we summarize the anomalous coupling limits obtained in Run Ia and Run Ib, and compare the Run Ib results with what we expected we would obtain, based on a simple extrapolation from Run Ia. This exercise in hindsight provides both a calibration for, and a cross-check of, the extrapolation method. The subsequent section provides expectations for anomalous coupling limits from the Run II analyses based on extrapolation of the Run I analyses to higher integrated luminosity. Next, we provide comments on some Run II analyses, and, lastly, discuss new channels and analyses which will become feasible in Run II, in particular the prospects for measuring the ZZV couplings via ZZ production.

4.1. Trilinear Couplings

The WWV ($V = \gamma$ or Z) vertices are described by a general effective Lagrangian [112, 113] with two overall couplings, $g_{WW\gamma} = -e$ and $g_{WWZ} = -e \cdot \cot \theta_W$, and six dimensionless couplings g_1^V , κ_V , and λ_V ($V = \gamma$ or Z), after imposing C , P , and CP invariance. The $W_\alpha^-(q) W_\beta^+(\bar{q}) V_\mu(p)$ vertex function (where all momenta are outgoing, $p + q + \bar{q} = 0$) in presence of

[§]Contributed by: U. Baur, H.T. Diehl and D. Rainwater

non-standard couplings is given by:

$$\begin{aligned} \frac{\Gamma_{WWV}^{\alpha\beta\mu}}{g_{WWV}} &= \bar{q}^\alpha g^{\beta\mu} \left(g_1^V + \kappa_V + \lambda_V \frac{q^2}{M_W^2} \right) \\ &\quad - q^\beta g^{\alpha\mu} \left(g_1^V + \kappa_V + \lambda_V \frac{\bar{q}^2}{M_W^2} \right) \\ &\quad - (\bar{q}^\mu - q^\mu) g^{\alpha\beta} \left(g_1^V + \frac{\lambda_V}{2} \frac{p^2}{M_W^2} \right) \\ &\quad + (\bar{q}^\mu - q^\mu) \frac{\lambda_V}{M_W^2} p^\alpha p^\beta. \end{aligned} \quad (5)$$

Here, M_W is the W -boson mass. Electromagnetic gauge invariance requires that $g_1^\gamma = 1$, which we assume throughout this paper. The SM Lagrangian is obtained by setting $g_1^\gamma = g_1^Z = 1$, $\kappa_V = 1$ ($\Delta\kappa_V \equiv \kappa_V - 1 = 0$) and $\lambda_V = 0$.

A different set of parameters, motivated by $SU(2) \times U(1)$ gauge invariance, had been used by the LEP collaborations [114] prior to 1998. This set consists of three independent couplings $\alpha_{B\phi}$, $\alpha_{W\phi}$ and α_W : $\alpha_{B\phi} \equiv \Delta\kappa_\gamma - \Delta g_1^Z \cos^2 \theta_W$, $\alpha_{W\phi} \equiv \Delta g_1^Z \cos^2 \theta_W$ and $\alpha_W \equiv \lambda_\gamma$. The remaining WWZ coupling parameters λ_Z and $\Delta\kappa_Z$ are determined by the relations $\lambda_Z = \lambda_\gamma$ and $\Delta\kappa_Z = -\Delta\kappa_\gamma \tan^2 \theta_W + \Delta g_1^Z$. The HISZ relations [115] which have been used by the DØ and CDF collaborations are also based on this set with the additional constraint $\alpha_{B\phi} = \alpha_{W\phi}$.

The di-boson production cross sections with non-SM couplings grow with the parton center of mass energy $\sqrt{\hat{s}}$. In order to avoid violation of S -matrix unitarity, the anomalous couplings $a = g_1^V$, $\Delta\kappa_V$, λ_V are taken as momentum dependent form factors with a scale Λ_{FF}

$$a(\hat{s}) = \frac{a}{(1 + \hat{s}/\Lambda_{FF}^2)^n} \quad (6)$$

and $n = 2$ (dipole form factor).

The $Z^\alpha(q_1) \gamma^\beta(q_2) V^\mu(P)$ ($V = \gamma$ or Z) vertices contributing to $Z\gamma$ production are described by a general vertex function [112] with eight dimensionless couplings h_i^V ($i = 1, \dots, 4$; $V = \gamma$ or Z):

$$\begin{aligned} \Gamma_{Z\gamma V}^{\alpha\beta\mu} &= \frac{P^2 - q_1^2}{M_Z^2} \left\{ h_1^V (q_2^\mu g^{\alpha\beta} - q_2^\alpha g^{\mu\beta}) \right. \\ &\quad + \frac{h_2^V}{M_Z^2} P^\alpha ((P \cdot q_2) g^{\mu\beta} - q_2^\mu P^\beta) \\ &\quad + h_3^V \epsilon^{\mu\alpha\beta\rho} q_{2\rho} \\ &\quad \left. + \frac{h_4^V}{M_Z^2} P^\alpha \epsilon^{\mu\beta\rho\sigma} P_\rho q_{2\sigma} \right\}. \end{aligned} \quad (7)$$

In the SM, all h_i^V 's are zero. The couplings h_1^V and h_2^V violate CP ; all couplings are C -odd. The form

factors for these couplings are

$$h_i^V(\hat{s}) = \frac{h_{i0}^V}{(1 + \hat{s}/\Lambda_{FF}^2)^n}, \quad (8)$$

where one usually assumes that $n = 3$ for $i = 1, 3$ and $n = 4$ for $i = 2, 4$ [107].

In the SM, the $\ell^+ \ell^- \gamma$ final state can be produced via radiative decays of the Z boson or by production of a boson pair via t - or u -channel quark exchange. The former process is the dominant source of events with small opening angle between the photon and charged lepton and for events with a low value of photon transverse energy, E_T^γ . Events produced by the latter process have lepton-pair invariant mass, $m_{\ell\ell}$, close to M_Z and three-body invariant mass, $m_{\ell\ell\gamma}$, larger than M_Z . Anomalous $ZZ\gamma$ or $Z\gamma\gamma$ couplings would enhance the cross section for $Z\gamma$ production, particularly for high- E_T photons, relative to the SM expectations.

The most general form of the $Z^\alpha(q_1) Z^\beta(q_2) V^\mu(P)$ vertex function can be written in the form [112]

$$\begin{aligned} \Gamma_{ZZV}^{\alpha\beta\mu} &= \frac{P^2 - M_V^2}{M_Z^2} \left(i f_4^V (P^\alpha g^{\mu\beta} + P^\beta g^{\mu\alpha}) \right. \\ &\quad \left. + i f_5^V \epsilon^{\mu\alpha\beta\rho} (q_1 - q_2)_\rho \right). \end{aligned} \quad (9)$$

CP invariance forbids f_4^V and parity conservation requires that f_5^V vanishes. In the SM, $f_4^V = f_5^V = 0$. S -matrix unitarity requires a form factor behavior for ZZV couplings similar to that of h_1^V and h_3^V [116] (Eq. (8) with $n = 3$).

Although the WWV , $Z\gamma V$ and ZZV couplings usually are assumed to be real, they are in general complex quantities.

In theories which go beyond the SM, the WWV couplings are expected to be at most $\mathcal{O}(M_W^2/\Lambda^2)$ where $\Lambda \sim \Lambda_{FF}$ is the scale of new physics. $Z\gamma V$ and ZZV couplings are at most $\mathcal{O}(M_Z^4/\Lambda^4)$.

4.2. Recent Theoretical Developments

4.2.1. Parameterization of $Z\gamma V$ Couplings

In Ref. [117] it was pointed out that the couplings h_i^V have to be purely imaginary quantities in order to guarantee that an effective Lagrangian which would lead to a vertex function of the form of Eq. (7) is hermitian. In contrast, the WWV and ZZV couplings are normalized such that real couplings automatically correspond to a hermitian effective Lagrangian. Since one usually assumes real couplings when placing limits on anomalous vector boson self-couplings, it is useful to replace the couplings h_i^V by

$$h_i^V = -i h_i^V \quad (10)$$

for the Run II analyses and beyond.

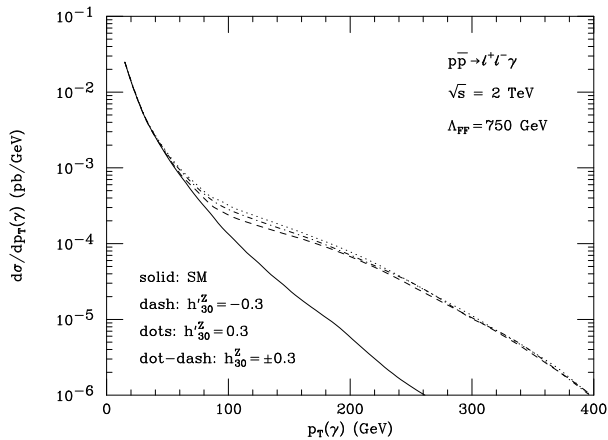


Figure 54. The photon transverse momentum distribution in $p\bar{p} \rightarrow \ell^+ \ell^- \gamma$ at the Tevatron in the SM and for anomalous $ZZ\gamma$ couplings. The cuts imposed are described in the text.

$h'_i{}^V$'s and $h_i{}^V$'s of equal magnitude result in virtually the same differential cross sections at high energies. This is illustrated in Fig. 54 for the case $|h'_{30}{}^Z| = |h_{30}{}^Z| = 0.3$. In order to simulate detector response, the following cuts have been imposed in Fig. 54:

$$p_T(\gamma) > 10 \text{ GeV}, \quad |\eta(\gamma)| < 2.5, \quad (11)$$

$$p_T(\ell) > 20 \text{ GeV}, \quad |\eta(\ell)| < 2.5, \quad (12)$$

$$m(\ell\ell) > 75 \text{ GeV}, \quad m(\ell\ell\gamma) > 100 \text{ GeV}, \quad (13)$$

and

$$\Delta R(\ell\gamma) > 0.7. \quad (14)$$

The form factor scale has been chosen to be $\Lambda_{FF} = 750 \text{ GeV}$.

Unlike for real $h_{3,4}{}^V$ couplings, the interference terms between the SM and the non-SM contributions do not vanish in the squared matrix element for real values of $h'_{3,4}{}^V$. Thus, for intermediate values of $p_T(\gamma)$, the differential cross sections for values of $h'_{3,4}{}^V$ of equal magnitude but opposite sign slightly differ. Since most of the sensitivity to anomalous couplings originates from the high energy domain, the limits for $h'_i{}^V$ are expected to be almost identical to those obtained for $h_i{}^V$. In the following we therefore list limits only for $h_i{}^V$.

4.2.2. NLO QCD Corrections to Vector Boson Pair Production

In the Run I di-boson analyses, data were compared with leading order production calculations to extract limits on the WWV and $Z\gamma V$ couplings. The effect

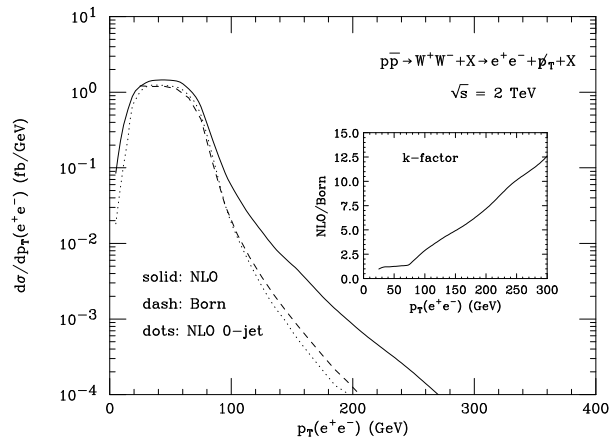


Figure 55. The e^+e^- transverse momentum distribution in $p\bar{p} \rightarrow W^+W^- + X \rightarrow e^+e^- \not{p}_T + X$ at the Tevatron in the SM. The following cuts were imposed to simulate detector response: $p_T(e) > 20 \text{ GeV}$, $|\eta(e)| < 2.5$ and $\not{p}_T > 20 \text{ GeV}$. For the NLO 0-jet curve (dotted line), jets with $p_T(j) > 20 \text{ GeV}$ and $|\eta(j)| < 3.5$ were vetoed.

of higher order QCD corrections was simulated by multiplying the differential cross sections by a simple constant k -factor

$$k = 1 + \frac{8\pi}{9} \alpha_s. \quad (15)$$

NLO calculations have shown [118] that the $\mathcal{O}(\alpha_s)$ QCD corrections in the SM depend logarithmically on \hat{s} and become large at high energies, due to gluon-induced partonic subprocesses, which only enter at NLO. An example is shown in Fig. 55, where we display the transverse momentum distribution of the charged lepton pair in $p\bar{p} \rightarrow W^+W^- + X \rightarrow e^+e^- \not{p}_T + X$. NLO corrections are seen to be very large ($\mathcal{O}(10)$) at high p_T , and dramatically alter the shape of the distribution. Qualitatively this is precisely what one expects from non-standard WWV couplings. Since the real emission diagrams are responsible for the increase of the QCD corrections with p_T , a jet veto drastically reduces the size of the QCD corrections (dotted line). It should be noted that the NLO QCD corrections reduce the W^+W^- cross section when a jet veto is imposed.

With the more than 20-fold increase in statistics expected in Run II, it is clear that the QCD corrections to di-boson production must properly be taken into account when information on anomalous couplings is extracted. Over the past seven years the NLO QCD corrections to $W\gamma$ [119], $Z\gamma$ [120], WW [121] and WZ production [122] including non-standard WWV

Table 6

The $p\bar{p} \rightarrow W^+W^- + X \rightarrow e^+e^- \cancel{p}_T + X$ cross section for $\sqrt{s} = 2$ TeV with $p_T(e) > 20$ GeV, $|\eta(e)| < 2.5$, and $\cancel{p}_T > 20$ GeV. Jets are required to have $p_T(j) > 20$ GeV, $|\eta(j)| < 2.5$. Results are shown for the calculations of Ref. [121] (BHO) and Ref. [124] (DKS) with factorization scale $Q^2 = M_W^2$, and using the CTEQ4M [126] set of parton distribution functions.

	BHO	DKS
	σ (fb)	σ (fb)
Standard Model		
Born	61.2	61.2
NLO	80.9	81.3
NLO 0-jet	65.6	65.3
$\Delta g_1^Z = 0.5, \lambda_Z = \lambda_\gamma = 0.1, \Delta\kappa_Z = \Delta\kappa_\gamma = 0.3$ $\Lambda_{FF} = 2$ TeV		
Born	82.7	82.8
NLO	106.5	107.0
NLO 0-jet	84.2	83.7

and $Z\gamma V$ couplings have been calculated using the narrow width approximation and ignoring spin correlations in the finite virtual corrections. Recently, more complete calculations have become available which properly take into account the previously ignored spin correlations. Ref. [123] also includes single resonant diagrams and finite W and Z width effects in the calculation; however, no anomalous couplings are taken into account. Refs. [124, 125] use the narrow width approximation, but do include the option of non-standard WWV couplings.

The contribution of the finite virtual corrections to the NLO cross section is smaller than about 10% for all di-boson processes. The spin correlations ignored in Refs. [119, 120, 121, 122] therefore are expected to have a rather small effect on the total cross section, as well as on most distributions. This expectation is confirmed by an explicit comparison between the calculations of Refs. [124] (DKS) and [121] (BHO) for W^+W^- production which is shown in Table 6. The two calculations are seen to agree at the 1% level.

A more detailed and careful comparison between the BHO and DKS calculations for W^+W^- and $W^\pm Z$ production at the LHC has been carried out in Ref. [127]. The WZ cross sections of the two calculations were found to agree within 1.5%, whereas in the WW case deviations of up to 3.8% were observed at NLO. Subsequently, a small error in the BHO W^+W^- code was discovered [128]. After correction of this error, the BHO and DKS calculations of W^+W^- production at the LHC agree to better than 0.5% [128].

4.3. Summary of Run Ia and Run Ib Analyses at CDF and DØ

This subsection contains a summary of the published CDF and DØ analyses. The intent is to provide an overview of the progress, a list of published papers, and tables which provide the basis for the comparison made in the next subsection.

4.3.1. $WW\gamma$ and WWZ Couplings

The DØ and CDF collaborations have performed several searches for anomalous $WW\gamma$ and WWZ couplings. Studies [129, 130, 131] of $p\bar{p} \rightarrow W\gamma + X$ have shown that the transverse energy spectrum of the photons agreed with that expected from SM production. Searches [132, 133, 134] for an excess of $p\bar{p} \rightarrow WW + X$, where the W bosons each decayed to $\ell\nu$ ($\ell = e$ or μ), yielded events which matched the SM prediction. Further, the p_T spectrum of the charged leptons agreed [134] with the prediction. Studies [135, 136, 137, 138] of the processes $p\bar{p} \rightarrow WW + X$ and $p\bar{p} \rightarrow WZ + X$, where one W boson decayed to a lepton or anti-lepton and the corresponding anti-neutrino or neutrino and the other vector boson decayed to a quark-antiquark pair manifested as jets, yielded no excess of events and a W boson transverse energy spectrum which matched the expected background plus SM signal. Lastly, DØ studied [138] the process $p\bar{p} \rightarrow WZ + X$ where the Z boson decayed to ee and the W boson decayed to either $e\nu$ or $\mu\nu$. Limits on anomalous $WW\gamma$ and WWZ couplings were derived from each of these analyses. Several [130, 132, 136] of these analyses were presented in detail in Ref. [139]. The results of all of the DØ analyses were combined [138], using the maximum-likelihood method [139, 140], to form the Tevatron's most restrictive limits on anomalous $WW\gamma$ and WWZ couplings.

Table 7 shows the anomalous coupling limits achieved in each of the analyses described above, the luminosity used, and the reference to the paper in which the result was published. It should be noted that many of the papers published limits under several assumptions for the relations between the coupling parameters and with several values of the form factor Λ_{FF} . Only those limits from the case $\lambda = \lambda_\gamma = \lambda_Z$ and $\Delta\kappa = \Delta\kappa_\gamma = \Delta\kappa_Z$ are listed, except for $W\gamma$ and WZ where only $WW\gamma$ and WWZ couplings, respectively, are relevant.

4.3.2. $Z\gamma V$ Couplings

The DØ and CDF collaborations have also performed several searches for anomalous $Z\gamma\gamma$ and $ZZ\gamma$ couplings. Studies [141, 142, 143] of the process $p\bar{p} \rightarrow Z\gamma + X \rightarrow \ell^+\ell^-\gamma + X$ have shown that the event yield and transverse energy spectrum of the photons agreed with that expected from SM $Z\gamma$ production,

Table 7

95% confidence level $WW\gamma$ and WWZ anomalous coupling limits achieved in Run I analyses by the DØ and CDF Collaborations.

Analysis	Ref.	Run	Lum. (pb ⁻¹)	Λ_{FF}	A.C. Limit (95% CL)
CDF $W\gamma \rightarrow e\nu\gamma$ and $\mu\nu\gamma$	[129]	Ia	20	1.5 TeV	$-0.7 \leq \lambda \leq 0.7$ $-2.2 \leq \Delta\kappa \leq 2.3$
DØ $W\gamma \rightarrow e\nu\gamma$ and $\mu\nu\gamma$	[130]	Ia	13.8	1.5 TeV	$-0.6 \leq \lambda \leq 0.6$ $-1.6 \leq \Delta\kappa \leq 1.8$
DØ $W\gamma \rightarrow e\nu\gamma$ and $\mu\nu\gamma$	[131]	Ia + Ib	92.8	1.5 TeV	$-0.31 \leq \lambda \leq 0.29$ $-0.93 \leq \Delta\kappa \leq 0.94$
DØ $WW \rightarrow$ Dilepton	[132]	Ia	14	900 GeV Equal Couplings	$-2.1 \leq \lambda \leq 2.1$ $-2.6 \leq \Delta\kappa \leq 2.8$
CDF $WW \rightarrow$ Dilepton	[133]	Ia + Ib	108	1.0 TeV Equal Couplings	$-0.9 \leq \lambda \leq 0.9$ $-1.0 \leq \Delta\kappa \leq 1.3$
DØ $WW \rightarrow$ Dilepton	[134]	Ia + Ib	97	1.5 TeV Equal Coupling	$-0.53 \leq \lambda \leq 0.56$ $-0.62 \leq \Delta\kappa \leq 0.77$
CDF WW and $WZ \rightarrow$ leptons + jets	[135]	Ia	19.6	1.0 TeV Equal Couplings	$-0.81 \leq \lambda \leq 0.84$ $-1.11 \leq \Delta\kappa \leq 1.27$
DØ WW and $WZ \rightarrow e\nu_{jj}$	[136]	Ia	13.7	1.5 TeV Equal Couplings	$-0.6 \leq \lambda \leq 0.7$ $-0.9 \leq \Delta\kappa \leq 1.1$
DØ WW and $WZ \rightarrow e\nu_{jj}$	[137]	Ia + Ib	96	1.5 TeV Equal Couplings	$-0.36 \leq \lambda \leq 0.39$ $-0.47 \leq \Delta\kappa \leq 0.63$
DØ WW and $WZ \rightarrow e\nu_{jj}$	[137]	Ia + Ib	96	2.0 TeV Equal Couplings	$-0.33 \leq \lambda \leq 0.36$ $-0.43 \leq \Delta\kappa \leq 0.59$
DØ WW and $WZ \rightarrow \mu\nu_{jj}$	[138]	Ib	81	2.0 TeV Equal Couplings	$-0.43 \leq \lambda \leq 0.44$ $-0.60 \leq \Delta\kappa \leq 0.74$
DØ $WZ \rightarrow ee\mu\nu$ and $ee\nu\nu$	[138]	Ib	92	1.0 TeV	$-1.42 \leq \lambda_Z \leq 1.42$ $-1.63 \leq \Delta g_1^Z \leq 1.63$
DØ Combined	[138]	Ia + Ib	96	2.0 TeV Equal Couplings	$-0.18 \leq \lambda \leq 0.19$ $-0.25 \leq \Delta\kappa \leq 0.39$

though it is noted that there were two $Z\gamma \rightarrow ee\gamma$ events with photons of E_T greater than 70 GeV, expected in only 7.3% of trial experiments.

Studies of the process $Z\gamma \rightarrow \nu\bar{\nu}\gamma$ have the advantage of the higher branching fraction for decay to neutrinos than does the charged-lepton decay mode. Furthermore, there is no final state radiation because the neutrinos are electrically neutral. However, the signal-to-background ratio is rather lower than in the charged-lepton analysis. DØ has published [144] the results of the Run Ia $Z\gamma \rightarrow \nu\bar{\nu}\gamma$ analysis. Again, the spectrum of the transverse energy of the photons, for $E_T^\gamma \geq 40$ GeV, agreed with the SM prediction.

DØ and CDF produced limits on anomalous $Z\gamma V$ ($V = Z, \gamma$) couplings using a fit to the E_T^γ spectrum. The DØ Run Ia and Run Ib results were combined in Ref. [143]. Table 8 shows a compilation of all the Run I CDF and DØ results. The limits for h_{30}^γ (h_{40}^γ) and h_{10}^V (h_{20}^V) are almost identical to those obtained for h_{30}^Z (h_{40}^Z) and are, therefore, not shown.

4.4. Hindsight: Extrapolating Run Ia Results to Run Ib

It is interesting to see how well one can “predict” the Run Ib limits based on the Run Ia results and a simple rule for scaling the limits based on the increase in the luminosity.

The $WW\gamma$ and WWZ anomalous coupling limits should scale by

$$\left(\int \mathcal{L} dt \right)^{1/4}. \quad (16)$$

One square-root comes from the decrease in the statistical uncertainty of the cross section (as a function of E_T , for instance) and the other from the fact that the differential cross section is a quadratic function of the anomalous couplings.

The $Z\gamma\gamma$ and $ZZ\gamma$ anomalous coupling limits would also scale by the fourth-root of the ratio of the luminosities, except that the limits depend very strongly on the form-factor scale.

Table 8

95% confidence level $ZZ\gamma$ and $Z\gamma\gamma$ anomalous coupling limits achieved in the Run I analyses by the DØ and CDF Collaborations.

Analysis	Ref.	Run	Lum. (pb ⁻¹)	Λ_{FF}	A.C. Limit (95% CL)
CDF $Z\gamma \rightarrow ee\gamma$ and $\mu\mu\gamma$	[141]	Ia	20	500 GeV	$-3.0 \leq h_{30}^Z \leq 3.0$ $-0.7 \leq h_{40}^Z \leq 0.7$
DØ $Z\gamma \rightarrow ee\gamma$ and $\mu\mu\gamma$	[142]	Ia	14	500 GeV	$-1.8 \leq h_{30}^Z \leq 1.8$ $-0.5 \leq h_{40}^Z \leq 0.5$
DØ $Z\gamma \rightarrow \nu\bar{\nu}\gamma$	[143]	Ia	13	750 GeV	$-0.4 \leq h_{30}^Z \leq 0.4$ $-0.06 \leq h_{40}^Z \leq 0.06$
DØ $Z\gamma \rightarrow ee\gamma$ and $\mu\mu\gamma$	[144]	Ib	97	500 GeV	$-1.31 \leq h_{30}^Z \leq 1.31$ $-0.26 \leq h_{40}^Z \leq 0.26$
DØ $Z\gamma \rightarrow ee\gamma$ and $\mu\mu\gamma$	[144]	Ib	97	750 GeV	$-0.69 \leq h_{30}^Z \leq 0.69$ $-0.08 \leq h_{40}^Z \leq 0.08$
DØ Combined	[144]	Ia + Ib		750 GeV	$-0.36 \leq h_{30}^Z \leq 0.36$ $-0.05 \leq h_{40}^Z \leq 0.05$

4.4.1. $W\gamma$

The integrated luminosity used in DØ's Run Ia + Run Ib $W\gamma$ analysis was 6.72 times larger than the Run Ia sample alone. From that we expect the combined anomalous coupling limits to be $(1/6.72)^{1/4} = 0.62$ as large as the Run Ia limits. Scaling the Run Ia results in Table 7, we would expect limits $-1.0 \leq \Delta\kappa_\gamma \leq 1.1$ and $-0.38 \leq \lambda_\gamma \leq 0.38$. Instead, from Table 7, the result was equivalent to a scaling of ~ 0.52 . That does not seem very different, but it is, for it corresponds to the equivalent of a factor of two more luminosity. The difference is attributed to an improvement in technique, the use of a three-body transverse mass criteria to remove events where the photon was radiated from a charged final state lepton. It's hard to predict improvement techniques because, if such improvements were a priori known, they would most likely have been applied.

4.4.2. $WW/WZ \rightarrow e\nu jj$

We expect the Run Ia + Run Ib limits to scale by 0.61 from the ratio of the integrated luminosities. Consulting Table 7, we find that this is essentially right on the nose for the $\Lambda_{FF} = 1.5$ TeV limits. The Run Ia + Ib $\Lambda_{FF} = 2$ TeV limits, not available because of unitarity constraints in the Run Ia sample, represent a slight ($\sim 10\%$) improvement over the Run Ia + Ib $\Lambda_{FF} = 1.5$ TeV results.

4.4.3. $WW \rightarrow$ dileptons

We expect the Run Ia + Run Ib limits to scale by 0.62 from the ratio of the integrated luminosities. However, that is not what happened. An important

improvement in the technique, namely a 2-D fit to the lepton E_T spectrum, plus the subsequent increase in the allowed form factor, allowed the combined results to be almost a factor of four better. Here is a case where we have already challenged the Run II limits predicted by the TeV_2000 report.

4.4.4. $Z\gamma \rightarrow ee\gamma$ and $\mu\mu\gamma$

Again, by the fourth-root rule, we expect the Run Ib limits to scale by 0.62. For $\Lambda_{FF} = 500$ GeV, we found that the h_{30}^Z results scaled by 0.72 and the h_{40}^Z by 0.52, averaging out to a scale factor of 0.62. But, because of the strong dependence on the form factor scale, the results at $\Lambda_{FF} = 750$ GeV are 3.5 and 5 times better for h_{30}^Z and h_{40}^Z , respectively.

4.5. Expectations for Run II Anomalous Coupling Limits

Having probed the usefulness and limitations of our scaling formula, we apply it to the Run I analyses to determine the limits that might be attained with 2 fb^{-1} . Of course, any projections for anomalous coupling limits are merely sensitivity estimates. Improvements in technique, such as multi-dimensional fits, or using clever projection techniques (see Ref. [145] for an example) may yield more stringent limits.

For the $W\gamma$ and WW/WZ analyses we will use an integrated luminosity scale factor $(2000/100)^{1/4} = 2.1$. The slight improvement from the $\approx 10\%$ increase in cross section available should the Tevatron operate at center of mass energy 2000 GeV is ignored. Increasing the form factor scale from 1.5 TeV to 2 TeV strengthens the limits by about 10%. The $WZ \rightarrow$ tripletons

Table 9

95% confidence level $WW\gamma$ and WWZ anomalous coupling limits that might be achieved by $D\bar{O}$ or CDF in Run II.

Analysis	Lum. (pb^{-1})	Λ_{FF}	A.C. Limit (95% CL)
$W\gamma \rightarrow$ $e\nu\gamma$ and $\mu\nu\gamma$	2000	1.5 TeV	$-0.14 \leq \lambda \leq 0.14$
		Equal Couplings	$-0.44 \leq \Delta\kappa \leq 0.44$
$W\gamma \rightarrow$ $e\nu\gamma$ and $\mu\nu\gamma$	2000	2.0 TeV	$-0.12 \leq \lambda \leq 0.12$
		Equal Couplings	$-0.40 \leq \Delta\kappa \leq 0.40$
WW and $WZ \rightarrow$ $e\nu jj$	2000	2.0 TeV	$-0.16 \leq \lambda \leq 0.17$
		Equal Couplings	$-0.20 \leq \Delta\kappa \leq 0.28$
$WZ \rightarrow$ trileptons	2000	2.0 TeV	$-0.2 \leq \lambda_Z \leq 0.2$ $-0.3 \leq \Delta g_1^Z \leq 0.3$
Combined (per experiment)	2000	2.0 TeV	$-0.086 \leq \lambda \leq 0.090$ $-0.12 \leq \Delta\kappa \leq 0.19$

analysis will improve by about a factor of 6 because of the increased integrated luminosity and because of the improvement in limit-setting technique available by fitting the E_T spectrum of the Z bosons. Table 9 contains the expected results. In order to put these bounds into perspective, we list the most recent LEP2 (95% CL) limits from a 3-parameter fit [146], assuming $\Delta\kappa_Z = \Delta g_1^Z - \Delta\kappa_\gamma \tan^2 \theta_W$ and $\lambda_Z = \lambda_\gamma$:

$$-0.073 < \Delta g_1^Z < 0.075, \quad (17)$$

$$-0.12 < \Delta\kappa_\gamma < 0.16, \quad (18)$$

$$-0.15 < \lambda_\gamma < 0.01. \quad (19)$$

It should be noted that form factor effects are *not* included in the bounds obtained at LEP2. Taking into account the form factor behavior of anomalous couplings weakens the limits obtained. For a dipole form factor with $\Lambda_{FF} = 2$ TeV, this is a 2% effect.

For anomalous $Z\gamma\gamma$ and $ZZ\gamma$ couplings we forecast limits which are very similar to those given in the Tev_2000 Report. Those predictions are based on 1 fb^{-1} integrated luminosity and $\Lambda_{FF} = 1500$ GeV and are listed in Table 10. The bounds obtained for h_{10}^V (h_{20}^V) almost coincide with those found for h_{30}^V (h_{40}^V). For comparison, the most recent 95% CL limits on h_i^V from LEP2 are:

$$-0.17 < h_1^\gamma < 0.08 \quad -0.26 < h_1^Z < 0.09, \quad (20)$$

$$-0.11 < h_2^\gamma < 0.10 \quad -0.11 < h_2^Z < 0.16, \quad (21)$$

$$-0.027 < h_3^\gamma < 0.041 \quad -0.29 < h_3^Z < 0.21, \quad (22)$$

$$-0.026 < h_4^\gamma < 0.022 \quad -0.12 < h_4^Z < 0.20. \quad (23)$$

Only one coupling at a time is varied here. Correcting for form factor effects, the limits for $h_{1,3}$ ($h_{2,4}$) weaken by about 5% (7%) for $\Lambda_{FF} = 1500$ GeV.

In Run II, the Tevatron will thus be able to improve the existing bounds on anomalous $Z\gamma V$ couplings mostly for $h_{2,4}^V$. If an integrated luminosity of

10 fb^{-1} can be achieved in Run II, the limits listed in Tables 9 and 10 would improve by approximately a factor 1.5.

A few additional comments are in order at this point:

4.5.1. $WW/WZ \rightarrow e\nu jj$

Note that the expected Run II anomalous coupling limit has nearly been ruled out by the Run I combined analysis measurement. Nevertheless, if the Run II combined measurement is to scale based on the increase in the luminosity, all of the analyses must be carried out again.

4.5.2. $Z\gamma \rightarrow ee\gamma$ and $\mu\mu\gamma$

Scaling the Run I yield, totalling 29 $ee\gamma + \mu\mu\gamma$ candidates at $D\bar{O}$, by the increase in luminosity, one expects about 600 $ee\gamma + \mu\mu\gamma$ events per experiment. The QCD background and final state radiation background will be reduced compared to Run I through the application of a di-lepton invariant mass criteria, reducing the samples to ~ 250 events. The Run II data will settle once and for all, whether there is a bump in the $Z\gamma$ invariant mass spectrum, as is not very strongly suggested by the Run I data. That is, unless a new one crops up.

4.5.3. $Z\gamma \rightarrow \nu\bar{\nu}\gamma$

This is a powerful tool for studying $Z\gamma\gamma$ and $ZZ\gamma$ couplings because of the large (20%) branching fraction for $Z \rightarrow \nu\bar{\nu}$. However, because the Z boson is undetectable, there aren't any other kinematic handles. There are common backgrounds which produce the same signature as the signal: a photon recoiling against missing transverse energy (neutrinos). In order to reduce the backgrounds, a higher E_T^γ cut is used than in the other $Z\gamma$ analyses (40 GeV instead of 7 – 10 GeV). Understanding the normalization of the background from cosmic ray muons that happened to deposit energy in the calorimeter in such a way as to

Table 10

95% confidence level $Z\gamma V$ anomalous coupling limits that might be achieved by DØ or CDF experiments in Run II.

Analysis	Lum. (pb ⁻¹)	Λ_{FF}	A.C. Limit (95% CL)
$Z\gamma \rightarrow ee\gamma$	1000	1.5 TeV	$-0.105 \leq h_{30}^V \leq 0.105$ $-0.0064 \leq h_{40}^V \leq 0.0064$
$Z\gamma \rightarrow \nu\nu\gamma$	1000	1.5 TeV	$-0.038 \leq h_{30}^V \leq 0.038$ $-0.0027 \leq h_{40}^V \leq 0.0027$

mimic a photon was the main difficulty in this analysis in Run I. This background should be more tractable in Run II using the new central and forward preshower detectors and a technique similar to that described in DØ’s Run Ia publications [139, 144].

4.6. New Directions in Di-boson Production for Run II

Besides improving limits from final states analyzed in Run I, a number of new channels will become accessible in Run II, either due to the increased data sample, or because of detector improvements. In addition, it will be possible to search for the so-called “radiation zero” in $W\gamma$ production. In this subsection, we first briefly describe the search for the radiation zero and the prospects for using di-boson final states involving b -quarks. This is followed by a somewhat more detailed analysis of ZZ production, the main new di-boson channel which will become accessible in Run II.

4.6.1. Radiation Zero in $W\gamma$ Production

$W\gamma$ production is of special interest because of the “radiation zero” in the helicity amplitudes [147]. The Tev.2000 Report describes the situation very eloquently and completely. The SM helicity amplitudes of the process $q_1\bar{q}_2 \rightarrow W^\pm\gamma$ vanish for

$$\cos\theta^* = \frac{Q_1 + Q_2}{Q_1 - Q_2} = \pm\frac{1}{3} \quad (24)$$

where θ^* is the scattering angle of the W boson with respect to the quark (q_1) direction in the $W\gamma$ rest frame and Q_1 and Q_2 are the quark and anti-quark electric charges normalized by the proton electric charge. Anomalous couplings destroy the radiation zero as do higher-order QCD corrections, backgrounds, finite W -width effects, and events where the photon is radiated from the charged lepton instead of the W .

The trick in reconstructing θ^* is in determining the parton center-of-mass frame because there are two solutions for the z -component of the neutrino momentum. CDF discussed [148] a possible solution in selecting the minimum of the $p_z(\nu)$ solutions for $W^-\gamma$ and the maximum of the $p_z(\nu)$ solutions for $W^+\gamma$. This is correct 73% of the time because of the high

W polarization at Tevatron production energies. CDF saw a hint [148] of the radiation zero in Run Ib but the signal was not definitive.

The twofold ambiguity in reconstructing $\cos\theta^*$ can be avoided by studying rapidity correlations such as $\Delta y(\gamma, \ell) = y(\gamma) - y(\ell)$, which manifests the radiation zero at $\Delta y(\gamma, \ell) \approx -0.3$ [149].

The Tevatron is operating at the ideal energy for observing the radiation zero because the zero is not smeared out by NLO processes expected from $W\gamma$ production at higher energy accelerators. Fig. 56 shows the $\Delta y(\gamma, \ell)$ distribution, together with the statistical errors for 1 fb⁻¹. The radiation zero will be observed in Run II if it is there.

4.6.2. $WZ \rightarrow \ell\nu b\bar{b}$

This channel has not been studied in Run I. It will be examined very closely in Run II because it is a background in the search for associated Higgs boson production ($W + H^0$ where $W \rightarrow \ell\nu$ and $H^0 \rightarrow b\bar{b}$). The SM cross section for WZ production, including NLO QCD corrections, is about 3.7 pb. The branching fraction for $Z \rightarrow b\bar{b}$ is $\sim 15\%$. This is 2.5 times as much as that of $Z \rightarrow \mu\bar{\mu}$ and $Z \rightarrow e\bar{e}$ combined. So we can expect about 250 $e\nu b\bar{b} + \mu\nu b\bar{b}$ events per experiment, not counting acceptance, lepton ID, and b -tagging efficiencies, which can be expected to amount to ~ 0.20 for such a final state. A cut on $b\bar{b}$ invariant mass will reduce the W +jets background.

This is ripe for an anomalous coupling analysis. To produce WWZ anomalous coupling limits, one can fit the E_T spectrum of the W boson and of the final-state lepton, such as was done in the Run I $WW/WZ \rightarrow \ell\nu$ +jets analyses.

4.6.3. $Z\gamma \rightarrow b\bar{b}\gamma$

Scaling the Run I yield, totalling 29 $ee\gamma + \mu\mu\gamma$ candidates at DØ, by the increase in luminosity and a factor for the larger branching ratio of $Z \rightarrow b\bar{b}$ to $Z \rightarrow ee(\mu\mu)$, one might expect about 1000 $Z\gamma \rightarrow b\bar{b}\gamma$ events. Background from γjj and three jet events where a jet mimics a photon are larger than the signal and may constrain this to a limit-setting analysis (see also Sec. 3.3.5).

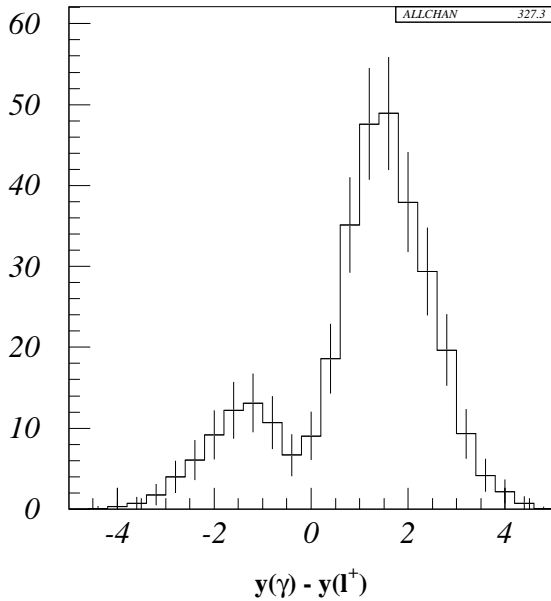


Figure 56. Simulation of the SM $\Delta y(\gamma, e)$ distribution in $p\bar{p} \rightarrow W^+\gamma \rightarrow e^+\not{p}_T\gamma$ in the DØ detector (from Ref. [77]). In addition to the standard \not{p}_T , electron and photon p_T and rapidity cuts, a $\Delta R(\gamma, \ell) > 0.7$ cut, and a cluster transverse mass cut of $m_T(\ell\gamma; \not{p}_T) > 90$ GeV are imposed (to reduce the $W \rightarrow e\nu\gamma$ background). The statistical error bars for an integrated luminosity of 1 fb^{-1} are also shown.

4.6.4. ZZ Production

For Run I, ZZ production has not been analyzed. The total cross section for $p\bar{p} \rightarrow ZZ$ at $\sqrt{s} = 2$ TeV, including NLO QCD corrections is approximately 1.5 pb. For an integrated luminosity of 2 fb^{-1} one thus expects a few $ZZ \rightarrow \ell_1^+\ell_1^-\ell_2^+\ell_2^-$ ($\ell_1, \ell_2 = e, \mu$) events, if realistic lepton p_T and pseudo-rapidity cuts are imposed. Larger event rates are expected for $ZZ \rightarrow \ell^+\ell^-\bar{\nu}\nu$, $ZZ \rightarrow \ell^+\ell^-\text{jj}$ and $ZZ \rightarrow \bar{\nu}\nu\text{jj}$. These channels, however, suffer from non-trivial background contributions. In this subsection we briefly discuss the signals of anomalous ZZV couplings in the four channels, and derive sensitivity bounds on f_4^V and f_5^V which one expects to achieve with 2 fb^{-1} (Run IIa) and 10 fb^{-1} (Run IIb). More details will be given elsewhere [116].

The results reported here are based on a tree level calculation of ZZ production in the double pole approximation. Timelike photon exchange and the decays of the Z bosons, including full decay correlations and finite Z width effects, are taken into account in the calculation. To simulate detector response, we impose the following transverse momentum, pseudo-rapidity

and separation cuts:

$$p_T(\ell) > 15 \text{ GeV}, \quad |\eta(\ell)| < 2.5, \quad (25)$$

$$p_T(j) > 20 \text{ GeV}, \quad |\eta(j)| < 2.5, \quad (26)$$

$$\Delta R(\ell j) > 0.6, \quad \Delta R(jj) > 0.6. \quad (27)$$

In the $ZZ \rightarrow \bar{\nu}\nu\text{jj}$ case, Eq. (25) is replaced by a charged lepton veto

$$p_T(\ell) < 10 \text{ GeV} \quad \text{for} \quad |\eta(\ell)| < 2.5. \quad (28)$$

In addition to the cuts imposed on the leptons and jets, we require

$$\not{p}_T > 20 \text{ GeV} \quad \text{for} \quad ZZ \rightarrow \ell^+\ell^-\not{p}_T, \quad (29)$$

$$\not{p}_T < 20 \text{ GeV} \quad \text{for} \quad ZZ \rightarrow \ell^+\ell^-\text{jj}, \quad (30)$$

$$\not{p}_T > 60 \text{ GeV} \quad \text{for} \quad ZZ \rightarrow \not{p}_T\text{jj} \quad (31)$$

and

$$76 \text{ GeV} < m(\ell\ell) < 106 \text{ GeV}, \quad (32)$$

$$76 \text{ GeV} < m(jj) < 106 \text{ GeV}. \quad (33)$$

Finally, in the $ZZ \rightarrow \ell^+\ell^-\bar{\nu}\nu$ case, we require that the angle in the transverse plane between a charged lepton and the missing transverse momentum is between 20° and 160° if the missing p_T is $\not{p}_T < 50$ GeV. This suppresses backgrounds from $b\bar{b}$ production and $Z \rightarrow \tau^+\tau^-$ decays to a negligible level.

Uncertainties in the energy measurements are taken into account in the numerical simulations by Gaussian smearing of the particle momenta according to the resolutions of the CDF II detector. For the form factor we use the form of Eq. (8) with $n = 3$ and $\Lambda_{FF} = 750$ GeV. We use the CTEQ4L parton distribution functions with $Q^2 = M_Z^2$. Unless stated otherwise, only one ZZV coupling at a time is chosen different from its zero SM value. For simplicity, we only consider real ZZV couplings.

$ZZ \rightarrow 4 \text{ leptons}$

Similar to the WWV and $Z\gamma V$ couplings, the effects of anomalous ZZV couplings are enhanced at large energies. A typical signal of nonstandard ZZZ and $ZZ\gamma$ couplings thus will be a broad increase in the ZZ invariant mass distribution, the Z transverse momentum distribution and the p_T distribution of the Z decay leptons. This is illustrated in Fig. 57 for the $p_T(Z)$ and the $p_T(\mu)$ distributions in $p\bar{p} \rightarrow ZZ \rightarrow e^+e^-\mu^+\mu^-$. Results are shown for the SM, $f_{40}^Z = 0.3$ and $f_{50}^Z = -0.3$. Terms proportional to f_4^V and f_5^V in the matrix elements have identical high energy behavior. Differences in the differential cross sections at high energies between ZZZ and $ZZ\gamma$ couplings are thus controlled by the $Zf\bar{f}$ and $\gamma f\bar{f}$ couplings, and

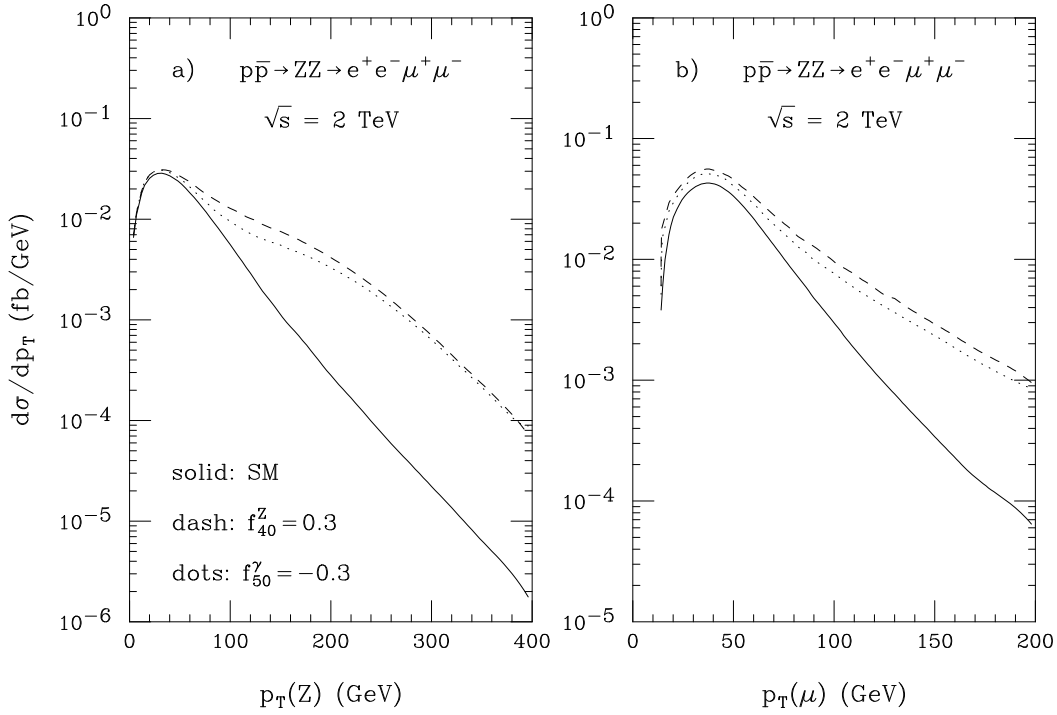


Figure 57. The $p_T(Z)$ and $p_T(\mu)$ distributions in $p\bar{p} \rightarrow ZZ \rightarrow e^+e^-\mu^+\mu^-$ in the SM and in the presence of non-standard ZZV couplings.

by the parton distribution functions. At the Tevatron these result in differential cross sections which differ by only a few percent for $\hat{s} \gg M_Z^2$ if $|f_i^Z| = |f_i^\gamma|$ ($i = 4, 5$). Slightly larger differences are observed at intermediate energies and transverse momenta. Since f_4^V violate CP conservation, terms in the helicity amplitudes proportional to those couplings do not interfere with the SM terms as long as f_4^V is real. Cross sections thus are independent of the sign of f_4^V .

To distinguish f_4^V and f_5^V , and to determine the sign of f_5^V , the $\Delta R(\ell_i^+\ell_i^-)$ and $\Delta\Phi(\ell_i^+\ell_i^-)$ ($i = 1, 2$) distributions may be helpful, if deviations from the SM predictions should be found in the p_T or the m_{ZZ} differential cross sections. Fig. 58 shows the $\Delta R(\mu^+\mu^-)$ and $\Delta\Phi(\mu^+\mu^-)$ distributions for $p\bar{p} \rightarrow ZZ \rightarrow e^+e^-\mu^+\mu^-$ in the SM and for non-standard ZZZ couplings. The shape of the distributions for non-zero f_4^V , $f_5^V > 0$ and $f_5^V < 0$ are quite different. Similar results are obtained for the corresponding distributions of the e^+e^- pair, and for the $ZZ\gamma$ couplings $f_{4,5}^\gamma$.

Anomalous couplings mostly affect the cross section at large Z -boson transverse momentum. Due to the Lorentz boost, the relative opening angle between the leptons originating from the Z decay decreases with increasing p_T . The deviations due to non-standard

ZZV couplings in the $\Delta R(\ell_i^+\ell_i^-)$ and $\Delta\Phi(\ell_i^+\ell_i^-)$ distributions thus are therefore concentrated at rather small values. The SM $\Delta R(\ell_i^+\ell_i^-)$ and $\Delta\Phi(\ell_i^+\ell_i^-)$ differential cross sections are dominated by the threshold region, $\sqrt{\hat{s}} \approx 2m_Z$, where the Z boson momenta are small and the decay leptons tend to be back-to-back, *i.e.* the distributions are strongly peaked at $\Delta R \approx 3$ and $\Delta\Phi = 180^\circ$.

Using the $\Delta R(\ell_i^+\ell_i^-)$ and $\Delta\Phi(\ell_i^+\ell_i^-)$ distributions, it may be possible to distinguish f_4^V and f_5^V and to determine the sign of f_5^V , provided a sufficient number of events are observed.

$$ZZ \rightarrow \ell^+\ell^-\bar{\nu}\nu$$

In contrast to the $ZZ \rightarrow 4$ leptons mode which is almost background free, there are several potentially important background processes if one of the two Z bosons decays into neutrinos. The advantage of the $ZZ \rightarrow \ell^+\ell^-\bar{\nu}\nu$ channel is its larger branching fraction. Summing over the three neutrino species, the number of $ZZ \rightarrow \ell^+\ell^-\bar{\nu}\nu$ signal events is about a factor 6 larger than the number of $ZZ \rightarrow 4$ leptons events.

The most important background processes contributing to the $ZZ \rightarrow \ell^+\ell^-\bar{\nu}\nu$ channel are $t\bar{t} \rightarrow$

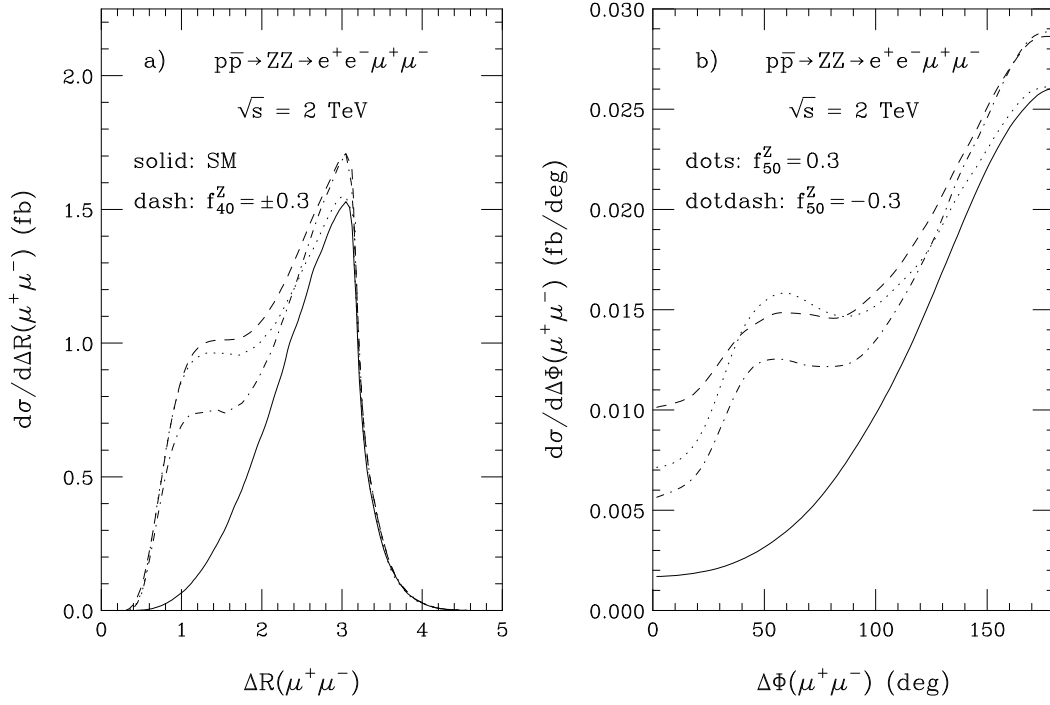


Figure 58. The $\Delta R(\mu^+\mu^-)$ and $\Delta\Phi(\mu^+\mu^-)$ distributions in $p\bar{p} \rightarrow ZZ \rightarrow e^+e^-\mu^+\mu^-$ in the SM and in the presence of non-standard ZZZ couplings.

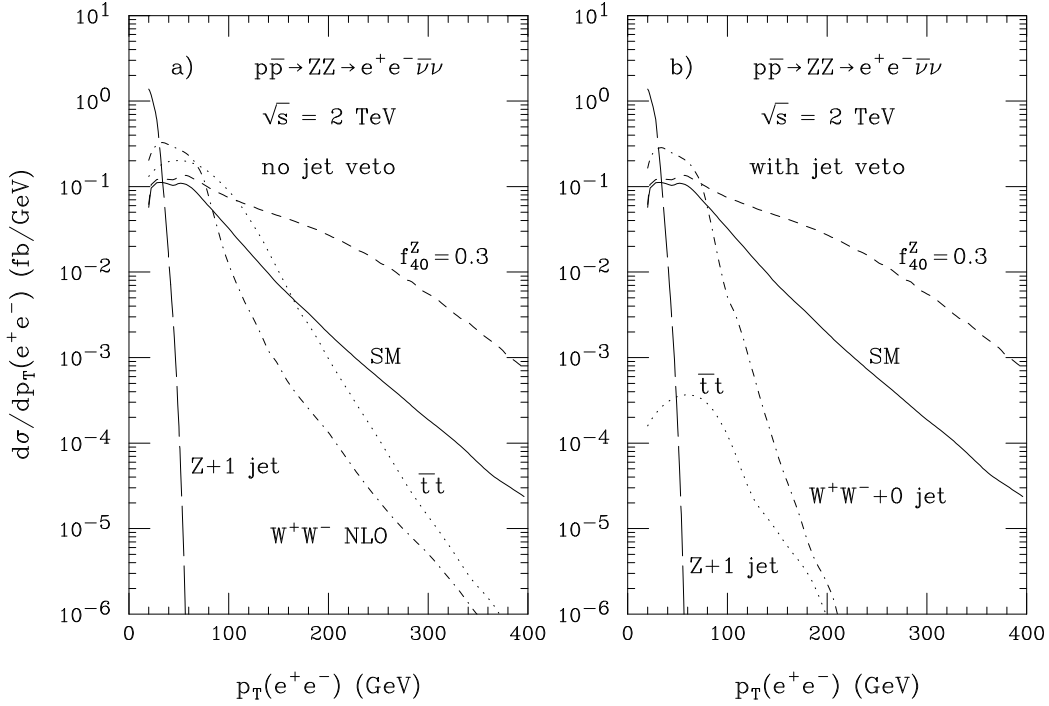


Figure 59. Transverse momentum distribution of the e^+e^- pair in $p\bar{p} \rightarrow ZZ \rightarrow e^+e^-\bar{\nu}\nu$ at the Tevatron, together with the differential cross sections from several background processes a) without and b) with a jet veto applied.

$W^+W^-b\bar{b}$, standard electroweak $W^+W^- + X$ production with $W^+W^- \rightarrow \ell^+\nu\ell^-\bar{\nu}$, and $Z(\rightarrow \ell^+\ell^-) + 1$ jet production with the jet rapidity outside the range covered by the detector and thus faking missing p_T . Our results for signal and backgrounds are summarized in Fig. 59 for the $ZZ \rightarrow e^+e^-\bar{\nu}\nu$ case.

The two most important backgrounds are $t\bar{t}$ and $W^+W^- + X$ production. If no additional cuts are imposed to suppress the $t\bar{t}$ background, its differential cross section is larger than the SM signal for e^+e^- transverse momenta as large as 200 GeV, and may thus reduce the sensitivity to anomalous ZZV couplings (see Fig. 59a). Requiring that no jets with $p_T(j) > 20$ GeV and $|\eta(j)| < 3.5$ are present almost completely eliminates the $t\bar{t}$ background. It also reduces the $W^+W^- + X$ background at large transverse momenta. As shown in Fig. 55, NLO QCD corrections strongly affect the $p_T(e^+e^-)$ distribution in $W^+W^- \rightarrow e^+\nu e^-\bar{\nu}$. The enhancement at large p_T is mostly due to real emission diagrams, leading to events which contain a hard jet.

To calculate the $Z + 1$ jet background, we have assumed that jets with a rapidity $|\eta(j)| > 3.5$ are misidentified as \cancel{p}_T . With this rather conservative assumption, the $Z + 1$ jet background is much larger than the ZZ signal at small transverse momenta. Due to kinematical constraints, however, it drops rapidly with p_T . Since non-standard ZZV couplings lead to large deviations from the SM only at high transverse momentum, essentially no sensitivity is lost by requiring $p_T(\ell^+\ell^-) > 40$ GeV when testing for ZZV couplings.

$ZZ \rightarrow \ell^+\ell^-jj$ and $ZZ \rightarrow \bar{\nu}\nu jj$

The $ZZ \rightarrow \ell^+\ell^-jj$ and $ZZ \rightarrow \bar{\nu}\nu jj$ channels have larger branching ratios than the $ZZ \rightarrow 4$ leptons and the $ZZ \rightarrow \ell^+\ell^-\bar{\nu}\nu$ channels, but also much higher backgrounds. The main background sources are QCD $Z + 2$ jet production and $W^\pm Z$ production with the W decaying into two jets. The $p_T(\ell^+\ell^-)$ distribution for $ZZ \rightarrow \ell^+\ell^-jj$ is shown in Fig. 60a. Fig. 60b shows the $p_T(jj)$ distribution for $ZZ \rightarrow \bar{\nu}\nu jj$. In each case we display the SM cross section together with the two main backgrounds, Zjj and $W^\pm Z$ production. We also show the ZZ cross section for $f_{40}^Z = 0.3$.

The $\cancel{p}_T > 60$ GeV cut imposed in the $ZZ \rightarrow \cancel{p}_Tjj$ case helps to suppress the $b\bar{b}$ and $Z \rightarrow \tau^+\tau^-$ backgrounds. The ‘‘kink’’ in the WZ and ZZ differential cross sections at $p_T \approx 250$ GeV is due to the $\Delta R(jj) > 0.6$ cut which becomes effective only at sufficiently high transverse momenta. The $W^\pm Z$ differential cross section is very similar to that of the SM signal over most of the p_T range considered. The $\cancel{p}_T < 20$ GeV cut imposed in the $ZZ \rightarrow \ell^+\ell^-jj$ channel

effectively eliminates the $t\bar{t} \rightarrow \ell^+\nu\ell^-\bar{\nu}jj$ background. The charged lepton veto (see Eq. (28)) required in the $ZZ \rightarrow \cancel{p}_Tjj$ case rejects backgrounds from $t\bar{t}$ production, $W \rightarrow \ell\nu$, and $Z \rightarrow \ell^+\ell^-$ decays. The Zjj background is uniformly about a factor 10 larger than the SM ZZ signal. It will therefore be very difficult to observe ZZ production in the semi-hadronic channels, if the SM prediction is correct. However, for sufficiently large anomalous ZZV couplings, the ZZ cross section exceeds the background at large transverse momenta. $ZZ \rightarrow \ell^+\ell^-jj$ and $ZZ \rightarrow \bar{\nu}\nu jj$ therefore may still be useful in obtaining limits on the ZZV couplings, similar to the semi-hadronic WW and WZ channels used by CDF and DØ in Run I to extract limits on the WWV couplings.

Sensitivity Bounds

In order to derive sensitivity limits for anomalous ZZV couplings which one can hope to achieve in Run II, we use the $p_T(\ell^+\ell^-)$ distribution for $ZZ \rightarrow 4$ leptons, $ZZ \rightarrow \ell^+\ell^-\bar{\nu}\nu$ and $ZZ \rightarrow \ell^+\ell^-jj$. For the $ZZ \rightarrow \bar{\nu}\nu jj$ channel we use the $p_T(jj)$ distribution. Other distributions, such as the ZZ invariant mass distribution (useful only for $ZZ \rightarrow 4$ leptons), or the maximum or minimum transverse momenta of the charged leptons or jets, yield similar results. In deriving our sensitivity limits, we combine channels with electrons and muons in the final state.

We calculate 95% confidence level (CL) limits performing a χ^2 test. The statistical significance is calculated by splitting the p_T distribution into a number of bins, each with more than five events typically. In each bin the Poisson statistics is approximated by a Gaussian distribution. In order to derive realistic limits, we allow for a normalization uncertainty of 30% of the SM cross section. Backgrounds in the $ZZ \rightarrow \ell^+\ell^-\bar{\nu}\nu$, $ZZ \rightarrow \ell^+\ell^-jj$ and $ZZ \rightarrow \bar{\nu}\nu jj$ channels are included in our calculation. In the $ZZ \rightarrow \ell^+\ell^-\bar{\nu}\nu$ case we assume that a jet veto has been imposed to reduce the $t\bar{t}$ background and require $p_T(\ell^+\ell^-) > 40$ GeV to eliminate the $Z + 1$ jet background. As before, we use a form factor of the form of Eq. (8) with $n = 3$ and $\Lambda_{FF} = 750$ GeV. Non-negligible interference effects are found between f_4^Z and f_4^γ , and between f_5^Z and f_5^γ . As a result, different anomalous contributions to the helicity amplitudes may cancel partially, resulting in weaker bounds than if only one coupling at a time is allowed to deviate from its SM value.

In Table 11 we display sensitivity limits for the Tevatron and integrated luminosities of 2 fb^{-1} and 10 fb^{-1} , taking into account the correlations between f_4^Z and f_4^γ , and between f_5^Z and f_5^γ . No limits for the $ZZ \rightarrow 4$ leptons case with 2 fb^{-1} are given. The lim-

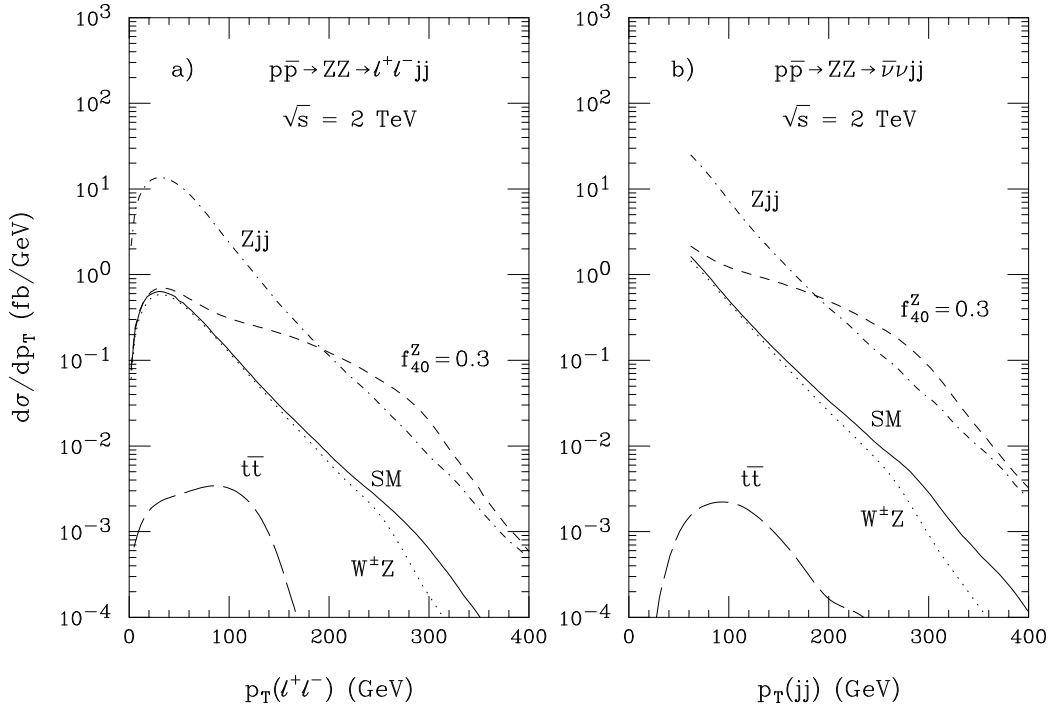


Figure 60. Transverse momentum distribution of a) the $\ell^+\ell^-$ pair in $p\bar{p} \rightarrow ZZ \rightarrow \ell^+\ell^-jj$, and b) of the jet pair in $ZZ \rightarrow \bar{\nu}\nu jj$ at the Tevatron, together with the differential cross sections from $t\bar{t}$, $W^\pm Z$ and $Z + 2$ jet production.

ited number of events in this case does not allow for an analysis of the $p_T(\ell^+\ell^-)$ distribution using the method chosen here. The bounds obtained from $ZZ \rightarrow \ell^+\ell^- \bar{\nu}\nu$ and $ZZ \rightarrow \bar{\nu}\nu jj$ are quite similar. The cross section for $ZZ \rightarrow \bar{\nu}\nu jj$ is about a factor 10 larger than that for $ZZ \rightarrow \ell^+\ell^- \bar{\nu}\nu$, however, the large background from Zjj production considerably limits the sensitivity to ZZV couplings for $ZZ \rightarrow \bar{\nu}\nu jj$. The limits from the $ZZ \rightarrow \ell^+\ell^- jj$ and $ZZ \rightarrow 4$ leptons channels are about a factor 1.5 and 2 weaker than those from $ZZ \rightarrow \ell^+\ell^- \bar{\nu}\nu$ and $ZZ \rightarrow \bar{\nu}\nu jj$.

We have not made any attempt to combine the limits from different channels. From Table 11 it is clear that this would result in a significant improvement of the bounds.

The sensitivity limits which can be achieved at the Tevatron in Run II should be compared with the bounds from recent measurements at LEP2 [146]:

$$|f_4^Z| < 0.49 \quad |f_4^\gamma| < 0.82 \quad (34)$$

$$|f_5^Z| < 1.1 \quad |f_5^\gamma| < 1.1 \quad (35)$$

Only one coupling at a time is varied here. (The LEP2 limits do not contain any form factor effects. For the form and scale chosen here, form factor effects weaken the limits by about 20%.) In Run II, CDF and DØ will be able to improve these bounds by at least a factor 4

to 8.

4.6.5. Measuring Form Factors

The limits on anomalous WWV , $Z\gamma V$ and ZZV couplings all depend on the power, n , and the scale, Λ_{FF} , of the form factor. These parameters are *a priori* unknown. In Ref. [117] it was pointed out that in final states without missing transverse momentum one can in principle determine the form factor by measuring the $\sqrt{\hat{s}}$ distribution. For $W\gamma$ production, the longitudinal momentum of the neutrino can only be reconstructed with a twofold ambiguity. Selecting the minimum of the two reconstructed values of \hat{s} , a similar measurement can be performed in the $W\gamma$ case [125]. Alternatively, the photon p_T distribution can be used.

In Ref. [127] a detailed study of the method was performed for $W(\rightarrow e\nu, \mu\nu)\gamma$ production at the LHC. Assuming $\lambda_0^\gamma = 0.025$, $n = 2$, $\Lambda_{FF} = 2$ TeV and an integrated luminosity of 300 fb^{-1} , λ_0^γ and Λ_{FF} were reconstructed using a binned maximum likelihood fit to the $p_T(\gamma)$ distribution. The power of the form factor, $n = 2$, was not varied and no detector simulation was included in the study. The reconstructed coupling and form factor scale were determined to $\lambda_0^\gamma = 0.0295 \pm 0.0022$ and $\Lambda_{FF} = 1.67 \pm 0.22$ TeV, *ie.* they can be measured with a relative precision

Table 11

Sensitivities achievable at 95% CL for the anomalous ZZV couplings in $p\bar{p} \rightarrow ZZ \rightarrow 4$ leptons, $p\bar{p} \rightarrow ZZ \rightarrow \ell^+\ell^-\bar{\nu}\nu$, $p\bar{p} \rightarrow ZZ \rightarrow \ell^+\ell^-\text{jj}$, and $p\bar{p} \rightarrow ZZ \rightarrow \bar{\nu}\nu\text{jj}$ at the Tevatron a) for an integrated luminosity of 2 fb^{-1} , and b) for an integrated luminosity of 10 fb^{-1} .

a) $\int \mathcal{L} dt = 2 \text{ fb}^{-1}$				
coupling	$ZZ \rightarrow 4$ leptons	$ZZ \rightarrow \ell^+\ell^-\bar{\nu}\nu$	$ZZ \rightarrow \ell^+\ell^-\text{jj}$	$ZZ \rightarrow \bar{\nu}\nu\text{jj}$
f_{40}^Z	–	+0.169 –0.169	+0.219 –0.218	+0.156 –0.155
f_{40}^γ	–	+0.175 –0.174	+0.222 –0.221	+0.157 –0.157
f_{50}^Z	–	+0.171 –0.204	+0.220 –0.244	+0.157 –0.179
f_{50}^γ	–	+0.184 –0.202	+0.229 –0.241	+0.166 –0.174
b) $\int \mathcal{L} dt = 10 \text{ fb}^{-1}$				
coupling	$ZZ \rightarrow 4$ leptons	$ZZ \rightarrow \ell^+\ell^-\bar{\nu}\nu$	$ZZ \rightarrow \ell^+\ell^-\text{jj}$	$ZZ \rightarrow \bar{\nu}\nu\text{jj}$
f_{40}^Z	+0.180 –0.179	+0.097 –0.097	+0.146 –0.145	+0.104 –0.103
f_{40}^γ	+0.185 –0.185	+0.100 –0.099	+0.148 –0.147	+0.104 –0.104
f_{50}^Z	+0.178 –0.216	+0.092 –0.120	+0.144 –0.167	+0.102 –0.124
f_{50}^γ	+0.192 –0.213	+0.103 –0.115	+0.151 –0.163	+0.109 –0.118

of about 10 – 15%. The central values of the reconstructed parameters differ by about 20% from the input parameters. Including detector response, and treating the form factor power n as an additional free parameter is expected to increase the relative error.

The study demonstrates that, due to the restricted number of events in each bin, the method will not produce competitive limits. However, if non-zero anomalous couplings are observed, the method may be useful in determining the shape of the form factor which provides indirect information on the dynamics of the underlying new physics.

At the Tevatron, the limits on the WWV couplings exhibit only a modest dependence on n and Λ_{FF} . Direct measurement of the form factor will thus be very difficult for these couplings. The situation is more promising for $Z\gamma V$ and ZZV couplings, where the sensitivity bounds depend more strongly on the form factor parameters.

Acknowledgements

We acknowledge contributions from the other members of the working group including P. Aurenche,

C. Balázs, L. Dixon, S. Eno, G. Gomez, N. Kidonakis, P. Nason, J. Qiu, and G. Sterman. We also thank T. Ferbel, M. Fontannaz, G. Ginther, B. Kniehl, A. D. Martin, R. Roberts, P. Slattery, J. Stirling, R. Thorne and W.K. Tung. We also wish to thank A. Beretvas, C. Bigongiari, J. Campbell, O. Lobban, and W. Wester for their help. Special thanks go to M. Mangano for some enlightening discussions.

REFERENCES

1. R. Brock *et al.*, Report of the *Precision Measurement* Working Group.
2. L. deBarbaro *et al.*, Report of the Working Group on *Parton Distribution Functions*.
3. F. Abe *et al.* (CDF Collaboration), Phys. Rev. **D60**, 092003 (1999).
4. B. Bailey, E. L. Berger, and L. E. Gordon, Phys.Rev. **D54**, 1896 (1996).
5. P. Aurenche *et al.*, Phys. Lett. **B140**, 87 (1984).
6. E.L. Berger, E. Braaten, and R.D. Field, Nucl. Phys. **B239**, 52 (1984).
7. E.L. Berger and J.W. Qiu, Phys. Rev. **D44**,2002 (1991).

8. B. Bailey, J. F. Owens, and J. Ohnemus, Phys. Rev. **D46**, 2018 (1992).
9. T. Binoth *et al.*, Eur. Phys. J. **C16**, 311 (2000).
10. C. Balázs, E.L. Berger, S. Mrenna, and C.-P. Yuan, Phys. Rev. **D57**, 6934 (1998).
11. P. Chiappetta, R. Fergani, and J. Guillet, Phys. Lett. **B348**, 646 (1995).
12. S. Catani *et al.*, JHEP **9903**, 025 (1999).
13. N. Kidonakis and J. F. Owens, Phys. Rev. **D61**, 094004 (2000).
14. E. Laenen, G. Oderda, and G. Sterman, Phys. Lett. **B438**, 173 (1998).
15. H.-L. Lai and H. nan Li, Phys. Rev. **D58**, 114020 (1998).
16. H. nan Li, Phys. Lett. **B454**, 328 (1999).
17. E. Laenen, G. Sterman, and W. Vogelsang, Phys. Rev. Lett. **84**, 4296 (2000).
18. J. Huston *et al.* (CTEQ Collaboration), Phys. Rev. **D58**, 114034 (1998).
19. H. L. Lai *et al.* (CTEQ Collaboration), Phys. Rev. **D55**, 1280 (1997).
20. M. Glück, E. Reya, and A. Vogt, Z. Phys. **C53**, 127 (1992).
21. A. D. Martin *et al.*, Eur. Phys. J. **C4**, 463 (1998).
22. H. Baer and M. Reno, Phys. Rev. **D54**, 2017 (1996).
23. J. Huston *et al.* (CTEQ Collaboration), Phys. Rev. **D51**, 6139 (1995).
24. L. Apanasevich *et al.*, Phys. Rev. **D59**, 074007 (1999).
25. P. Aurenche *et al.*, Eur. Phys. J. **C9**, 107 (1999).
26. P. Aurenche *et al.*, Eur. Phys. J. **C13**, 347 (2000).
27. M.A. Kimber, A.D. Martin, and M.G. Ryskin, Eur. Phys. J. **C12**, 655 (2000).
28. C. Balázs, J. Huston, and I. Puljak, hep-ph/0002032 (February 2000), submitted to Phys. Rev. **D**.
29. C. Balázs, Ph.D. thesis, Michigan State University, 1999.
30. S. Catani *et al.*, hep-ph/0005114 (May 2000), to appear in the Proceedings of the *Workshop on Physics at TeV Colliders* (Les Houches, 1999).
31. M. Begel, Nucl. Phys. B (Proc. Supp.) **79**, 244 (1999); Ph.D. thesis, University of Rochester, 1999.
32. E. Bonvin *et al.* (WA70 Collaboration), Phys. Lett. **B236**, 523 (1990).
33. F. Abe *et al.* (CDF Collaboration), Phys. Rev. Lett. **70**, 2232 (1993).
34. R. Barate *et al.* (WA11 Collaboration), Phys. Rev. Lett. **21**, 1541 (1979); M. J. Corden *et al.* (WA12 Collaboration), Phys. Lett. **B76**, 226 (1978); A. L. S. Angelis *et al.* (R108 Collaboration), Phys. Lett. **B97**, 163 (1980); D. Antreasyan *et al.* (R209 Collaboration), Phys. Rev. Lett. **47**, 12 (1981); J. Badier *et al.* (NA3 Collaboration), Phys. Lett. **B117**, 372 (1982); A. S. Ito *et al.* (E288 Collaboration), Phys. Rev. **D23**, 604 (1981); D. Antreasyan *et al.* (E300 Collaboration), Phys. Rev. Lett. **39**, 906 (1977); M. D. Corcoran *et al.* (E395 Collaboration), Phys. Rev. **D21**, 641 (1980); K. J. Anderson *et al.* (E444 Collaboration), Phys. Rev. Lett. **42**, 944 (1979); E. Anassontzis *et al.* (E537 Collaboration), Phys. Rev. **D38**, 1377 (1988); G. Moreno *et al.* (E605 Collaboration), Phys. Rev. **D43**, 2815 (1991); S. Palestini *et al.* (E615 Collaboration), Phys. Rev. Lett. **55**, 2649 (1985); J. S. Conway *et al.*, Phys. Rev. **D39**, 92 (1989); J. Alsjpector *et al.* (E687 Collaboration), Phys. Lett. **B81**, 397 (1979).
35. A. L. S. Angelis *et al.* (R108 Collaboration), Phys. Lett. **B97**, 163 (1980); A. G. Clark *et al.* (R702 Collaboration), Nucl. Phys. **B160**, 397 (1979).
36. W. Chen, Ph.D. thesis, State University of New York at Stony Brook, 1997.
37. H.-U. Bengtsson and T. Sjostrand, Comput. Phys. Commun. **46**, 43 (1987), [Pythia v5.7].
38. J. F. Owens, Rev. Mod. Phys. **59**, 465 (1987).
39. A. P. Contogouris, S. Papadopoulos, and C. Papavassiliou, Nucl. Phys. **B179**, 461 (1981).
40. A. P. Contogouris *et al.*, Phys. Rev. **D32**, 1134 (1985).
41. M. Fontannaz and D. Schiff, Nucl. Phys. **B132**, 457 (1978).
42. R. P. Feynman, R. D. Field, and G. C. Fox, Phys. Rev. **D18**, 3320 (1978).
43. J. Collins and D. Soper, Nucl. Phys. **B193**, 381 (1981); **B213**, 545(E) (1983); **B197**, 446 (1982); J. Collins, D. Soper, G. Sterman, Phys. Lett. **B109**, 388 (1982).
44. J.C. Collins, D.E. Soper, and G. Sterman, Nucl. Phys. **B250**, 199 (1985).
45. L. Apanasevich *et al.* (E706 Collaboration), Phys. Rev. Lett. **81**, 2642 (1998).
46. M. Bonesini *et al.* (WA70 Collaboration), Z. Phys. **C37**, 535 (1988).
47. M. Bonesini *et al.* (WA70 Collaboration), Z. Phys. **C38**, 371 (1988).
48. G. Ballocci *et al.* (UA6 Collaboration), Phys. Lett. **B436**, 222 (1998).
49. E. Bonvin *et al.* (WA70 Collaboration), Z. Phys. **C41**, 591 (1989).
50. L. Apanasevich, Ph.D. thesis, Michigan State University, 2000.
51. M. Bonesini *et al.* (WA70 Collaboration), Z. Phys. **C37**, 39 (1987).
52. J. Antille *et al.* (UA6 Collaboration), Phys. Lett. **B194**, 568 (1987).

53. E. Anassontzis *et al.* (R806 Collaboration), *Z. Phys.* **C13**, 277 (1982).
54. C. Kourkoumelis *et al.* (R806 Collaboration), *Z. Phys.* **C5**, 95 (1980).
55. M. Diakonou *et al.* (R806 Collaboration), *Phys. Lett.* **B91**, 296 (1980).
56. S. Kuhlmann, *Nucl. Phys. B (Proc. Suppl.)* **79**, 241 (1999).
57. B. Abbott *et al.* (DØ Collaboration), *Phys. Rev. Lett.* **84**, 2786 (2000).
58. R. Ansari *et al.* (UA2 Collaboration), *Z. Phys.* **C41**, 395 (1988).
59. J. Alitti *et al.* (UA2 Collaboration), *Phys. Lett.* **B288**, 386 (1992).
60. S. Abachi *et al.* (DØ Collaboration), FERMILAB-PUB-96-357-E.
61. V. Zutshi, DØ note in preparation.
62. Y. Gershtein, DØ note in preparation.
63. H. L. Lai *et al.* (CTEQ Collaboration), *Phys. Rev.* **D51**, 4763 (1995).
64. H. L. Lai *et al.* (CTEQ Collaboration), *Eur. Phys. J.* **C12**, 375 (2000).
65. G. Sterman and W. Vogelsang, hep-ph/0002132 (February 2000).
66. S. Catani, M.L. Mangano, and P. Nason, hep-ph/9806484, *JHEP* **9807**, 024 (1998).
67. Yu.L. Dokshitzer, D.I. Dyakanov, and S.I. Troyan, *Phys. Rep.* **58**, 269 (1980).
68. R.K. Ellis and S. Veseli, hep-ph/9706526, *Nucl. Phys.* **B511**, 649 (1998).
69. W. Vogelsang and A. Vogt, hep-ph/9505404, *Nucl. Phys.* **B453**, 334 (1995).
70. H. Baer, J. Ohnemus, and J.F. Owens, *Phys. Rev.* **D42**, 61 (1990).
71. F. Abe *et al.* (CDF Collaboration), *Phys. Rev. Lett.* **77**, 439 (1996); a paper on the Run Ib analysis is in preparation.
72. B. Abbott *et al.* (DØ Collaboration), *Phys. Rev. Lett.* **82**, 2451 (1999).
73. F. Abe *et al.* (CDF Collaboration), *Phys. Rev.* **D57**, 1359 (1998).
74. E. L. Berger, Xiao-feng Guo, and Jian-wei Qiu, hep-ph/9512281, *Phys.Rev.Lett.* **76**, 2234 (1996); hep-ph/9605324, *Phys. Rev.* **D54**, 5470 (1996).
75. P. Aurenche *et al.*, hep-ph/9606287, *Phys. Rev.* **D55** 1124 (1997).
76. S. Frixione, hep-ph/9801442, *Phys. Lett.* **B429**, 369 (1998).
77. D. Amidei *et al.*, *Future Electro-Weak Physics at the Fermilab Tevatron*, edited by D. Amidei and R. Brock, FERMILAB-Pub-96/082 (1996).
78. B. Abbott *et al.* (DØ Collaboration), *Phys. Rev.* **D61**, 072001 (2000).
79. D. Cronin-Hennessy, A. Beretvas, P.F. Derwent, *Nucl. Instrum. Meth.* **A443**, 37 (2000).
80. F. Abe *et al.* (CDF Collaboration), *Phys. Rev.* **D50**, 5550 (1994).
81. C. Avila *et al.* (E811 Collaboration), *Phys. Lett.* **B445**, 419 (1999).
82. N. Amos *et al.* (E710 Collaboration), *Phys. Rev. Lett.* **68**, 2433 (1992).
83. M. Albrow, A. Beretvas, L. Nodulman, and P. Giromini, CDF-PUB-4844 (1999).
84. J. Bantly, J. Krane, D. Owen, R. Partridge, and L. Paterno, Fermilab-TM-1995 (1997).
85. R. Hamberg, W.L. van Neerven, and T. Matsuura, *Nucl. Phys.* **B359**, 343 (1991); W.L. van Neerven and E.B. Zijlstra, *Nucl. Phys.* **B382**, 11 (1992).
86. For a review of resummation in transverse momentum space, see R.K. Ellis and S. Veseli, *Nucl. Phys.* **B511**, 649 (1998).
87. For a review of resummation in the Fourier conjugate impact parameter space, see C. Balázs and C.-P. Yuan, *Phys. Rev.* **D56**, 5558 (1997).
88. B. Abbott *et al.* (DØ Collaboration), *Phys. Rev.* **D58**, 092003 (1998).
89. F. Abe *et al.* (CDF Collaboration), *Phys. Rev.* **D52**, 4784 (1995).
90. C. Balázs and C.-P. Yuan, *Phys. Rev.* **D59**, 114007 (1999).
91. Q. Fan and A. Bodek, Proceedings, 6th *International Conference on Calorimetry in High Energy Physics* (ICCHEP 96), Rome, Italy, 8 – 14 June 1996, pp. 553 – 560.
92. T. Sjöstrand, *Comput. Phys. Commun.* **82**, 74 (1994).
93. E. Barberio and Z. Was, *Comput. Phys. Commun.* **79**, 291 (1994); E. Barberio, B. van Eijk, and Z. Was, *ibid.* **66**, 115 (1991).
94. T. Affolder *et al.* (CDF Collaboration), *Phys. Rev. Lett.* **84**, 845 (2000).
95. G.A. Ladinsky and C.-P. Yuan, *Phys. Rev.* **D50**, 4239 (1994).
96. B. Abbott *et al.* (DØ Collaboration), *Phys. Rev.* **D61**, 032004 (2000).
97. U. Baur, S. Keller, and W. K. Sakumoto, *Phys. Rev.* **D57**, 199 (1998).
98. F. Abe *et al.* (CDF Collaboration), *Phys. Rev.* **D59**, 052002 (1999).
99. A. Bodek *et al.* for the CDF Collaboration, *Constraints on PDF's from W and Z Rapidity Distributions at CDF*, Fermilab-Conf-99/160-E, to be published in Proceedings, 7th *International Conference on Deep Inelastic Scattering and QCD* (DIS 99), DESY, Zeuthen, Germany, 19 – 24 April 1999.
100. G. Arnison *et al.* (UA1 Collaboration), *Phys. Lett.* **B122**, 103 (1983).

101. G. Arnison *et al.* (UA1 Collaboration), Phys. Lett. **B126**, 398 (1983).
102. G. Banner *et al.* (UA1 Collaboration), Phys. Lett. **B122**, 476 (1983).
103. P. Bagnaia *et al.* (UA1 Collaboration), Phys. Lett. **B129**, 130 (1983).
104. J. Alitti *et al.* (UA2 Collaboration), Phys. Lett. **B186**, 452 (1987).
105. J. Alitti *et al.* (UA2 Collaboration), Z. Phys. **C49**, 17 (1991).
106. M. Carena *et al.*, *Report of the Higgs Working Group*, Fermilab Supersymmetry/Higgs Run II Workshop (1998).
107. U. Baur and E.L. Berger, Phys. Rev. **D47**, 4889 (1993).
108. E. Mirkes, Nucl. Phys. **B387**, 3 (1992).
109. J.C. Collins and D.E. Soper, Phys. Rev. **D16**, 2219 (1977).
110. M.I. Martin, *Measurement of the Angular Distribution of the Electron from $W \rightarrow e\nu$ decay in $p\bar{p}$ at $\sqrt{s}=1.8$ TeV as Function of p_T^W* , PhD thesis, Universidad de Zaragoza, Spain, 1994 (unpublished).
111. G. Steinbrück, *Measurement of the Angular Distribution of Electrons from W Boson Decays at $D\bar{O}$* , PhD thesis, University of Oklahoma, Norman, Oklahoma, 1999 (unpublished).
112. K. Hagiwara, R. D. Peccei, D. Zeppenfeld and K. Hikasa, Nucl. Phys. **B282**, 253 (1987).
113. U. Baur and D. Zeppenfeld, Nucl. Phys. **B308**, 127 (1988).
114. G. Gounaris *et al.*, in *Physics at LEP2*, edited by G. Altarelli, T. Sjöstrand and F. Zwirner, CERN 96-01, 525 (1996).
115. K. Hagiwara, S. Ishihara, R. Szalapski and D. Zeppenfeld, Phys. Rev. **D48**, 2182 (1993).
116. U. Baur and D. Rainwater, FERMILAB-Pub-00/153-T, to appear in Phys. Rev. D.
117. G.J. Gounaris, J.Layssac and F.M. Renard, Phys. Rev. **D61**, 073013 (2000).
118. B. Mele, P. Nason and G. Ridolfi, Nucl. Phys. **B357**, 409 (1991); S. Frixione, P. Nason and G. Ridolfi, Nucl. Phys. **B383**, 3 (1992); S. Frixione, Nucl. Phys. **B410**, 280 (1993).
119. U. Baur, T. Han, and J. Ohnemus, Phys. Rev. **D48**, 5140 (1993).
120. U. Baur, T. Han, and J. Ohnemus, Phys. Rev. **D57**, 2823 (1998).
121. U. Baur, T. Han, and J. Ohnemus, Phys. Rev. **D53**, 1098 (1996).
122. U. Baur, T. Han, and J. Ohnemus, Phys. Rev. **D51**, 3381 (1995).
123. J.M. Campbell and R.K. Ellis, Phys. Rev. **D60**, 113006 (1999).
124. L. Dixon, Z. Kunszt and A. Signer, Phys. Rev. **D60**, 114037 (1999).
125. D. DeFlorian and A. Signer, Eur. Phys. J. **C16**, 105 (2000).
126. H.L. Lai *et al.* (CTEQ Collaboration), Phys. Rev. **D55**, 1280 (1997).
127. S. Haywood *et al.*, Report of the Electroweak Physics Working Group, hep-ph/0003275 (March 2000), to appear in the CERN Yellow-Report of the 1999 CERN Workshop on Standard Model Physics (and more) at the LHC.
128. M. Dobbs, private communication.
129. F. Abe *et al.* (CDF Collaboration), Phys. Rev. Lett. **74**, 1936 (1995).
130. S. Abachi *et al.* ($D\bar{O}$ Collaboration), Phys. Rev. Lett. **75**, 1034 (1995).
131. S. Abachi *et al.* ($D\bar{O}$ Collaboration), Phys. Rev. Lett. **78**, 3634 (1997).
132. S. Abachi *et al.* ($D\bar{O}$ Collaboration), Phys. Rev. Lett. **75**, 1023 (1995).
133. F. Abe *et al.* (CDF Collaboration), Phys. Rev. Lett. **78**, 4537 (1997).
134. B. Abbott *et al.* ($D\bar{O}$ Collaboration), Phys. Rev. **D58**, 051101 (1998).
135. F. Abe *et al.* (CDF Collaboration), Phys. Rev. Lett. **75**, 1017 (1995).
136. S. Abachi *et al.* ($D\bar{O}$ Collaboration), Phys. Rev. Lett. **77**, 3303 (1996).
137. B. Abbott *et al.* ($D\bar{O}$ Collaboration), Phys. Rev. Lett. **79**, 1441 (1997).
138. B. Abbott *et al.* ($D\bar{O}$ Collaboration), Phys. Rev. **D60**, 072002 (1999).
139. S. Abachi *et al.* ($D\bar{O}$ Collaboration), Phys. Rev. **D56**, 6742 (1997).
140. B. Abbott *et al.* ($D\bar{O}$ Collaboration), Phys. Rev. **D58**, 031102 (1998).
141. F. Abe *et al.* (CDF Collaboration), Phys. Rev. Lett. **74**, 1941 (1995).
142. S. Abachi *et al.* ($D\bar{O}$ Collaboration), Phys. Rev. Lett. **75**, 1028 (1995).
143. B. Abbott *et al.* ($D\bar{O}$ Collaboration), Phys. Rev. **D57**, 3817 (1998).
144. S. Abachi *et al.* ($D\bar{O}$ Collaboration), Phys. Rev. Lett. **78**, 3640 (1997).
145. J. Papavassiliou and K. Philippides, Phys. Rev. **D60**, 113007 (1999).
146. G. Bella *et al.* (The LEP TGC Working Group), LEPEWWG/TGC/2000-01 (March 2000).
147. R.W. Brown and K.O. Mikaelian, Phys. Rev. **D19**, 922 (1979).
148. D. Benjamin, Proceedings of the 10th Topical Workshop on Proton-Antiproton Collider Physics, Batavia, IL, May 1995, edited by R. Raja and J. Yoh, AIP Press (1996), p. 370.
149. U. Baur, S. Errede and G. Landsberg, Phys. Rev.

D50, 1917 (1994).